The University of Manchester

Imaging of hidden objects by planar capacitive and magnetic sensor arrays for security applications

A thesis submitted to the University of Manchester
for the degree of Doctor of Philosophy
in the Faculty of Engineering and Physical Science

2009

Xiaohui Hu

School of Electrical and Electronic Engineering

Table of Contents

List of figures

List of tables

Abstract

For the convenience of passengers, a shoe scanner is needed in public transportation portals as a supplementary tool for human screening. In addition, security scanners are needed in post-offices for scanning envelopes or small parcels. Imaging with electromagnetic sensors operating in the low frequency range has the advantages of low-cost, fast response and no radiation, and is of interest to be further exploited. This thesis investigates the detection of hidden threat objects by imaging with planar capacitive and coil sensor arrays.

Planar sensors can provide one-sided access to an MUT, but have complex response features and design issues. To explore imaging with planar sensors, different single-modality sensor arrays have been designed, including a concentric-ring-shaped array, a square-electrode-based adaptive array, a square-electrode-based single-electrode array for permittivity imaging, and a PCB-coil array for conductivity/permeability imaging. A dual-modality sensor array is assembled based on the ring array and the coil array for permittivity/conductivity/permeability imaging. The sensing depth of the sensor arrays have been evaluated experimentally, with results in agreement with simulations.

To interface to the single-modality and dual-modality sensor arrays, a novel multi-channel multi-modality imaging system has been developed based on an impedance analyser, HP4192A. Flexibility in sensor connection is achieved by using a specifically designed MUX box while implementation of different measurement protocols, image construction algorithms and post-analysis is supported by a layer-structured software design. For image reconstruction, the sensitivity coefficients based interpolation method is used with the ring array, the single-electrode array, the coil array and the dual-modality array. Tomographic imaging using LBP and Landweber iteration is used with the adaptive array. In addition, a lookup table based fusion is used with the dual-modality sensor array.

Imaging with different sensor arrays has been evaluated. The ring array is suitable for imaging floating MUTs in the transmission mode, and has a spatial resolution of one

sensing element, a position resolution of half a sensing element. The adaptive array is better used with normal tomography scan, and has a spatial resolution and a position resolution of half a sensing element. The single-electrode sensor array is better used with adaptive scan, and is more suitable for imaging grounded MUT than the ring array in shunt mode. The coil sensor array has a spatial resolution of one sensing element, and a position resolution of half a sensing element. Image reconstruction by interpolation based on sensitivity coefficients can deliver similar results to tomographic imaging, but requires much less computation and does not distort the shape of MUT. It can be a good alternative for imaging with planar sensors. The dual-modality array can provide complementary measurements, so that the effect of conductivity can be decoupled from the capacitance measurements. By the lookup table based fusion, permittivity/conductivity/permeability images can be generated from C/R/X images, which is a more accurate representation of material property distribution.

Declaration

No portion of the work referred to in the thesis has been submitted in support of an application for another degree or qualification of this or any other university or other institute of learning.

Copyright statement

i. The author of this thesis (including any appendices and/or schedules to this thesis) owns any copyright in it (the "Copyright") and s/he has given The University of Manchester the right to use such Copyright for any administrative, promotional, educational and/or teaching purposes.

ii. Copies of this thesis, either in full or in extracts, may be made **only** in accordance with the regulations of the John Rylands University Library of Manchester. Details of these regulations may be obtained from the Librarian. This page must form part of any such copies made.

iii. The ownership of any patents, designs, trademarks and any and all other intellectual property rights except for the Copyright (the "Intellectual Property Rights") and any reproductions of copyright works, for example graphs and tables ("Reproductions"), which may be described in this thesis, may not be owned by the author and may be owned by third parties. Such intellectual Property Rights and Reproductions cannot and must not be made available for use without the prior written permission of the owner(s) of the relevant Intellectual Property Rights and/or Reproductions.

iv. Further information on the conditions under which disclosure, publication and exploitation of this thesis, the Copyright and any Intellectual Property Rights and/or Reproductions described in it may take places is available from the Head of School of Electrical and Electronic Engineering.

Acknowledgements

First of all, I would like to thank my parents for their unconditional love and immense support throughout my life. I am also in debt to my fiancée, Dandan Wu, for her love, support and understanding.

I am extremely grateful to my supervisor, Prof. Wuqiang Yang, for his guidance and encouragement throughout the course of my PhD study.

I would like to thank Dr. Bin Cheng and Dr. Min Yang for their contributions to the hardware and software designs, thank Dr. Yi Li and Dr. Haigang Wang for interesting and fruitful discussions, and thank Derrick in the workshop for assisting the construction of the system.

Members in SISP group and all my other friends are also thanked for the fun I have outside research work. I especially would like to thank Terry and Ella for their help and care during my stay in the UK.

Finally, I would like to thank ICIR Inc in USA and Schlumberger Cambridge Research in the UK for collaboration and financial support, and thank UK ORS Award and the University of Manchester for providing tuition fees.

Publications

[1] Hu X H and Yang W Q (2009), Planar capacitive sensors – a review of design and applications, *Sensor Review,* Accepted

[2] Hu X H and Yang W Q (2009), An imaging system with planar PCB-coil sensor array, *IEEE International workshop on Imaging Systems and Techniques*, Shenzhen, China, May 10-12, pp

[3] Hu X H, Yang M, Li Y, Yang W Q and de Lara M M (2008), An impedance-analyser-based multi-channel imaging system and its applications, *IEEE International workshop on Imaging Systems and Techniques*, Chania, Crete, Greece, Sept. 10-12, pp 181-186

Other publications during the course of PhD research:

[4] Hu X H, Katsouros M, Yang W Q and Huang S M (2007), Further analysis of charge/discharges capacitance measuring circuit used with tomography sensors, *Sensors & Transducers Journal*, 80 (6), pp 1246-1256

[5] Hu X H, Yang M and Yang W Q (2007), Design of twin-plane sensor with internal electrodes for flow measurement, *5th World Congress on Industrial Process Tomography*, Bergen, Norway, Sept. 3-6pp 568-576

[6] Hu X H and Yang W Q (2006), Design of a data acquisition and function generation unit with USB, *Measurement Science and Technology*, 17, N17-N23

Acronyms and symbols

Acronyms:

ABB	auto-balancing-bridge
AE	area error
CMOS	Complementary Metal-Oxide Semiconductor
CDC	capacitance-to-digital converter
DLL	Dynamic Link Library
DUT	device under test
ECT	electrical capacitance tomography
EIT	electrical impedance tomography
EM	electro-magnetic
EMT	electrical magnetic tomography
ERT	electrical resistance tomography
FEM	finite element modelling
FR4	Flame Retardant 4
GMR	Giant Magnetoresistance
GUI	Graphical User Interface
IC	integrated circuit
IEEE	Institute of Electrical & Electronics Engineers
I-V	current-to-voltage
LBP	linear back projection
LF	low-frequency
MUT	material under test
MUX	multiplexer
N/A	not available
NDT	non-destructive testing
NI	national instrument
NPN	Negative-Positive-Negative
PC	Personal Computer
PCA	principle component analysis

PCB	printed circuit board
PCI	Peripheral Component Interconnect
PE	position error
PSoC	programmable-system-on-chip
RF	radio-frequency
SNR	signal-to-noise ratio
SQUID	Superconducting Quantum Interference Device
SVP	sensitivity variation parameter
TF	terahertz-frequency
USB	universal serial bus
VCCS	voltage controlled current source
4TP	four-terminal-pair
Σ-Δ	sigma-delta

Symbols:

A	cross-sectional area of the coil
A'	area of MUT in image
A	true area of MUT
A_{pixel}	effective area of pixel
AE	Area error
B	susceptance
B	magnitude of magnetic flux density
B_{total}	magnitude of total magnetic flux density
B'	magnitude of perturbation magnetic flux density
B_0	magnitude of primary magnetic field density
C	Capacitance
C_f	feedback capacitor
C_{ds}	capacitance between driving and sensing electrode
C_{dm}	capacitance between driving electrode and MUT
C_{mg}	capacitance between MUT and ground
C_{sm}	capacitance between sensing electrode and MUT
C_S, C_{S1}, C_{S2}	Stray capacitance

C_x	unknown capacitance
C_{drive}	parasitic capacitance in driving coil
C_{pick}	parasitic capacitance in pickup coil
$C'(\bar{x}', \bar{y}')$	centre coordinates of MUT from image
$C(x, y)$	true centre coordinates of MUT
D	dissipation factor
E	magnitude of electric field
$E_{D,j}$	electric field in a voxel resulting from driving electrode
$E_{S,j}$	electric field in a voxel resulting from sensing electrode
G	conductance
H	magnitude of magnetic field
$H_{d,j}$	magnetic field in a voxel resulting from driving coil
$H_{p,j}$	magnetic field in a voxel resulting from pickup coil
H_{CUR}	high current terminal
H_{POT}	high potential terminal
I, I_x, I_o, I_s	electric current
I_{drive}	electric current in the driving coil
I_{pick}	electric current in the pickup coil
L	inductance
L_P, L_{P1}, L_{P2}	parasitic inductance
L_{CUR}	low current terminal
L_{POT}	low potential terminal
M	number of pixels
M_{12}, M_x	mutual inductance
N	number of turns in coil
N_p	number of pixel
$\boldsymbol{P}$	projection operator
P	sensing space
Q	electric charge
Q	resonant factor
R	resistance
R_D	resistance in the oscillation loop
R_P	parasitic resistance

R_{drive}	parasitic resistance in driving coil
R_{pick}	parasitic resistance in pickup coil
R_f	feedback resistor
S	Siemens
S	sensitivity (distribution)
$S_{\varepsilon,dev}$	standard deviation of sensitivity distribution
$S_{\varepsilon,avg}$	average of sensitivity distribution
S^{-1}	inverse of sensitivity distribution
S^T	transpose of sensitivity distribution
T	Period $1/f$
V	electric potential
V'	induced electric potential
V_c, V_i	input voltage
V_D	electric potential on driving electrode
V_S	electric potential on sensing electrode
V_x	voltage output
X	reactance
X_D	reactance of coil
X_C	reactance of capacitor
Y	admittance
Z	impedance
Z_d	impedance of driving coil
Z_p	impedance of parasitic in signal path
Z_s	impedance of parasitic capacitance
Z_x	impedance of DUT
Z_{mea}	measured impedance
a	radius of coil
d	differential operator
f	frequency in Hertz
g	normalised distribution of material
$\hat{g}$	reconstructed image representing distribution of material
$\hat{g}_B$	reconstructed binary image
i, j	spatial index

j	imaginary unite $\sqrt{-1}$
l	lift-off of MUT
n	number of turns
p	index of pixels
r	position vector
s_ε	sensitivity
t	thickness of MUT
t	image threshold
x	x-axis of Cartesian coordinate system
y	y-axis of Cartesian coordinate system
z	z-axis of Cartesian coordinate system
$\bar{x}'$	averaged x coordinates of MUT in image
$\bar{y}'$	averaged y coordinates of MUT in image
Φ	magnetic flux vector
$\Phi(r)$	spatial electrical potential distibution
Γ	electrode surface
Ω	ohm
α	relaxation factor in Landweber iteration
μ	permeability
μ_0	permeability of free space
μ_r	relative permeability
λ	normalised measurement vector
ε	permittivity
ε_0	permittivity of free space
ε_r	relative permittivity
σ	conductivity
θ	phase angle
ω	frequency in rad/s
v_j	volume of voxel
∇	gradient operator

Chapter 1 Introduction

This chapter presents a brief introduction to the research carried out in this thesis. The first section presents a general background for security screening systems and explains the motivations for this research. The second section outlines the research aims and objectives. The final section presents the structure and organisation of the thesis.

1.1 Background and Motivation

1.1.1 Background

Security screening systems are widely deployed at public transportation portals or sports centres for the detection of concealed weapons, explosives or drugs. To cope with the increasing challenges from terrorist threats, new security screening techniques are in high demand. In general, security screening systems can be categorised into three different types (Singh and Singh 2003): (1) bulk detection, (2) trace/vapour detection, and (3) human screening.

Bulk detection systems are mainly used for scanning luggage, cargo, containers or vehicles. Radioactive sources, such as neutrons (Gozani 1997, Buffler 2004), gamma-ray (Gozani *et al.* 2003) and x-ray (Murray *et al.* 1997), are commonly used in those systems for bulk imaging, from which the threat object can be identified. While images with high resolution can be produced, such systems usually pose safety concerns due to the use of radioactive sources.

Trace/vapour detection systems are mainly used for the detection of explosives or drugs by chemical analysis (Moore 2004) instead of imaging. Such systems can detect small quantities of target substances left on the luggage or evaporated in the air. To perform such analysis, samples may need to be taken by security staff. As many explosive materials have frequency signatures in the Terahertz range (Federici *et al.* 2005), THz technology can also be used for detecting explosives or drugs.

Human screening systems include conventional walk-through/hand-held metal detectors and human imaging systems. The walk-through/hand-held detectors (Rapidscan Systems 2009) can trigger an alarm to indicate the potential presence of a threat object, which is then accompanied with addition body search by security staff. A significant problem with such detectors is that threat objects such as ceramic knife or plastic explosives cannot be detected because they are not metallic. To avoid body search, human imaging systems have been under rapid development in recent years in the areas of infrared imaging (Kong *et al.* 2004), THz imaging (Federici *et al.* 2005) and millimetre-wave imaging (Sinclair *et al.* 2000). Such systems can generate images that can see through the clothing of a person so that a concealed weapon can be detected. However, such systems may pose privacy concerns as the person being scanned may appear naked in the image.

This thesis is mainly concerned with the improvement of human screening systems. A common problem with both metal detectors and human imaging systems is that they cannot effectively detect threat objects hidden in shoes. It is often seen in the airport that passengers need to remove their shoes, put them through the x-ray detector, and walk through security check point with bare feet. Such a process is inconvenient and may cause significant delay to passengers. Therefore, a supplementary tool is needed for detecting threat objects hidden in shoes without removing them.

Another area of interest is security screening in the post-office. Although mail and deliveries have long been used to transport threat objects (Centre for Protection of National infrastructure 2009), unfortunately, there is no effective security screening system used in the post-office so far. A security scanner for checking envelopes or small parcels would help to identity threat objects and greatly reduces the risk of terrorist attack.

Different sensing modalities have been used for security screening, which cover nearly the full frequency spectrum, from nuclear, X-ray, infrared, THz, millimetre wave, down to RF reflectometry (Seward and Yukl 1991) and LF dielectrometry (Sears 2001). Fig. 1.1 shows the frequency spectrum with typical applications in different frequency bands. Amongst the available sensing modalities, electro-magnetic (EM) sensing in the

low frequency (LF) range (below 10 MHz) has the advantages of low cost, fast response and intrinsically safe. However, it is relatively less exploited for use in security screening than the higher frequency modalities.

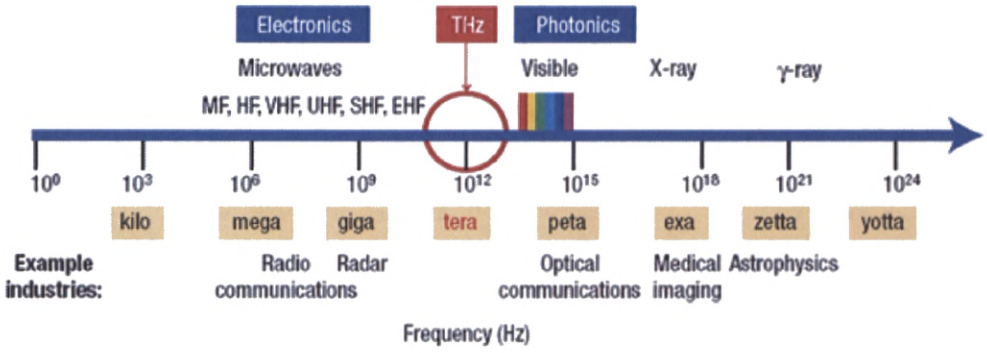

Fig. 1.1 Electromagnetic spectrum (Ferguson and Zhang 2002)

Sears (2001) reported an explosive detection system based on Dielectrometry. Interdigital capacitive sensors with varying electrode spacing are used to obtain complex dielectric measurements of a sample. Model-based parameter estimation is carried out to identify target materials using a pre-computed database of sensor responses to different materials. However, the performance of material identification is influenced by a number of factors, such as noise in the measurement and the position of the sample. Schliker (2004) reported a system for imaging buried object using a capacitive and inductive sensor array. This sensor array has a unique design which uses a single driving winding/electrode and multiple sensing elements so that the sensor array can work in the capacitive mode and inductive mode alternatively. Model-based imaging is carried out to generate images of absolute electrical properties using pre-computed measurement grid/lookup table and inverse interpolation (Schilker 2006). Although this system can obtain capacitive and inductive measurements, fusion is not implemented yet. A constraint of the model-based parameter estimation and imaging used in these two systems is that it is difficult and time consuming to obtain the measurement grid/lookup table. However, as the inverse interpolation is relatively simple, parameter estimation and imaging can be implemented online if the measurement grid is provided.

Gonzalez-Nakazawa (2007) developed a portable scanner to detect concealed weapons using two parallel rows of solenoids. Imaging is carried out off-line using electro-magnetic tomography (EMT). Compared with the conventional metal detectors, this system can generate conductivity/permeability images simultaneously, from which the position of the metallic object can be located. However, the shape of the object in the reconstructed image is distorted, and is highly dependent on its position in the sensing space. In addition, this system cannot detect non-metallic threat objects.

Cheng (2008) developed a number of scanners based on different planar capacitive senor arrays, including a laptop-based portable envelope scanner and a PC-based foot scanner using concentric ring sensor arrays, and a luggage scanner using two parallel sensor boards with square electrodes. Online imaging is carried out using the interpolation method for the ring sensor arrays, while off-line imaging is carried out using electrical capacitance tomography (ECT) for the square-electrode array. Capacitive-sensor-based systems can detect non-metallic threat objects, such as a ceramic knife. However, the performance of systems is influenced by conductivity and the potential boundary conditions in the system, which needs to be further investigated. As capacitive and magnetic sensors can provide complementary information for a sample, it is of interest to investigate dual-modality imaging using capacitive and magnetic sensor arrays.

1.1.2 Motivations

Concluding from the above, the motivations of this thesis are originated from two aspects. From security screening system point of view, a low-cost system for scanning shoes, envelopes and smaller parcels is needed. From a sensing modality point of view, imaging with capacitive and magnetic sensor arrays operating in the LF range is to be further exploited.

1.2 Aim and objectives

This thesis aims to develop an imaging system based on capacitive and magnetic sensor arrays for security scanning of shoes, envelopes and small parcels. The research objectives are:

- Further investigation of features of planar capacitive and magnetic sensors,
- Designing planar capacitive, magnetic and dual-modality sensor arrays,
- Designing imaging system to obtain measurements from capacitive and magnetic sensors,
- Designing suitable image reconstruction and fusion algorithms for capacitive and magnetic sensors
- Evaluating the performance of the imaging system

There are a number of novel aspects in this research, including:

- Comprehensive investigation of planar capacitive sensors from design to application
- Multi-channel multi-modality imaging system based on an impedance analyser
- Imaging with different planar capacitive sensor arrays and planar PCB-coil arrays
- Imaging and fusion with dual-modality planar capacitive and coil sensor array

1.3 Organisation of thesis

The research background, aims and objectives are introduced as presented in Chapter 1. The rest of the thesis is organised as follows.

Chapter 2 reviews the design and applications of planar capacitive and magnetic sensors in terms of their sensing principles, key issues in sensor design, performance evaluation and applications. The detailed research directions in this thesis are identified.

Chapter 3 presents the design of single-modality and dual-modality sensor arrays. The performance of the sensor arrays are evaluated experimentally in terms of dynamic range, sensing depth and cross-talk.

Chapter 4 presents the design and evaluation of a multi-channel, multi-modality imaging system based on an impedance analyser, HP4192A. Image reconstruction and fusion are reviewed, and suitable algorithms are developed.

Chapter 5 presents the imaging results and analysis for all the sensor arrays. The performance of the sensor arrays are qualitatively analysed in terms of edge detection and spatial resolution, and quantitatively analysed in terms of position and area estimation. Fusion results based on the dual-modality sensor array are also presented.

Finally, Chapter 6 presents the conclusions from this research, and gives suggestions for future research.

Chapter 2 Review of planar capacitive and magnetic sensors

Imaging with capacitive and magnetic sensors is investigated. In particular, the planar sensor structure is of interest, because they can provide one-sided access to the material under test (MUT), which is well suited for easy and convenient scanning of shoes, envelopes or small parcels. While the conventional capacitive and magnetic sensors have been extensively studied, the planar structure poses additional challenges in sensor modelling and design. This chapter presents a review for planar capacitive and magnetic sensors in terms of their sensing principles, key issues in sensor design, performance evaluation and applications, from which the novelties and research directions are identified.

2.1 Planar capacitive sensors

Capacitive sensors have been used in a wide range of applications due to their features of low cost, fast response, non-intrusive and non-invasive, no radiation and flexibility in electrode design (Huang *et al.* 1989, Xie *et al.* 1990). In a planar capacitive sensor, the sensor electrodes are placed in a co-planar plane. Apart from the above common features, the planar structure provides a possibility to interrogate an MUT from only one side (Mamishev *et al.* 2004), which is particularly useful when the access to the MUT is limited. These additional features make planar capacitive sensors a popular option for applications in proximity/displacement detection (Chen *et al.* 1998), intelligent human interfacing (Smith *et al.* 1998), non-destructive testing (NDT) (Diamond *et al.* 2006), material characterisation (Mamishev *et al.* 2004) and imaging (Frounchi *et al.* 2003, Cheng 2008). On the other hand, the planar structure complicates sensor design, especially with different properties of the MUT and conditions.

Some work has been done in design and evaluation of planar capacitive sensors. A rectangular-shaped sensor array (Shi *et al.* 1991) and a comb-shaped sensor array (Wang *at al.* 1996) were studied for multi-interface detection between air/oil/water, showing that an optimal set of structural parameters can be used to achieve the desired sensitivity and linearity. For NDT and material characterisation, Igreja (2004) studied

the design issues for an inter-digital sensor using an analytical method. Li (2006) used a numerical method to study a concentric ring sensor, with an emphasis on the effects of shielding and substrate thickness. General design principles are given by Igreja and Li for their respective sensors. For proximity or displacement measurement related applications, the existing studies mainly focus on conductive MUT. For example, Chen (1998) used an analytical method to study the performance of a concentric ring shaped sensor for proximity detection of a grounded metal disk, where the influence of electrode size, shape and geometry was considered. Using a numerical method, Zoethout (2003) studied a rectangular shaped planar sensor for displacement measurement of a grounded spindle, and also compared the performance of the sensor used with different material properties and boundary conditions. With a single-electrode array, Lee (1999) studied the performance of a capacitive fingerprint sensor, where the sensor output against the distance between the finger and the sensing chip was studied.

In the context of characterisation and imaging of a dielectric MUT with different boundary conditions, however, a systematic study of sensor modelling, features and design issues is needed. In addition, the influencing factors on sensitivity distribution, and the effect of conductivity on sensor performance have not been studied for planar capacitive sensors.

In this section planar capacitive sensors are discussed in terms of their sensing mechanism, key issues in sensor design and evaluation, with a focus on characterisation and imaging of dielectric MUTs. A numerical method is used to investigate the sensor response under different conditions, and to derive sensitivity distributions. The applications of planar capacitive sensors are summarised according to sensor features and different methods for image reconstruction.

2.1.1 Principle of capacitive sensing and different modes for planar sensors

The principle of capacitive sensing is based on the interaction between an MUT and the interrogating electric field. An electric field generated from sensor electrodes penetrates through an MUT, and causes electric displacement within the MUT to counter the applied field. This displacement field changes the charge stored between the sensor

electrodes, and thus alters inter-electrode capacitance, which in turn can be used to infer the properties of the MUT, such as permittivity, conductivity and their distributions, and ultimately to derive the system variables that can be related to those properties.

For capacitance measurement, an electrical stimulus is applied to a driving electrode while a measurement is taken from a sensing electrode. Usually, the frequency of the electrical stimulus, and thus the generated electric field, is limited. For example, the frequency range of the state-of-the-art Agilent precision impedance analyser 4294A is between 40 Hz to 110 MHz (Agilent Technologies 2008 1). In this frequency range, an MUT can be mainly characterised by its static relative permittivity and conductivity (Da Silva 2008). The interaction between an MUT and electric field can be described by the Laplace equation for electro-static or electro-quasi-static approximation, assuming no free charge in the sensing space (COMSOL 2008).

$$\nabla\left(\left(\sigma(r)+\varepsilon_0\varepsilon(r)/T\right)\nabla\Phi(r)\right)=0 \tag{2.1}$$

$$\nabla\left(\left(\sigma(r)+j\omega\varepsilon_0\varepsilon(r)/T\right)\nabla\Phi(r)\right)=0 \tag{2.2}$$

where r is the position vector, $\sigma(r)$ is the spatial conductivity distribution, ε_0 is the permittivity of vacuum, $\varepsilon(r)$ is the spatial relative permittivity distribution, $\Phi(r)$ is the spatial electric potential distribution, ∇ is a gradient operator, T is the time constant for electro-static approximation, and ω is the angular frequency of the electric field.

In equation (2.1) the electro-statics formulation is approximated for conducting and dielectric materials. In equation (2.2) the electro-quasi-statics formulation is approximated for conducting and dielectric materials with small currents and a negligible coupling between the electric and magnetic fields.

When electric potentials are applied to a sensing system, including sensor electrodes and an MUT, a specific set of boundary conditions is defined. By solving the field equations with the imposed potential boundary conditions, the relationship between

capacitance of any pair of electrodes and distributions of permittivity and conductivity in the system can be derived by (Yang and Peng 2003)

$$C = \frac{Q}{V} = -\frac{1}{V}\oint_{\Gamma}(\sigma(r) + \varepsilon_o \varepsilon(r))\nabla\Phi(r)d\Gamma \qquad (2.3)$$

where V is the electric potential difference between a pair of electrodes and Γ is the electrode surface.

2.1.2 Planar sensor structure and different sensing modes

Conventionally, a capacitor is in the form of a parallel-plate, where the driving and sensing electrodes are placed opposite to each other in close proximity. An electric field is uniformly distributed between them. When the electrodes gradually open up, the electric field is no longer confined within a small region between electrodes, but expanded into a wider space and forms a fringe field. When the electrodes are open up to a co-planar plane, the fringe field becomes predominant between the driving and sensing electrodes. This type of sensor is called planar sensor in literature. The transition from a parallel-plate capacitor to a co-planar sensor with the consideration of the fringe effect is illustrated in Fig. 2.1 (Mamishev *et al.* 2004). The planar structure provides a possibility to interrogate an MUT from only one side (Mamishev *et al.* 2004), which is particularly useful when access to both sides of the MUT is limited. For example, to inspect the surface or internal properties of a large mechanical structure, sensor electrodes can only scan over its surface to acquire information. To scan a foot with a shoe on, electrodes can only be placed on the bottom of the shoe. The associated design issues for planar sensors are more complicated than conventional capacitance sensors.

From equation (2.3), the value of the inter-electrode capacitance depends on the geometry of the sensor and the MUT, permittivity and conductivity distributions in the system, as well as potential boundary conditions. This means that an inter-electrode capacitance can change with an MUT being dielectric or conductive, floating or grounded. When an MUT is surrounded by sensor electrodes, the system boundary

conditions are specified by the status of the sensor electrodes. For a planar capacitance sensor, however, as only one side of an MUT is influenced by the sensor electrodes, the potential boundary conditions and the resulting inter-electrode capacitance can change dramatically.

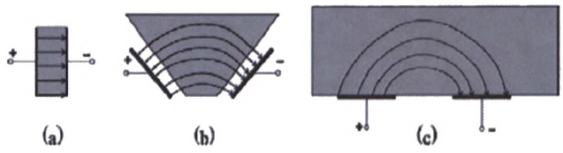

Fig. 2.1 Transition from parallel-plate to fringe field sensor: (a) parallel-plate capacitor whose (b) electrodes open up to provide (c) one-sided access to MUT

According to the potential boundary conditions of an MUT, planar capacitive sensors can be categorised into three different sensing modes: (1) transmission mode for a floating MUT, (2) shunt mode for a grounded MUT and (3) single-electrode mode with an MUT used as a virtual electrode in a capacitor. To further explain the sensor response and design issues for different sensing modes, it is necessary to review the general aspects of sensor design issues and parameters for performance evaluation.

In the transmission mode, an MUT is floating. Although the electrical properties of the MUT may change the distribution of the electric field in the system, the sensor can be modelled as a two-terminal system with three capacitors: (1) a capacitor between the driving and sensing electrodes, C_{ds}, (2) a capacitor between the driving electrode and the MUT, C_{dm} and (3) a capacitor between the sensing electrode and the MUT, C_{sm}. The sensor model and an equivalent circuit for the planar capacitive sensor in the transmission mode are shown in Fig. 2.2.

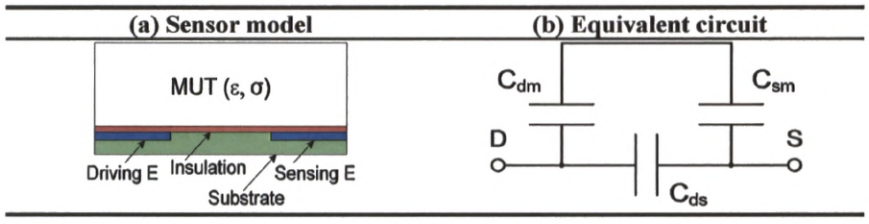

Fig. 2.2 Sensor model and equivalent circuit for transmission mode

In the shunt mode, an MUT is grounded. It affects the capacitive coupling in the system by drawing electric field lines away from the sensing electrode, and thus, reduces the inter-electrode capacitance. The sensor can be modelled as a three-terminal system with three capacitors: (1) a capacitor between the driving and sensing electrodes, C_{ds}, (2) a capacitor between the driving electrode and the MUT, C_{dm} and (3) a capacitor between the sensing electrode and the MUT, C_{sm}. When the MUT is at a low potential instead of ground, such as a human body (Cheng 2008), the sensor can also be described by the shunt mode. The equivalent circuit in this case includes an additional capacitor between an MUT and ground, C_{mg}. The sensor model and the equivalent circuits for the planar capacitive sensor in the shunt mode are shown in Fig. 2.3.

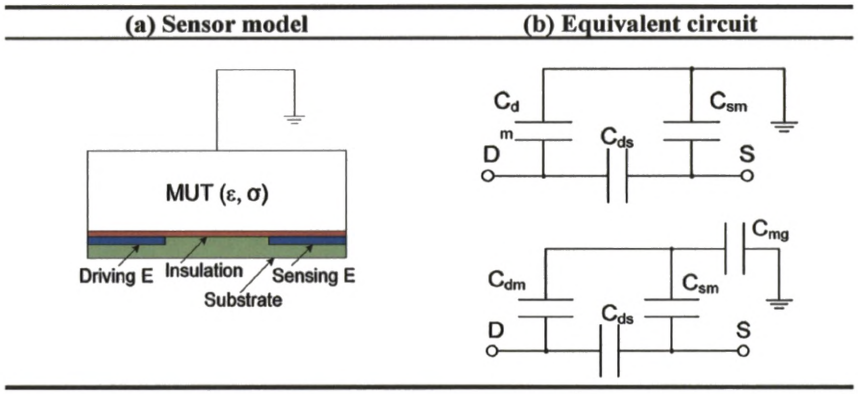

Fig. 2.3 Sensor model and equivalent circuit for shunt mode

In the single-electrode mode, an MUT is grounded, and is used as a virtual electrode. The electric field lines start from the driving electrode and terminate on the grounded boundary of the MUT. Therefore, the sensor can be modelled as a capacitor between the driving electrode and MUT, C_{dm}. When the MUT is at a low potential, the sensor can also be described using the single electrode mode. The equivalent circuit in this case includes an additional capacitor between MUT and ground, C_{mg}. The sensor modeland equivalent circuit model for a planar capacitive sensor in the transmission mode are shown in Fig. 2.4.

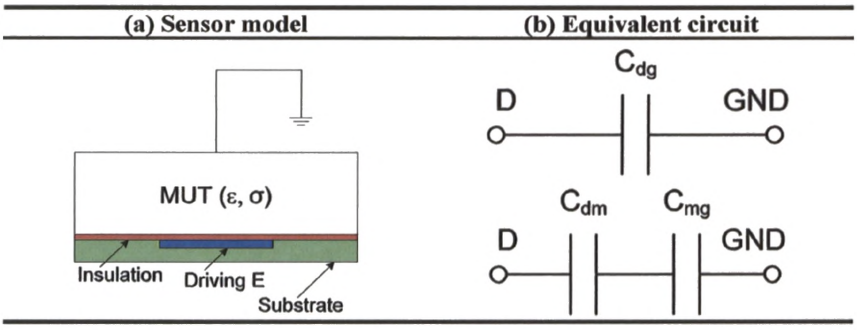

Fig. 2.4 Sensor model and equivalent circuit for single-electrode mode

2.1.3 Key issues for sensor design, performance evaluation and considerations for instrumentation

There are a number of issues in sensor design and several parameters for the evaluating the performance of a sensor. One design issue may influence the sensor performance in several aspects. On the other hand, more than one design issues may have to be considered together to achieve the desired sensor performance. Therefore, it is important to understand how the design issue influences the sensor performance, so that a sensor can be optimised for a specific application. In addition, instrumentation-related issues need to be considered to obtain the correct measurements from a sensor. The key issues in sensor design and construction, parameters for performance evaluation and instrumentation-related issues are summarised in the following.

A. Sensor design

The key design issues for a planar sensor include the number of electrodes and their arrangement, geometry of electrodes, shielding and guarding. These parameters will be briefly explained below.

Number of electrodes and their arrangement depend on the number and complexity of the system variables to be solved for an application. It requires the understanding of the relationship between the capacitance measurements and system variables. For a simple application, such as proximity or displacement measurement, where there exists a direct relationship between the capacitance measurements and the distance of an MUT, a single sensing element, such as a concentric ring sensor, would be sufficient.

For more complex situations, such as imaging or NDT-related applications, a sensor array may be used, and the arrangement of electrodes in the sensor array may need to be considered. The arrangement of electrodes also depends on the available space in the system to place the electrodes.

Geometry of electrodes includes the shape, spacing and separation of electrodes, which are the most important parameters to determine the sensor performance (Li *et al.* 2006). The shape of electrodes can be in a simple form, such as a square, rectangular, round or ring shape, or in a complex form, such as a comb or spiral shape. The spacing between electrodes refers to the distance between the centres of two adjacent electrodes. The separation of electrodes refers to the width of the empty space between the adjacent electrodes. The geometry of electrodes influences the sensor performance in signal strength, penetration depth and measurement sensitivity.

Shielding and guarding can be used for shaping the electric field (Quantum Research Group 2005), and more importantly for eliminating stray capacitance and noise from an unwanted region (Li *et al.* 2006). Different types of shielding and guarding methods may be used, depending on the capacitance measuring circuit. Usually, a shield is held at a ground potential. Shielding can be placed in between the electrodes or beneath the substrate as a backplane (Li *et al.* 2006). Active-guarding is another commonly used method in capacitance measurement, where a guard electrode is held at the same potential as the driving signal (Huang *et al.* 1988 2). Shielding and guarding are considered together with instrumentation related issues.

B. Sensor construction

An insulation layer is usually placed over the electrodes in a capacitance sensor to prevent the direct contact to an MUT. A sensor substrate is used as mechanical support. The issues in sensor construction include the choice of materials for electrodes, insulation layer, substrate, and a construction method. Electrodes are commonly made of a conductive material, such as copper. Dielectric materials are commonly used for the insulation layer and the substrate. The choice of material would affect the sensor performance by introducing additional uncertainty or drift in capacitance measurements.

It is desirable to use materials of low moisture absorption, so that its influence to measurements is minimal (Mameshev *et al.* 1998). The permittivity value for the sensor substrate and the insulation layer should be chosen to be as close to the value of the MUT as possible, so that the electric field in the system is the most uniform (Xie *et al.* 1990). The thicknesses of insulation layer and sensor substrate can influence the signal strength and sensitivity distribution, and thus need to be optimised (Li *et al.* 2006). Several sensor construction techniques, including MEMS (Chen *et al.* 1998), PCB and manual construction, can be chosen, depending on the dimension of the sensor and costs.

C. Key parameters for evaluation of sensor performance

To evaluate the performance of a sensor, the parameters to be considered include signal strength, dynamic range, linearity, penetration depth, measurement sensitivity and cross-talk. For imaging applications, further evaluation parameters need to be considered, including spatial/image resolution, sensitivity distribution and imaging speed.

Signal strength and dynamic range: The feature of a planar sensor is that the signal decreases exponentially in the z direction (Mamishev *et al.* 2004). The sensor output signal consists of a standing value and the dynamic changes due to the presence of an MUT. The standing value is the measurement from an empty sensor, which is often much larger than the dynamic range. For example, the standing capacitance is about one order larger than the changes in capacitance in an ECT sensor. One of the objectives in sensor design is to minimise the standing value and maximise the dynamic range, so that a maximum signal-to-noise ratio (SNR) can be achieved.

Linearity: Due to the soft-field nature, the response of a capacitance sensor to material properties is inherently non-linear (Yang and Peng 2003). However, for some applications, such as proximity or displacement measurement, there is an approximated linear region near the origin in the capacitance measurement (Chen *et al.* 1998). The linear range and slope of this approximated linear region determines the working range and sensitivity of a capacitance-based proximity sensor.

Penetration depth for a planar sensor can be defined as the maximum distance in the z direction for the sensor to produce a detectable change in the sensor output. It is an important parameter to indicate how far the sensor signal can reach. In literature, a threshold of 3% of the dynamic range is used to define the z distance as the penetration depth when an MUT is moving away from the sensor electrodes (see Fig. 2.5 (a)) (Li *et al.* 2006). It is also desirable to study how deep the electric field can penetrate into the MUT. In the same way, the penetration depth against the thickness of an MUT can be defined, as shown in Fig. 2.5 (b) (Da Silva 2008). In practice, the penetration depth is limited by the noise level of the instrumentation system, and affected by the spacing between the electrodes.

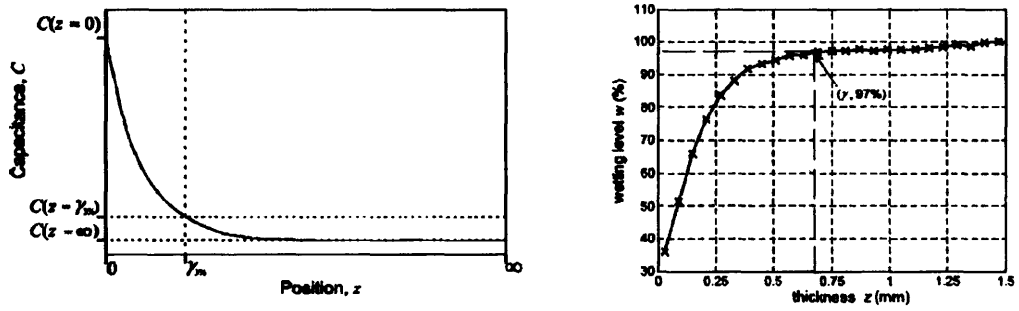

(a) C vs. MUT lift-off (Li *et al.* 2006)

(b) C vs. MUT thickness (Da Silva 2008)

Fig. 2.5 Effective penetration depth of a planar capacitance sensor against lift-off and thickness of MUT

In general, **sensitivity** is defined as the ratio of changes in the sensor output to changes in a system variable. The linearised sensitivity (i.e. neglecting the 2nd and higher order terms) for capacitance measurement can be written as (Yang and Peng 2003)

$$\Delta C = s_\varepsilon \Delta \varepsilon \tag{2.4}$$

where $s_\varepsilon = d\xi / d\varepsilon$ is the sensitivity of the capacitance transducer to changes in permittivity. One feature of capacitance sensors is that multiple system variables are

coupled in the inter-electrode capacitance, including permittivity (ε), conductivity (σ), lift-off (l) and thickness (t) of an MUT.

In NDT or imaging applications, **sensitivity distribution** can be obtained, and used to evaluate the sensor performance or used for image reconstruction. Among the available methods for obtaining the sensitivity distribution (Wajman *et al.* 2004), the numerical method based on the dot multiplication is a popular choice due to the advancement in computing and numerical modelling techniques (Li 2008). By modelling with high orders and using a fine mesh, a sensitivity distribution with high accuracy can be generated. Based on the superposition theory (Yang 2007), a sensitivity distribution for a complex electrode arrangement can also be generated. The 3D sensitivity distribution for a pair of driving and sensing electrodes can be derived by (Xie *et al.* 1990, Wajman *et al.* 2004)

$$S_{SD,j} = -\int_{P} \frac{E_{D,j}}{V_D} \cdot \frac{E_{S,j}}{V_S} dv_j \tag{2.5}$$

where $E_{D,j}$ and $E_{S,j}$ are the electric fields in a voxel j when potentials V_D on electrode D and V_S on electrode S are set and v_j is the volume of the j^{th} voxel and P is the sensing space.

The sensitivity distribution can be evaluated by the sensitivity variation parameter (SVP), as defined by (Xie *et al.* 1990)

$$SVP = S_{\varepsilon,dev} / S_{\varepsilon,avg} \tag{2.6}$$

where

$$S_{\varepsilon,avg} = \frac{1}{M} \sum_{j=1}^{M} S_{\varepsilon,j} \tag{2.7}$$

and

$$S_{s,dev} = \left(\frac{1}{M} \sum_{j=1}^{M} \left(S_{s,j} - S_{s,avg} \right)^2 \right)^{1/2} \qquad (2.8)$$

The smaller the SVP, the more homogeneous the sensitivity distribution is.

Cross-talk indicates the influence of a sensing element on its neighbouring elements, which should be kept minimal in practice. However, as a fringe field is dominant in planar sensors, unwanted coupling between different sensing elements is inevitable. Cross-talk can be reduced by placing a shield (Li *et al.* 2006) or by increasing the separation between different sensing elements, at the cost of weakened signal strength or poorer spatial resolution.

Spatial resolution refers to the smallest feature that can be detected by a sensing element. It depends on the geometry of the electrodes and their arrangement. **Image resolution** refers to the size of pixels in an image. It depends not only on the spatial resolution of the sensor, but also on the image reconstruction algorithm. In some applications, a measurement from each sensing element is directly mapped into a pixel in an image, such as in fingerprint imaging (Lee *et al.* 1999). In other applications, the sensitivity distribution is used to generate an image, where the number of pixels is larger than the number of measurements (Cheng 2008).

Imaging speed depends on the data acquisition speed of a measuring system and the algorithm for image reconstruction.

D. Instrumentation-related issues

The instrumentation-related issues include measurement protocol, stray-immunity and capacitance measuring method.

Measurement protocol refers to the pattern and sequence for energising the driving electrodes and taking measurements from the sensing electrodes. A number of measurement protocols can be implemented with a sensor array, e.g. a single electrode

or multiple electrodes can be used for either driving or sensing. Different measurement protocols can result in different sensor responses, acquisition time and different number of measurements. It can also result in redundant measurements due to symmetry in electrode arrangement. An optimal measurement protocol may be needed for a specific application.

Stray-immunity should be considered in a capacitance measuring circuit due to the existence of stray capacitance, which can be much larger than the sensor capacitance output itself (Yang 1996). Stray-immunity can be ensured by a stray-immune configuration or by using guard electrodes (Huang *et al.* 1988 2) (see Fig. 2.6).

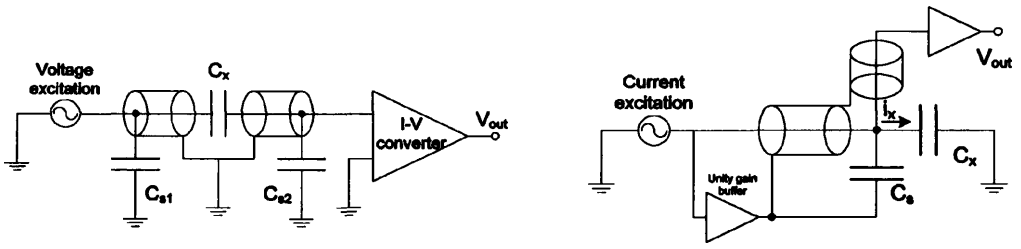

(a) Stray-immune configuration (b) Active guard

Fig. 2.6 Stray-immune methods for capacitance measurement

In a stray-immune circuit, a measuring electrode is held at virtual ground. The stray capacitance can be modelled as two capacitors, C_{s1} connected from the driving electrode to ground, and C_{s2} between the virtual ground and ground. C_{s1} will not affect the measurement because the current flowing through it does not contribute to the current to be measured. Also, C_{s2} will not affect the measurement because both its terminals are held at the ground potential. All the signal paths and electrodes should be protected by grounded shielding. In addition, both terminals of the unknown capacitor C_x can be committed into the measuring circuit.

In the active guard method, the influence of stray capacitance, C_s, is eliminated by the active guard, which is driven at the same potential as the excitation signal. A high-speed unity-gain buffer should be used to drive the active guard. The signal paths and unused electrodes should all be actively driven, so that unwanted capacitive coupling can be

eliminated (Quantum Research Group 2005). In addition, only one terminal from the unknown capacitor can be committed into the measuring circuit.

The commonly used **capacitance measurement methods** with the consideration of stray-immune configuration include (1) the charge transfer based techniques, e.g. charge/discharge circuit (Huang *et al.* 1988 2), (2) the auto-balancing-bridge based techniques, e.g. impedance analysers (Agilent Technologies 2008 2) and an AC-based ECT system (Yang and York 1999) and (3) the current-injection techniques (Nerino *et al.* 1997, Cypress Semiconductor 2007). Further details of those methods and their implementations will be discussed in Chapter 4. The charge/discharge and auto-balancing-bridge techniques use a stray-immune configuration, and can be used with a planar capacitive sensor in the transmission or shunt mode (further details to be discussed in the next part). The current-injection techniques use the active guard method, and can be used with a planar capacitive sensor in the single-electrode mode (further details to be discussed in the next part).

2.1.4 Sensor modelling, response and design guidelines

This part studies the sensor models, response features and design guidelines of planar capacitive sensors in different sensing modes. While analytical modelling can provide accurate solutions to sensors of simple geometries, numerical modelling is preferred to deal with varying design parameters and properties of MUT. In this work, a commercial finite-element modelling (FEM) package, COMSOL, is used for sensor modelling.

To understand the relationship between the design issues and the sensor performance, a concentric ring shape capacitance sensor is used in modelling and simulations. This sensor is chosen because of its symmetry in structure, so that sensor modelling can be simplified. Simulations were carried out using COMSOL 3.4 with a 2D axial symmetric electro-statics generalised module to calculate the sensor output with varying design parameters (e.g. the radii of the driving electrode, separation of electrodes, width of the sensing electrode and the distance of the backplane to electrodes). The concentric ring sensor has an insulation layer of 0.5 mm thickness, a sensor substrate of 5 mm thickness and copper electrodes of 0.1 mm thick sandwiched in between. The material chosen for

the insulation layer and sensor substrate is FR4, with a dielectric constant of 4.5 (Merkel *et al.* 2000). The electrode in the middle is used for driving while the ring electrode used for sensing. An MUT is placed in the upper half space (z >=0) and the backplane, if used, is on the bottom of the substrate. To examine the sensor response in relationship with the material properties, positions and design parameters, capacitance measurements are plotted against the variable in evaluation.

A. Transmission mode

To investigate the sensor response to electrical properties of the MUT, simulations were carried out demonstrate the potential and field distributions, and to find out the relationship between the inter-electrode capacitance and permittivity or conductivity of the MUT. Fig. 2.7 shows the potential and electric field distributions and Fig. 2.8 shows the absolute capacitance value vs. permittivity/conductivity. It can be seen that the inter-electrode capacitance increases with the increase in permittivity or conductivity, but the relationships are non-linear, due to the insulation layer used in the sensor. If the MUT is in direct contact with sensor electrodes, the capacitance will be proportional to the permittivity (Da Silva 2008).

To investigate the influence of the design parameters on the sensor performance, simulations were carried out to find out the relationship between the sensor output and different thicknesses and lift-off of the MUT. Fig. 2.9 shows capacitance measurement against a dielectric MUT with the consideration of varying design parameters.

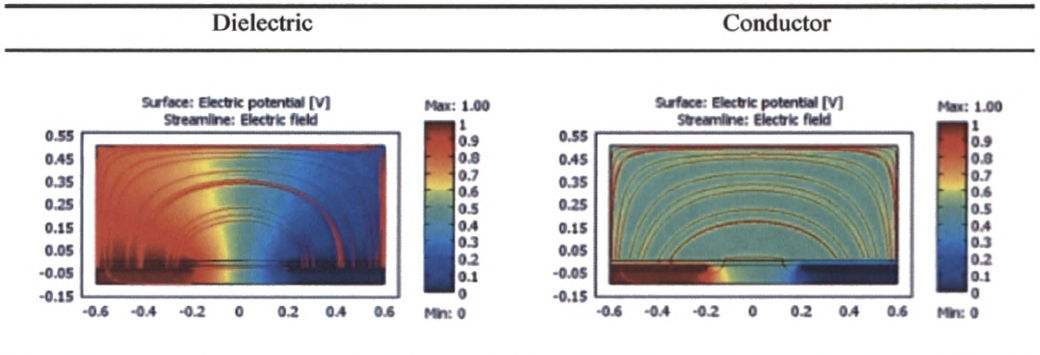

Fig. 2.7 Potential and electric field distributions for transmission mode

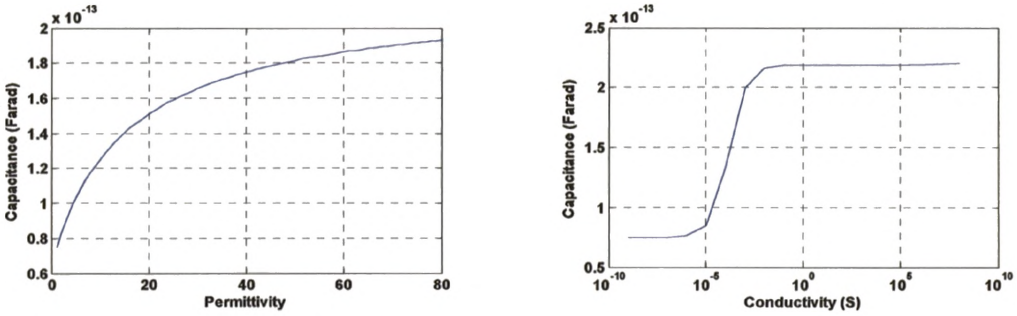

(a) C vs. varying permittivity with $\sigma = 0$ (b) C vs. varying conductivity with $\varepsilon = 1$

Fig. 2.8 Capacitance measurements in response to properties of MUT from concentric ring sensor in transmission mode (radii = 4 mm, ring width = 2 mm, separation = 2 mm, thickness of MUT = 11 mm, without backplane and inter-electrode shielding)

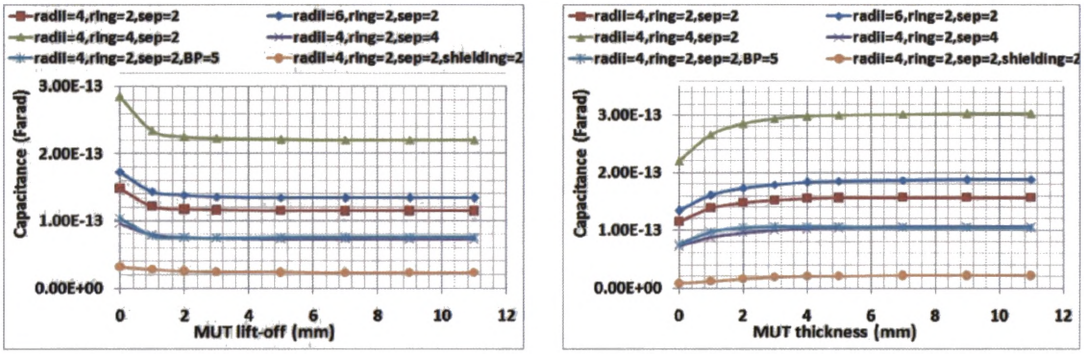

(a) C vs. lift-off of MUT (thickness = 2 mm) (b) C vs. thickness of MUT (lift-off = 0)

Fig. 2.9 Influence of design parameters on sensor response to dielectric MUT ($\varepsilon_r = 5$, $\sigma = 0$) in transmission mode

In the transmission mode, the inter-electrode capacitance decreases with the lift-off of MUT but increases with the thickness of MUT. Using a bigger driving electrode or sensing electrode can increase the signal level, dynamic range and sensing depth. However, increasing electrode separation results in a reduced signal level and dynamic range but an enhanced penetration depth. This means that there is a trade-off in determining the electrode size and separation, and thus an optimal ratio between these parameters are needed to achieve the best overall performance. In addition, the penetration depth is roughly ½ of the electrode spacing. The use of a backplane results in a reduced signal level, dynamic range and sensing depth. Therefore, it should be kept

a certain distance away from the sensor electrodes. The use of inter-electrode shielding also reduces the signal level and dynamic range, but enhances the sensing depth and significantly extends the approximated linear region near the origin. To achieve an optimal design, the electrode spacing should be determined at first according to the desired penetration depth. The use of backplane and shielding may be considered and an optimal ratio for electrode size and separation may be sought.

As the sensor output is directly related to the properties of the MUT, a planar capacitive sensor in the transmission mode is suitable for material characterisation, NDT, multi-interface sensing and tomography.

B. Shunt mode

To investigate sensor response to the properties of the MUT and design parameters, similar simulations were carried out. Fig. 2.10 shows the potential and electric field distributions and Fig. 2.11 shows the absolute capacitance vs. permittivity and conductivity of the MUT. In the shunt mode, the inter-electrode capacitance increases non-linearly with the permittivity or conductivity of the MUT when the values are low, but decreases sharply as their values continue to increase, because the higher the values of permittivity or conductivity, the more the field lines are drawn to the grounded boundary. It suggests that sensor performance in the shunt mode is similar to the transmission mode when the permittivity/conductivity of the MUT is low, but different when the permittivity/conductivity of the MUT is high. In addition, different permittivity or conductivity values could result in the same inter-electrode capacitance, which makes it more difficult to estimate the material properties.

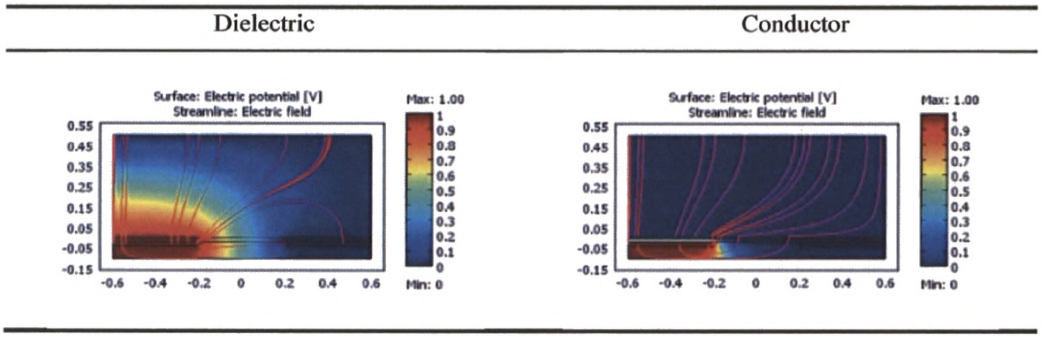

Fig. 2.10 Potential and electric field distributions for shunt mode

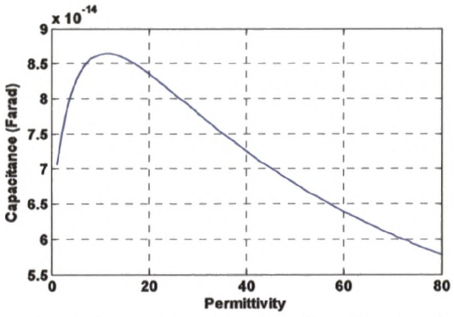

(a) C vs. varying permittivity when $\sigma = 0$

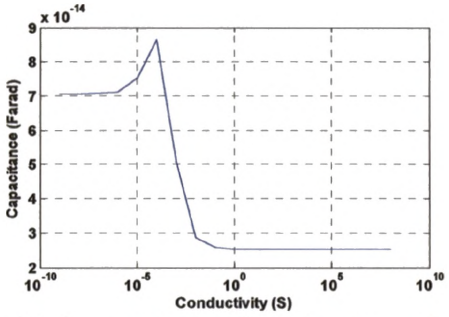

(b) C vs. varying conductivity when $\varepsilon = 0$

Fig. 2.11 Capacitance measurements in response to properties of MUT from concentric ring sensor in shunt mode (radii = 4 mm, ring width = 2 mm, separation = 2 mm, thickness of MUT = 11 mm, without backplane and inter-electrode shielding)

Fig. 2.12 shows capacitance measurements against a dielectric MUT with the consideration of varying design parameters. Unlike in the transmission mode, the inter-electrode capacitance in the shunt mode increases both with the lift-off and thickness of the MUT. The influences of electrode geometry and shielding are similar to those on the transmission mode. However, the penetration depth in the shunt mode is larger than in the transmission mode, which is roughly 1.5 times of the electrode spacing, because the grounded MUT makes the electric field lines penetrate deeper into the MUT. In addition, the approximated linear region near the origin is much larger, especially with the use of inter-electrode shielding. The design guidelines for a planar capacitive sensor in the shunt mode are similar to that in the transmission mode.

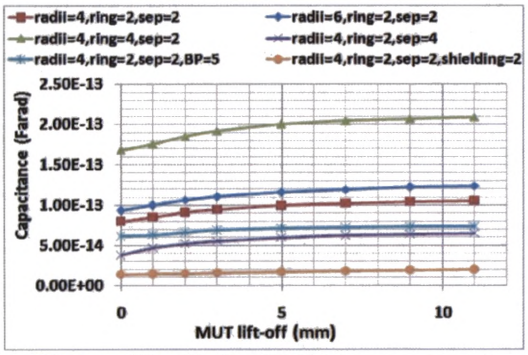

(c) C vs. lift-off of MUT (thickness = 2 mm)

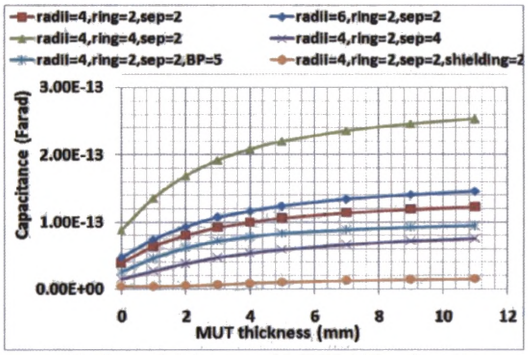

(d) C vs. thickness of MUT (lift-off = 0)

Fig. 2.12 Influence of design parameters on sensor response to dielectric MUT ($\varepsilon_r = 5$, $\sigma = 0$) in shunt mode

As the inter-electrode capacitance is not directly related to the electrical properties of the MUT, it is difficult to use a planar capacitive sensor in the shunt mode for material characterisation. On the other hand, the relevance of sensor output to the position of the MUT makes it more suitable for applications involving displacement or proximity measurement.

C. Single-electrode mode

To investigate the sensor response to the properties of the MUT and the design parameters, similar simulations were carried out. Fig. 2.3 shows the potential and field distributions and Fig. 2.14 shows the absolute capacitance against the permittivity and conductivity of an MUT. In the single-electrode mode, the measured capacitance increases non-linearly with the increase in the permittivity/conductivity of the MUT, which is similar to the transmission mode. However, the signal level is much larger because the capacitive coupling between the electrode and the MUT is stronger.

Fig. 2.15 shows the capacitance measurements against the lift-off and thickness of a dielectric MUT with the consideration of varying radii and separation. Unlike in the transmission or shunt mode, the active guard technique should be used in the single-electrode mode, because the MUT cannot be connected into the measuring circuit. To avoid the unwanted coupling, the unused electrodes are connected to an active guard. Therefore, the design parameters include only radii and separation.

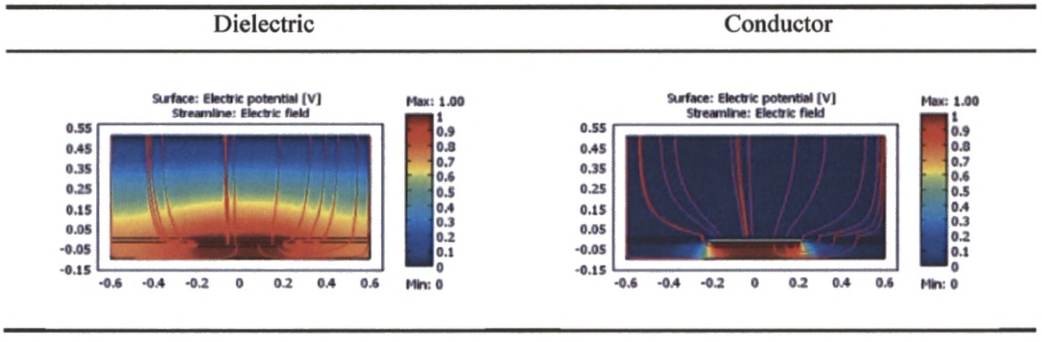

Fig. 2.13 Potential and electric field distributions for single-electrode mode

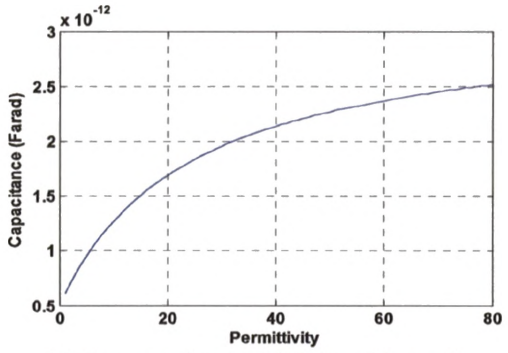

(a) C vs. varying permittivity with $\sigma = 0$

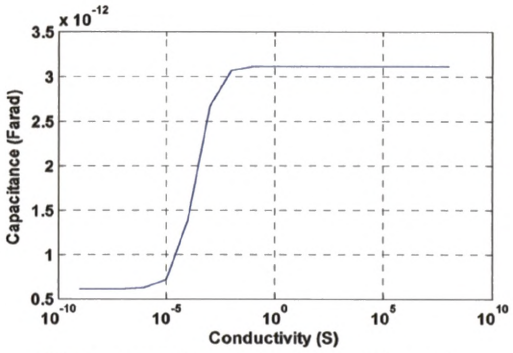

(b) C vs. varying conductivity with $\varepsilon = 1$

Fig. 2.14 Capacitance measurement in response to properties of MUT from concentric ring sensor in single-electrode mode, radii for driving electrode = 4 mm, thickness of MUT = 5 mm

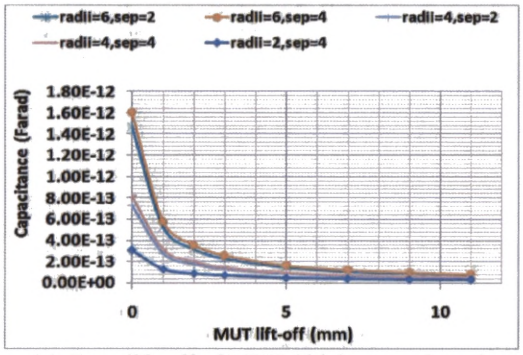

(e) C vs. lift-off of MUT (thickness = 2 mm)

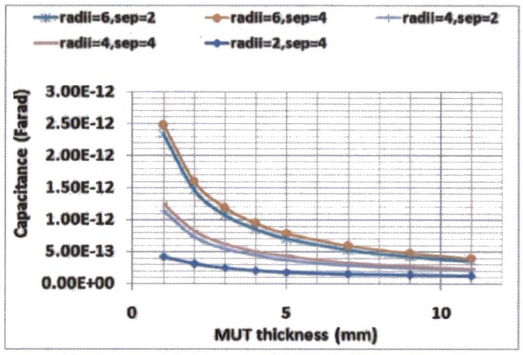

(f) C vs. thickness of MUT (lift-off = 0)

Fig. 2.15 Influence of design parameters on sensor response to dielectric MUT ($\varepsilon_r = 5$, $\sigma = 0$) in single-electrode mode

In the single-electrode mode, the inter-electrode capacitance decreases sharply with both the lift-off and thickness of the MUT. Using bigger electrodes can increase the signal level, dynamic range and penetration depth. Increasing separation also increases the signal level, dynamic range and penetration depth, because the active electrodes nearby will partly draw away the charge stored between the driving electrode and the MUT, and thus reducing the capacitance. The penetration depth is roughly 1 electrode spacing. To achieve an optimal design, the ratio between the electrode size and the separation needs to be considered.

As the sensor output is directly related to the properties and positions of the MUT, a planar capacitive sensor in the single-electrode mode can be used for both material characterisation and proximity/displacement measurement.

2.1.5 Sensitivity distributions

It is important to know the sensitivity distribution of a planar capacitance sensor. For non-imaging applications, the sensitivity distribution can be used to facilitate the sensor design and optimisation. For imaging applications, the sensitivity distribution is used for image reconstruction. The influencing factors on the sensitivity distribution, such as electrode shape, separation and shielding, will be examined here. SVP, as defined in the previous section, can be used to indicate how uniform the sensitivity distribution is, and how far the penetration depth is.

A. Shape of electrodes

The sensitivity distributions for electrodes of different shapes have been investigated, including square-spiral, comb, concentric ring and rectangular in the transmission or shunt mode, and square in the single-electrode mode. The same sensing space of $20\times20\times20$ mm^3 was used in simulation for each design, with electrodes placed in a plane $z = 0$, centred at (0, 0), and a separation of 2 mm. No back-plane or shielding is used. Fig. 2.16 (a) – (e) shows the electrode geometries, sensitivity distributions in XY plane and cross-sectional plane, and SVPs.

It can be seen that the high sensitivity values are mainly distributed along the gaps between the electrodes, with higher values around sharp corners than along smooth electrode boundaries. In addition, complex electrode shapes tend to have more uniform sensitivity distributions, but less penetration depth. A single-electrode sensor presents the most uniform sensitivity. Due to the symmetry in structure, the concentric ring electrode has a sensitivity distribution symmetrical along its z axis.

B. Separation of electrodes

To examine the influence of the separation of electrodes, the sensitivity distribution of the rectangular sensor with the doubled electrode separation (4 mm) was derived. The electrode geometry, sensitivity distributions and SVP are shown in Fig. 2.16 (f). It can be seen that a wider separation results in a deeper penetration depth and a more uniform sensitivity distribution over the whole sensing space. The rectangular sensor with a narrower electrode separation will have a much stronger local sensitivity, which may be good for displacement measurement over a small range near the electrodes. However, a uniform sensitivity is more desirable for imaging applications, because the reconstructed images will be less position dependent.

C. Backplane

Backplane is often used with planar capacitive sensors as a shield to minimise the interference of noise from the unwanted region. To investigate the influence of backplane, the sensitivity distribution of the concentric ring sensor with a backplane placed at z = -2 mm was derived. The electrode geometry, sensitivity distributions and SVP are shown in Fig. 2.16 (g). It can be seen that the use of backplane distorts the sensitivity distribution by pushing it to the other side. It also causes negative sensitivity between the electrodes and the back-plane, reduces penetration depth and makes the overall distribution less uniform.

2.1.6 Influence of buried conductor in dielectric MUT on capacitance measurement

It is well known that a capacitance sensor is affected by conductivity (Huang *et al.* 1988 1). The influence of the conductor buried in a dielectric MUT on the performance of a planar capacitive sensor has not been studied so far. Simulations were carried out using the concentric ring capacitance sensors in different sensing modes. Capacitance measurements are calculated for a conductor (ε_r = 1, σ = 1) buried in a dielectric MUT (ε_r = 5, σ = 0) at varying depth (0.5, 1, 2, 3, 4 mm), and then normalised against

capacitance measurements without the conductor. Fig. 2.17 shows the sensor models, the field and potential distributions and the normalised capacitance values.

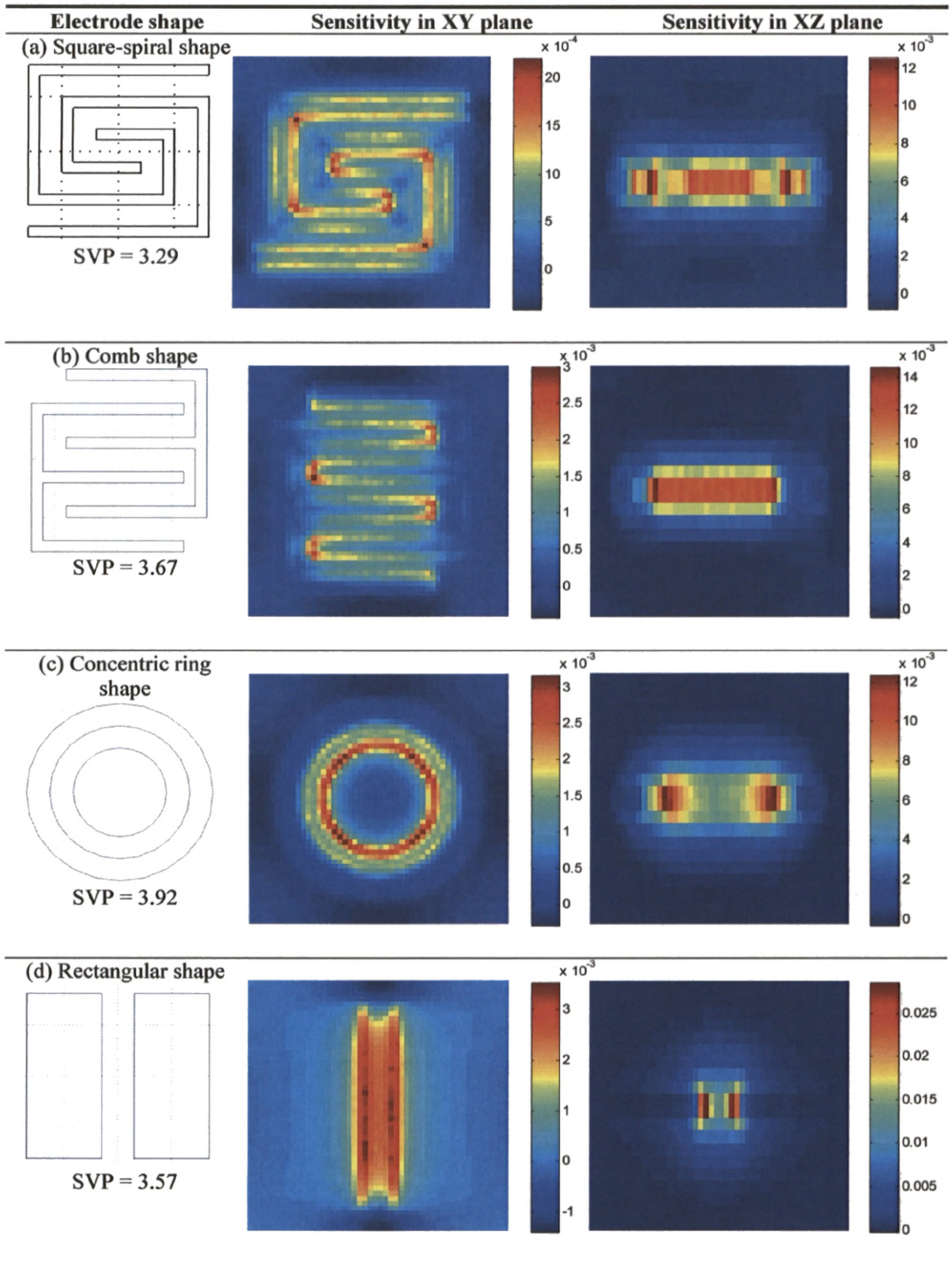

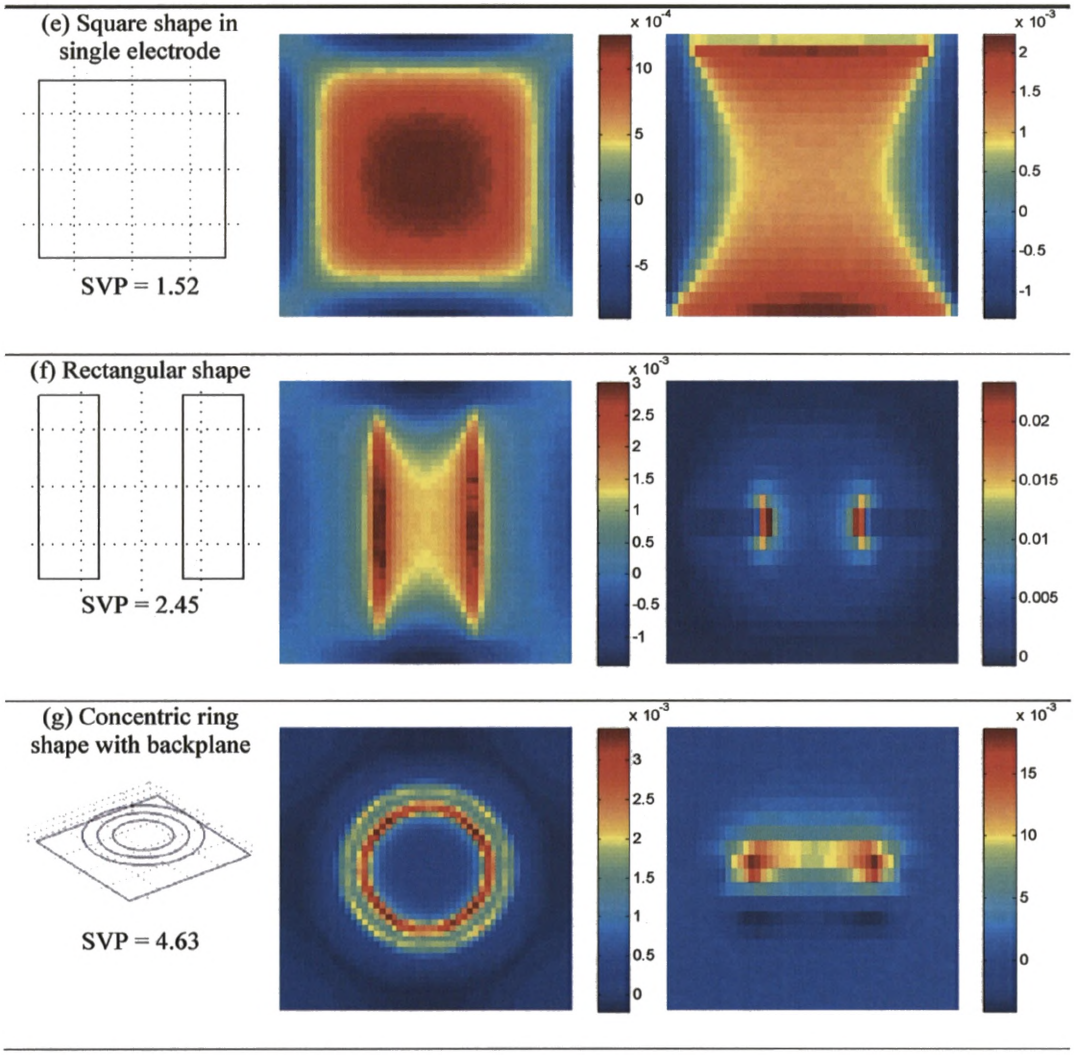

Fig. 2.16 Sensitivity distributions for electrodes with different shapes

It can be seen that the existence of the buried conductor causes a positive change in capacitance in the transmission and single-electrode mode. However, the capacitance decreases non-linearly with the buried depth. In the shunt mode, the buried conductor causes a negative change in capacitance. However the capacitance increases almost linearly with the buried depth.

The output from a planar capacitive sensor is a non-linear function of permittivity, conductivity and their distributions. With only capacitance measurement, it is difficult to distinguish the contributions of conductivity and permittivity if they both exist. To deal with this problem, an additional sensing modality can be introduced into the

sensing system. For example, a dual-modality capacitive and magnetic sensor may be used to provide complementary measurements about the MUT.

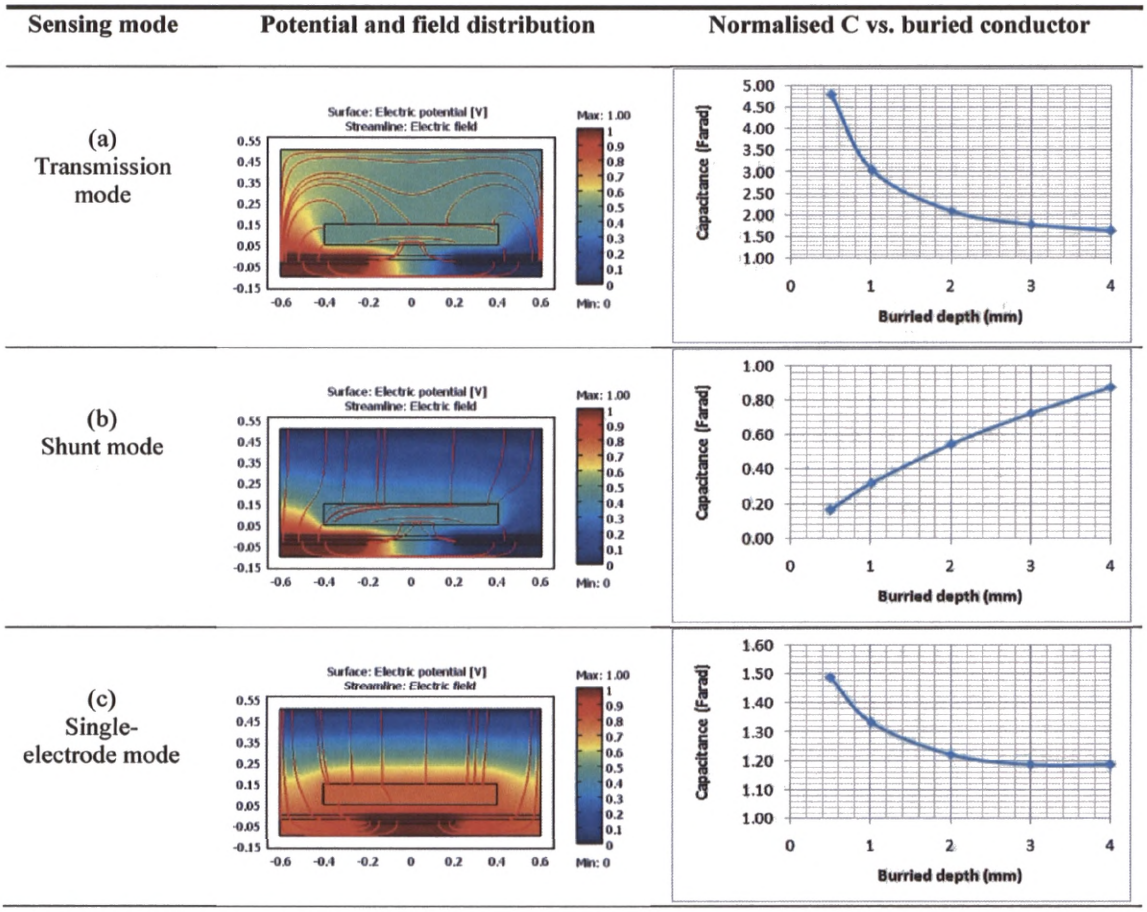

Fig. 2.17 Influence of conductor in dielectric MUT in different sensing modes

2.1.7 Applications

As a sensor output can be related to a number of system variables, a planar capacitive sensor can be used in a wide range of applications, which can be categorised into non-imaging and imaging applications. For non-imaging applications, one or several system variables can be estimated based on the relationship between the sensor output and the system variable(s). For imaging applications, the estimated variables are presented as an image, which can be obtained from capacitance measurements by different

reconstruction methods, such as direct imaging, interpolation, model-based imaging and tomography. Different imaging methods will be further discussed in Chapter 4.

In this thesis, imaging with planar capacitive sensor arrays will be further exploited for security applications. In particular, imaging with different sensing modes and reconstruction methods will be investigated.

2.2 Planar coil sensors

2.2.1 Choice of sensor

Imaging conductivity/permeability distributions by magnetic sensor(s) is of interest in a number of applications, including non-destructive testing (NDT) (Cawley 2001), process monitoring (Peyton *et al.* 1996) and security screening (Bruschini 2000). The available magnetic sensors include SQUID, fiber-optic, search coil, flux-gate, AMR, Hall-effect sensor and GMR sensor (Ganzalez-Nakazawa 2007, Tumanski 2007). Among them, the search coil has the widest measurement range and can achieve very high measurement resolution (Tumanski 2007). Table 1 lists the typical detectable field ranges of those magnetic sensors. In addition, the coil sensor has the advantage of versatility in design. It can be optimised by adjusting the arrangement of coil, size, number of turns and the driving signal. Therefore, it is chosen to be used in this thesis.

Table 2.1 Typical field range of various magnetic field sensors

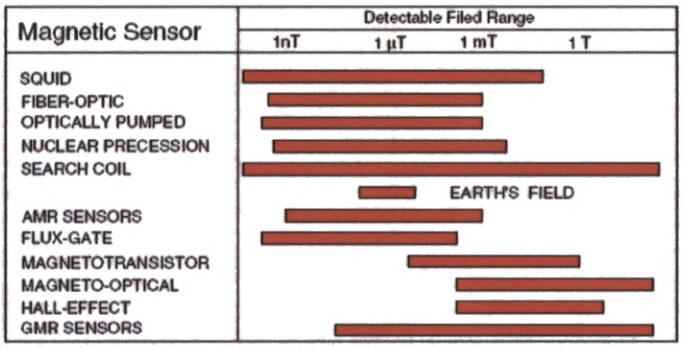

2.2.2 Eddy-current principle and methods for measuring induction phenomena

The sensing principle of search coil is based on measuring an eddy current. A driving coil generates a primary field and induces eddy current in an MUT. This eddy current generates a perturbation field and causes changes in voltage inside a coil, which are measured to reflect the properties of the MUT. A good introduction to eddy current principle and testing is available online from (NDT Resource Centre 2009). Based on the eddy-current principle, the use of a coil sensor can be in the form of a single coil as both transmitter and receiver, or separate driving-pickup coils. The latter has advantages of high sensitivity and flexibility in design, and thus, is used more often in applications related to material characterisation.

There are several induction phenomena that can be measured by coil sensors. The most direct form of induction is the induced voltage, V'. The induced voltage from an air-cored pickup solenoid under a time varying magnetic field can be expressed as (Tumanski 2007)

$$V' = -n\frac{d\Phi}{dt} = -nA\frac{dB}{dt} = -\mu_0 nA\frac{dH}{dt} \tag{2.9}$$

where μ_0 is the permeability of vacuum, n is the number of turns, A is the coil area, Φ is magnetic flux passing through the coil, B is the magnetic density and H is the magnetic field.

It can be seen that the sensitivity of the induced voltage to the changes in magnetic field is proportional to the coil area, the number of turns and the frequency of the field. To further enhance the coil sensitivity, a ferrite core may be used with a solenoid. In such a case, the induced voltage can be expressed as (Tumanski 2007)

$$V' = -\mu_0\mu_r nA\frac{dH}{dt} \tag{2.10}$$

where μ_r is the relative permeability of the ferrite core. Despite the increased sensitivity, the ferrite core reduces the measurement resolution and introduces non-linearity to the voltage output, which depends on temperature, frequency, flux density, and thus is difficult to compensate (Tumanski 2007).

Other induction parameters include the coil self-impedance (Z), the resonance factor (Q), or the mutual-impedance (M_{12}) between a pair of driving-pickup coils. The analytical solutions for the relationships between the induced parameters (V', Q, Z or M_{12}) and the variables of interest in the system (σ, μ and their distributions) are often complicated and application-dependent. For example, Dodd and Dedds (1968) presented the solutions for the induced voltage, self-impedance and mutual inductance of a pair of coaxially placed coils above a conducting plate.

On the other hand, the induced parameters can be measured and expressed by electrical signals, so that the relationships between the measured electrical signals and the system variables can be established. Based on the induction parameters, several methods can be used for taking measurement with coil sensors, including measuring the coil self-impedance, the resonance factor, the induced voltage from the pickup coil and the mutual inductance between the driving-pickup coils. These methods and their implementations will be further discussed in Chapter 4.

The design considerations for induction coil sensors include coil area, length in the z direction, number of turns and driving signal. These parameters affect sensor performance in terms of the generation of primary field as well as the detection of perturbation field. Different kinds of coil sensors and their designs are summarised in the latest review by Tumanski (2007).

2.2.3 Planar coil sensors and applications

In recent years, there is a growing interest in planar coil sensors, including analytical modelling of various designs of planar coil sensors, and different applications. However, there is a lack of review for planar coil sensors in literature. Therefore, a

review of the designs, features and applications of planar coil sensors are carried out in this section.

The planar coil sensor is a type of flat solenoid with a minimum length in the z direction. The advantages of planar coil sensors include high sensitivity due to small lift-off, flexible attachment to complex surfaces and ease of fabrication (Ditchburn *et al.* 2005). It can be a compact sensor if required. As the art work for a planar coil can be done by drawing in the design document instead of manual winding, coils of different shapes can be easily implemented. The commonly used shapes for planar coils include meandering winding, circular spiral and rectangular / square spiral.

Sensor modelling and analytical solutions to coil self / mutual impedance of various shapes have been extensively studied.

The models of the meandering winding magnetometers of single sensing element and sensor array have been established by Goldfine (2000), focusing on the analytical solutions of trans-impedance to MUT lift-off and electrical properties, which are subsequently used to generate measurement grids/look-up tables for parameter estimation and imaging (Schliker 2006).

The closed-form expressions for the self-impedance of planar circular spiral coil (Ditchburn *et al.* 2003) and the mutual-inductance of driving-pickup pairs of planar spiral coil (Burke and Ibrahim 2004, Burke and Ditchbum 2008) have been derived, presenting the response in impedance to different cases, such as free space, a conducting half space and an ideal crack. These studies demonstrated that different designs of planar coils can all be used in crack detection with good sensitivity. The closed-form expression for planar rectangular spiral coil has also been studied (Ditchbum and Burke 2005), showing that the response of a planar rectangular coil sensor to crack depends on its orientation. In addition, the advantages of the rectangular spiral shape over the circular spiral shape are the improved packing when used in array, less sensitivity to edge effects and simpler artwork. The impedance diagrams of the planar rectangular spiral coils are calculated by (Fava and Ruch 2006), suggesting that there is an optimal lift-off and frequency for different coil designs and applications. Tospelas and

Siakavella (2007) studied the performance of circular and square shaped coils in planar and non-planar forms, and further illustrated that planar coils give better results in crack detection when MUT lift-off is small.

Planar coil sensors with different designs and manufacturing processes have been used in a number of applications.

Planar meandering winding magnetometers have been used in applications in structure quality inspection (Fisher *et al.* 2000, Goldfine *et al.* 2001) and imaging of absolute electrical properties (Schliker 2006). This type of sensor can shape the EM field and has a penetration depth equal to coil pitch (Schliker 2006). Yamada (1995) used a planar probe consisting of a meander type driving coil and a mesh type pickup coil for crack detection in metals. It showed that the new probe has larger signal than conventional eddy current solenoid probes. To overcome the problems of edge effect and alignment, Mukhopadhyay (2002) presented a driving pickup pair with planar mesh type coil, and showed that an optimal coil pitch should be sought for a particular sensor. This type of sensor has been used for characterising the sample quality in the meat industry (Mukhopadhyay *et al.* 2005).

Hirota (1993) presented a micro-coil sensor for measuring magnetic field leakage in steel quality inspection. The sensor consists of two parallel coils placed in a co-planar plane, manufactured by photolithography technology. It showed that the planar sensor has a higher sensitivity and a better spatial resolution than the build-up type solenoid. (Uesaka *et al.* 1995, 1998) presented a micro eddy current sensor, consisting of a pancake type driving coil and an array (4 × 4) of planar spiral pickup coils (40 turns each) made on a flexible polyimide film by photolithography. This sensor is used for flaw detection for a conductive tube in nuclear plant. Sadler and Ahn (2001) presented an integrated on-chip eddy current sensor, consisting of driving-pickup pair of 13-turn square spiral coils with a Ni/Fe permalloy magnetic core, fabricated by MEMS technology, which is used for proximity and crack detection. Gatzen (2002) presented a microsensor based on thin-film technology for proximity detection, which consists of a big single turn driving coil and a 7-turn pickup coil with a soft magnetic core.

The design and modelling of planar coil sensors have been carried out extensively, but their applications are mainly focused on flaw/crack detection and material characterisation based on parameter estimation directly from measurements. To provide a visual interpretation of the system variables, imaging with planar coil sensor is to be further exploited. When the imaging space is large, a sensor array is favourable over a single sensing element, because mechanical movement of the sensor can be minimised or avoided.

In this thesis, imaging with a planar coil sensor array to detect hidden metallic objects will be investigated. The limitation of coil sensor is that it is insensitivity to permittivity. As capacitive and coil sensors can provide complementary information about the electrical properties of an MUT, a dual-modality sensor consisting of capacitive and coil sensor arrays is of strong interest and will be investigated.

2.3 Summary

This chapter reviews the sensing principle, design issues and applications for planar capacitive and coil sensors.

For planar capacitive sensors, a systematic study of sensor modelling, features and design issues is carried out in the context of characterisation and imaging of a dielectric MUT. According to the potential boundary conditions of an MUT, a planar capacitance sensor can be described using one of the three different sensing modes: (1) the transmission mode, (2) the shunt mode and (3) the single-electrode mode. The sensor response to the properties and positions of an MUT has been explained in detail. To achieve an optimal design, a trade-off between different evaluation parameters has to be made. In the transmission mode and the single-electrode mode, the response of the sensor is strongly related to the properties of an MUT, which makes the sensor suitable for material characterisation and imaging. In the shunt mode, the response of the sensor is strongly relevant to the positions of an MUT, and thus, the sensor is suitable for proximity/displacement measurement. In addition, the influencing factors on sensitivity distribution, and the effect of conductivity on sensor performance have been discussed for planar capacitive sensors. The sensitivity distribution of the sensor depends largely

on the geometry of the electrodes. In addition, conductivity would cause positive changes for a sensor in the transmission and single-electrode modes, but negative changes for the sensor in the shunt mode.

For planar coil sensors, the sensing principle, design issues and measurement methods have been briefly discussed. In particular, a further review of sensor modelling and application of planar coil sensors has been carried out.

As identified from the reviews, imaging with planar capacitive and coil sensor arrays using different sensing modes and image reconstruction methods will be investigated in this thesis. Due to the limitation in single modality sensing, the use of a dual-modality capacitive and coil sensor array is of particular interest.

Chapter 3 Design of planar capacitive and magnetic sensor arrays

In Chapter 2, imaging using different capacitive and coil sensor arrays with different image reconstruction methods has been identified for this research. This chapter presents the design of single-modality and dual-modality sensor arrays. The single-modality sensor arrays include a concentric-ring based array, a square-electrode based adaptive array and a square-electrode based single-electrode array for imaging permittivity, and a PCB-coil array for imaging conductivity/permeability. The dual-modality sensor array is based on the ring array and the PCB-coil array for imaging permittivity/ conductivity/permeability. The performance of the sensor arrays are evaluated experimentally in terms of dynamic range, sensing depth and cross-talk.

3.1 Penetration depth and size of sensing element

As the aim of the research is to generate images that can "see" through shoes, envelopes and small parcels, the desired penetration depth for the sensor arrays is first considered. The most likely place to hide threat objects in a shoe is in its bottom layer. Amongst different types of shoes, leather shoes and trainers are the most common, because they have a relatively thick and uniform bottom layer, which is about 1 to 2 cm thick. Most envelopes and small parcels have a thickness less than 2 cm. Therefore, the desired penetration depth is about 1 to 2 cm.

A spatial resolution in the order of 1 cm is desirable for sensor arrays to be able to identify the shape features of a hidden object. To compromise between the penetration depth and spatial resolution, the size of the sensing element for all the sensor arrays to be designed is chosen to be 2×2 cm^2.

3.2 Design of planar capacitive sensor arrays

Three types of capacitive sensor arrays will be investigated for imaging permittivity, including a concentric ring array, which works either in the transmission mode or the shunt mode; an adaptive array and a single-electrode array both based on square electrodes. An optimal design of each of the sensor array will be carried out.

3.2.1 Capacitance sensor array based on concentric ring element

The concentric ring sensor was used by Chen (1998) as a proximity sensor to measure the displacement of a grounded conductor. Li (2004) used the ring sensor for estimating the moisture content in cookies. Due to the simplicity and symmetry in structure, the ring element was used in a sensor array in an imaging application (Frounchi *et al.* 2003). Cheng (2008) also used a ring sensor array for security imaging. In the imaging applications, the ring sensor array was assumed to work in the transmission mode. When scanning shoes without removing them from the feet, it is more appropriate to use the shunt mode to model the sensor performance, because human feet are in a low potential. With the given elementary size, an optimal design for the ring sensor array will be sought.

A. Optimal design of ring sensor array

The optimal design for the concentric ring sensing element is a trade-off between the dynamic range and SVP of the sensor, which are determined by the combination of radii, ring width and separation of electrodes. To find out the optimal ratio between them, simulations have been carried out to compare the dynamic range and SVP of the sensor against varying design parameters in the transmission mode. A radius of 3, 4 and 5 mm for the centre electrode and a width of 1, 2 and 3 mm for the ring electrode are used in evaluation. To make full use of the sensing area, the separation between the adjacent sensing elements is chosen to be 2 mm, and the separation between the driving and sensing electrodes is chosen to be as large as possible. As the spacing of the sensing element is fixed, the penetration depth of the ring sensor is almost fixed. The dynamic range is given as the difference between the sensor output with a dielectric MUT ($\varepsilon_r = 5$,

σ = 0, thickness = 10 mm) and the output of an empty sensor. Table 3.1 gives comparison of the absolute dynamic range and SVP for different designs. The optimal design should have a big dynamic range and a least SVP in sensitivity distribution.

Table 3.1 Dynamic range and SVPs for different designs

Radii (mm)	3		4		5	
Width of Ring (mm)	Dynamic range (fF)	SVP	Dynamic range (fF)	SVP	Dynamic range (fF)	SVP
1	13.6	2.80	16.3	2.72	20.7	2.93
2	30.6	3.10	37.3	3.11	48.9	3.60
3	50.9	3.68	63.1	3.91	83.1	5.60

From the above results, it can be seen that the optimal set of parameters is: radii = 4 mm, width of ring= 2 mm. Therefore, the separation between the centre and the ring electrode is 3 mm and the separation between adjacent sensing elements is 2 mm. Compared with Cheng's design, in which the dynamic range is 26.5 fF and SVP is 3.25, the optimal design can increase the dynamic range by 41% and reduce the SVP by 4%. The ring sensor array can work in the transmission mode for scanning envelopes or small parcels, or work in the shunt mode for scanning shoes. From Chapter 2, the expected penetration depth for transmission mode is half of electrode spacing, which is about 4 mm. The expected penetration depth for the shunt mode is 1.5 times of electrode spacing, which is about 12 mm.

B. Sensor array

Ideally, a sensor array can be formed using any number of ring elements placed in rows and columns. The number of elements may depend on the size of the target MUT. In the current design, two arrays of 8×12 elements (equivalent to a sensing area of 16×24 cm^2) are used for scanning shoes while an array of 6×6 (equivalent to a sensing area of 12×12 cm^2) elements is used for scanning envelopee or small parcels. The driving electrodes in the sensor array are connected in rows while the sensing electrodes are connected in columns, so that a fast scan can be achieved by a row-excitation and column-detection method. Fig. 3.1 shows a 6×6 ring sensor array with connections. The ring sensor arrays

are made by PCB and a piece of rubber sheet (1 mm thick) is adhered to the surface of the electrodes as an insulation layer.

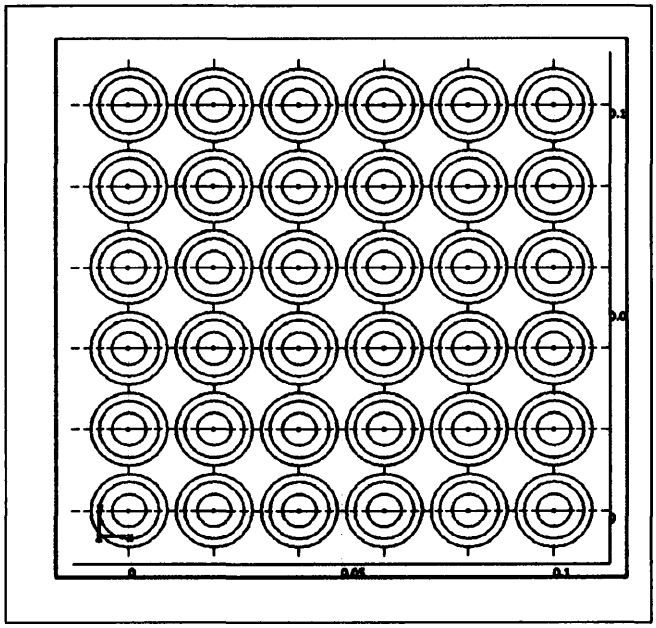

Fig. 3.1 Optimal design of ring array with 6×6 elements

C. Sensitivity distribution

3D modelling for the ring element has been carried out using COMSOL and a 3D electro-static generalised module with a sensing space of 20×20×20 mm^3. The 3D sensitivity distributions for the optimised sensing element in the transmission mode and shunt mode are calculated using equation 2.5. For calculating the sensitivity distribution in the transmission mode, all the outer boundaries of the sensing space are set to electric insulation. For calculating the sensitivity in the shunt mode, the top boundary of the sensing space is set to ground, and all other outer boundaries are set to electric insulation. The accumulated 2D sensitivity distributions are derived by summing up the 3D sensitivity values in the z direction within the sensing space. Fig. 3.2 shows the accumulated sensitivity distributions in the XY plane for the optimal design in the transmission mode and shunt mode. It can be seen that the high sensitivity values for the shunt mode are mainly around the edges of the electrodes and not as evenly distributed as for the transmission mode.

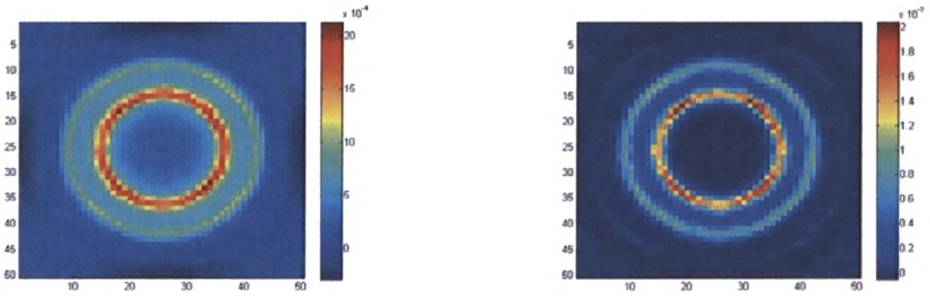

(a) Transmission mode (b) Shunt mode

Fig. 3.2 Sensitivity distributions in transmission and shunt mode

D. Cross-talk and sensing depth

Cross-talk of the ring sensor array was evaluated with the sensor in the transmission mode. The 6×6 sensor array was connected to a multi-channel imaging system developed in this research, which will be presented in Chapter 4. A test sample of the same size as the sensing element is placed at different positions relative to the same sensing element, including: (a) in the centre covering the whole element, (b) on the edge, covering two adjacent elements and (c) in the corner, covering four adjacent elements. Both dielectric and conductive samples have been used, which are a square piece of Blu-Tack and a square piece of copper sheet. Blu-Tack is a soft plastic compound, which can become adhesive when compressed, and can be easily made into different shapes. One category of the target threat objects is plastic explosives, such as C4. However, it is not possible to obtain C4 samples for this research because the distribution of C4 is highly restricted. Therefore, an alternative plastic, Blu-Tack, has been used in the experiments as a threat object. Fig. 3.3 shows the measurement matrix for samples placed at different positions relative to the same sensing element.

It can be seen that both dielectric and conductive materials give rise to changes in capacitance. The changes due to a conductive object are larger than from a dielectric object. Due to the structure of the ring sensor, where the excitation electrode is in the middle and the detection ring is surrounding the centre electrode, cross-talk is negligible after removing the noise from the measurements. The maximal influence from cross-talk is 5.3%, which is from Blu-Tack placed in the centre. However, the sample contributes to the measurement of every sensing element it covers, and the resulting

measurement decreases with the effective area covered in the sensing element. This means that an MUT may appear bigger in an image than its actual size, depending on the position of the edges of the MUT relative to the sensing elements.

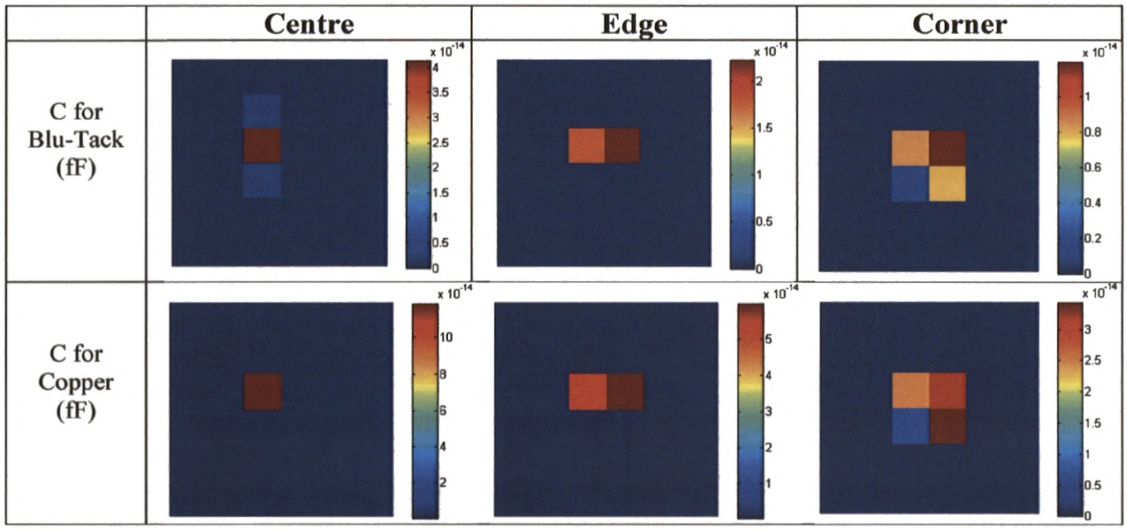

Fig. 3.3 Measurements from ring sensor array for samples placed at different positions relative to same sensing element

Sensing depth against life-off and thickness of MUT were examined for the ring sensor array in the transmission mode and the shunt mode. To make the ring sensor work in the shunt mode, a grounded top boundary needs to be used. To achieve this, a plastic cover (1 mm in thickness) adhered with grounded copper sheet (0.01 mm in thickness) adhered can be used. The ring sensor array works in the transmission mode without using this grounded plastic cover, but in the shunt mode when the grounded cover is placed above the sensor array with a certain height. This plastic cover is also used for single-electrode array, which will be explained later.

To examine the sensor response to life-off of MUT, a square piece of Blu-Tack was placed at different heights above the same sensing elements, and the changes in capacitance against the dynamic range are plotted in Fig 3.4 (a). To examine the sensor response to thickness of MUT, square pieces of Blu-Tack with the same thicknesses were stacked over the same sensing element, and the changes in capacitance against the dynamic range are plotted in Fig. 3.4 (b). The sensing depths for both cases are

identified using the system noise level. For the optimal ring sensor in the transmission mode, the sensing depth is about 6 mm with a dynamic range of 109 fF against lift-off of MUT, and about 3 mm with a dynamic range of 554 fF against thickness of MUT. For the ring sensor in the shunt mode, the sensing depth is about 11 mm with a dynamic range of 273 fF against lift-off of MUT, and about 14 mm with a dynamic range of 651 fF against thickness of MUT. The order of the sensing depths is in agreement with simulation from Chapter 2, but the dynamic range is much larger. This is due to the insulation layer used with the ring sensor.

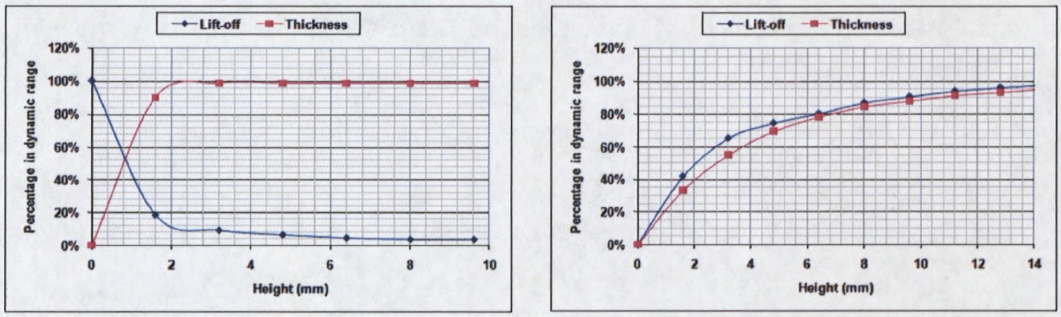

(a) Transmission mode (b) Shunt mode

Fig. 3.4 Sensing depth for ring sensor in transmission mode and shunt mode

3.2.2 Adaptive sensor array based on square electrodes

The square-electrode based sensor arrays of different electrode numbers and elementary sizes were used for 2D/3D tomographic imaging by Cheng (2008). A sensor array (4×4) consisting of big electrodes (electrode size: 40×40 mm^2, electrode separation: 5 mm) was used for landmine detection, a pair of parallel planar capacitance sensor arrays (16×16, electrode size: 15×15 mm^2, electrode separation: 1.5 mm) were used for scanning luggage, and an adaptive sensor array (16×16, electrode size: 11×11 mm^2, electrode separation: 1.5 mm) was used for scanning shoes. For the given elementary size in this thesis, an optimal design for the square-electrode based sensor array can be sought.

One feature of tomographic imaging with the planar sensor array is that different penetration depths can be achieved from different pair of excitation-detection electrodes, which enables 3D imaging using such an array. However, 3D tomographic

imaging using planar capacitive sensor array is difficult because the sensitivity decreases sharply in the z direction, and solving the inverse problem for such a case may require multi-level regularisation (Van Berkel and Lionheart 2007). Cheng (2008) revealed some 3D tomographic imaging results, showing that the reconstructed object in the image was significantly distorted. For security scanning, 2D imaging may be sufficient, and thus will be used in this thesis.

Another problem with tomographic imaging is the measurement protocol. Under the tomography method, measurements are taken from every independent electrode pair in the sensor array. For example, if the number of electrodes in the array is N, the number of independent measurements will be $N \times (N\text{-}1)/2$. This measurement protocol can be inefficient when N is large because:

(1) The required number of measurements increases proportionally to the power of N, which may significantly prolong the acquisition process;
(2) The size of sensitivity matrix also increases proportionally to the power of N, which may significantly increase the computation cost;
(3) The measurements from distant pairs of electrodes contain less useful information, as noise is dominant in such measurements.

Cheng (2008) suggested an adaptive measurement protocol, which is to generate small images from local scans and combine these local images to form a final image. In his method, the driving signal was applied to several electrodes at the same time while the measurements were taken from the individual electrodes surrounding the driving electrodes. However, this method is complicated in electrode switching, and may generate overlaps between different local scans, which are difficult to deal with. Therefore, no imaging results were reported.

A. Optimal design

In this work, 2D tomographic imaging by a square-electrode based sensor array will be investigated. The optimal design for the sensor array and an improved adaptive measurement protocol will be sought.

The optimal design can be found to compromise between the dynamic range and the sensitivity distribution for different pairs of electrodes. For the planar sensor array, the measurement from adjacent-electrode pair is more important other electrode pairs, as it contains more useful information. Therefore, the optimal design is sought based on the dynamic range and SVP of adjacent electrodes. With the given elementary area of 20×20 mm^2, different electrode side-lengths, 10, 12, 14, 16 and 18 mm, were evaluated, which corresponds to inter-electrode separation of 10, 8, 6, 4 and 2 mm. A 2×2 sensor array is modelled using COMSOL and a 3D electro-static generalised module. Fig. 3.5 shows the normalised dynamic range and 1/SVP against different ratios of separation/length. From the plots, an optimal ratio of 0.25 is found at the cross point of dynamic range and 1/SVP, which leads to a side-length of 16 mm and a separation of 4 mm.

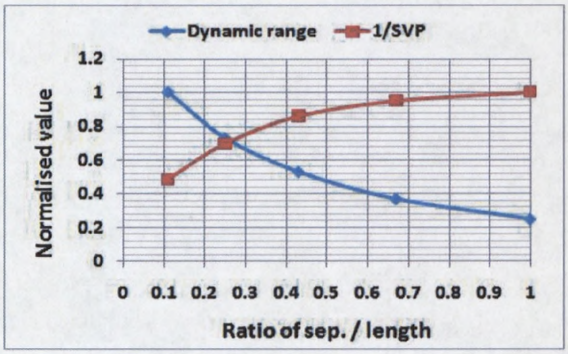

Fig. 3.5 Normalised dynamic range and 1/SVP against ratio of separation / length of electrode

B. Sensor array and adaptive scan

To improve the measurement protocol, an adaptive measurement method is proposed, which consists of coarse scan and fine scan. The coarse scan uses grouped electrodes as both excitation and detection, and can be used to quickly scan over the whole sensing space. The reconstructed image from coarse scan has a poor spatial resolution, but can be used to identify the region of interest. The fine scan uses normal electrodes to obtain local scan, and generates local images with a higher spatial resolution with no overlap.

For the un-identified regions, the corresponding local image will be zeroed. The final image is generated by combining all the local images. If the region of interest is small, a significant amount of time and computation can be saved by using the improved adaptive method.

To further explain the proposed scanning method, a 4×4 sensor array with the optimal electrode size is used as an example as shown in Fig. 3.6 The independent electrodes are numbered from E_1 to E_G. For the normal tomography method, measurements are taken from the independent pairs of electrodes, resulting in 120 independent measurements. For the coarse scan using a 2×2 sub-array, the sensor array is divided into 4 groups, $\{E_{1,2,5,6}, E_{3,4,7,8}, E_{9,A,D,E}, E_{B,C,F,G}\}$, resulting in 6 independent measurements. For a fine scan, measurements are taken from within each group, resulting in a maximal of 24 measurements if all groups are scanned. The total maximal number of required measurements will be 30, which is 4 times less than the number of measurements required from a normal tomography scan.

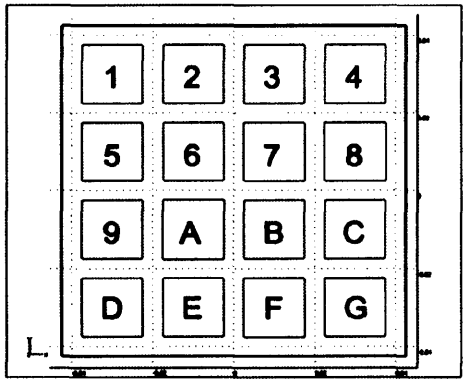

Tomography scan:
Independent electrodes:
$\{E_1, E_2, E_3, E_4, E_5, E_6, E_7, E_8, E_9, E_A, E_B, E_C, E_D, E_E, E_F, E_G\}$
Number of independent measurements: 120

Coarse scan:
Combined electrodes:
$\{E_{1,2,5,6}, E_{3,4,7,8}, E_{9,A,D,E}, E_{B,C,F,G}\}$,
Number of independent measurements: 6

Fine scan:
Groups of independent electrodes:
$\{E_1, E_2, E_5, E_6\}$, $\{E_3, E_4, E_7, E_8\}$,
$\{E_9, E_{10}, E_{13}, E_{14}\}$, $\{E_{11}, E_{12}, E_{15}, E_{16}\}$
Number of independent measurement in each group: 6

Fig. 3.6 Square-electrode based array and adaptive measurement protocol

This method can be used with sensor arrays of different numbers of electrodes. The scanning speed depends on the number of electrodes used in the coarse scan and fine scan. Table 3.2 gives the number of required measurements for different sensor arrays.

Table 3.2 Number of measurements required for different measurement protocols

Size of sensor array	Tomography	Coarse scan using 2 × 2 array	Coarse scan using 2 × 4 array	Coarse scan using array 4 × 4
Required measurement in fine scan	N/A	6	28	120
8 × 12	4560	276	120	15
8 × 8	2016	120	28	6
8 × 4	496	28	6	1
4 × 4	120	6	1	N/A

It can be seen that the fastest scanning speed can be achieved by using a quarter of the total number of electrodes for coarse scan. This suggests that when the number of electrodes is large, multiple levels of coarse and fine scans may be used to achieve a high scanning speed. For example, if an adaptive array consists of 8×8 electrodes, coarse scan using 4×4 electrodes can be used for the 1st level, and coarse scan using 2×2 electrodes can be used for the 2nd level. Fine scan with a group of 4 electrodes can be used to provide local scans.

C. Sensitivity distribution

A 4×4 sensor array is modelled by COMSOL using a 3D electro-static generalised module. The sensing space is 80×80×20 mm^3 and the outer boundaries of the sensing space are set to electric insulation. The 3D sensitivity distributions are calculated using equation 2.5 and the accumulated 2D sensitivity distribution are derived by summing up the sensitivity values in the z direction within the sensing space. Fig. 3.7 shows the typical 2D sensitivity distributions for adjacent and diagonal pairs of electrodes from both coarse scan and fine scan. For the coarse scan, the sensitivity distributions are derived from the electric potentials generated from the grouped electrodes. For the fine scan, the sensitivity distributions are derived from the electric potentials generated from the individual electrodes in a sub 2×2 array.

It can be seen that the sensitivity distributions for the fine scan has similar pattern as from the coarse scan. For the sensitivity distribution of the adjacent pairs, i.e. Fig 3.7 (a)

and (c), the higher sensitivity values are mainly distributed between the selected electrodes, which seem to be pushed towards the boundary of the sensing area. This is because the 2D distribution is accumulated from the 3D distribution, which has different distributions in the XY plane at different Z levels. At lower Z levels, the sensitivity in the XY plane is more uniform. At higher Z levels, the sensitivity in the XY plane is more concentrated between the excitation and detection electrodes, and is much less towards the centre of the sensing area. For the sensitivity distribution of the diagonal pairs, the higher sensitivity values are more distributed across the whole sensing area. In general, higher sensitivity values from the fine scan are spread out more evenly in the sensing area than from the coarse scan. This ensures that an image obtained by the fine scan has better accuracy and spatial resolution than from the coarse scan.

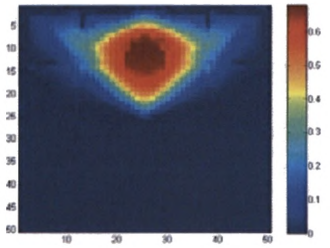

(a) Adjacent pair of $E_{1,2,5,6}$ and $E_{3,4,7,8}$

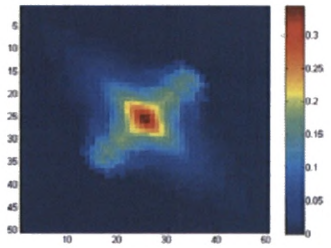

(b) Diagonal pair of $E_{1,2,5,6}$ and $E_{B,C,F,G}$

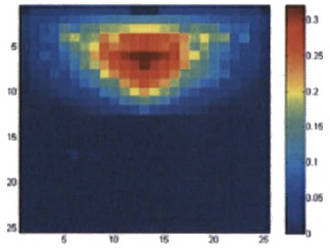

(c) Adjacent pair of E_1 and E_2

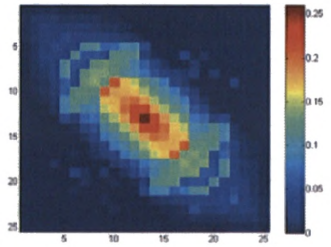

(d) Diagonal pair for E_1 and E_6

Fig. 3.7 Typical sensitivity distributions for coarse scan and fine scan

D. Equivalent cross-talk

A 4×4 single-electrode array has been made using PCB and a rubber sheet (1 mm thick) is adhered to the surface of the electrodes as the insulation layer. As oppose to the ring sensor array, the measurements from the adaptive array are all cross-element measurements. Similar experiments can be used to investigate the influence of the

position of the sample on imaging. The same square piece of Blu-Tack was placed at different positions relative to the same sensing element. Fig. 3.8 shows the final images obtained by normal tomography scan with a non-iterative algorithm, LBP, and an iterative algorithm, Landweber. The details about image reconstruction algorithms will be explained in Chapter 4.

It can be seen that the position of the sample affects the imaging results, but the influence is different from the ring sensor array. The sample appears bigger when placed in the centre or on the corner of a sensing element, and appears smaller on the edge. This is because the sample contributes to more pairs of adjacent-electrode measurements (8) when placed in the centre or on the corner (6), but contributes to less pairs of adjacent-electrode measurements (5) when placed on the edge. In addition, the reconstruction algorithm used also affects the imaging results, in that the size of the sample is smaller by the iterative algorithm than by the non-iterative algorithm.

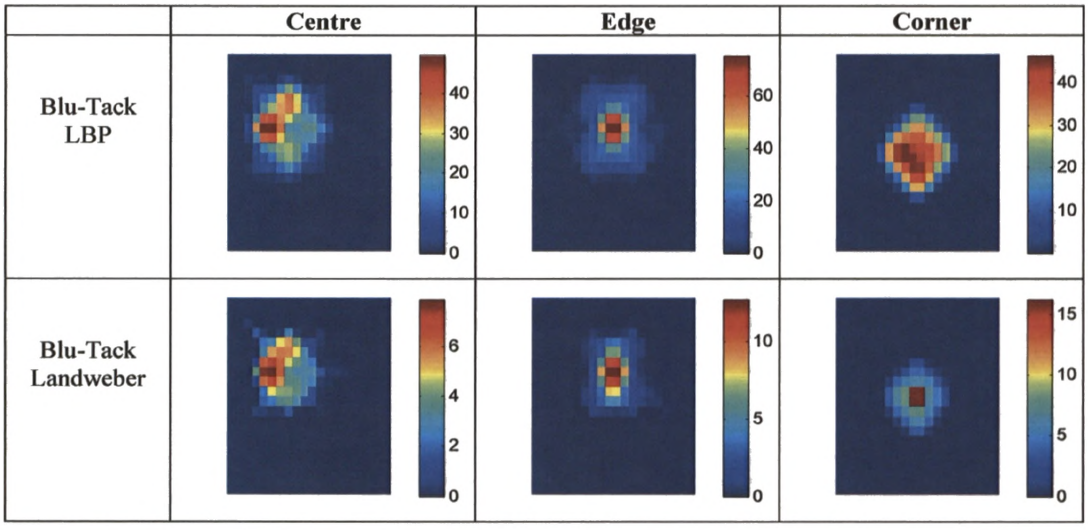

Fig. 3.8 Reconstructed images from adaptive sensor array for Blu-Tack placed at different positions

3.2.3 Single-square-electrode capacitance sensor array

Single-electrode capacitance sensor arrays were used for foot gauge (Sensatech 2000) and fingerprint imaging (Lee *et al.* 1999). Those capacitance arrays used a large number

of small electrodes in sub-cm scale, and every measurement corresponds to a pixel in an image. The resulting image has a higher resolution but the penetration depth of the sensor array is small. Given the size for the sensing element, the optimal design for the single-electrode sensor array is sought.

A. Optimal design

The optimal electrode size and separation can be found to compromise between the dynamic range and cross-talk. For the single-electrode sensor array, the effective sensing region for one electrode may extend further beyond its boundaries due to the fringe field effect. This effective region can be quantified as sensing width, which can then be used to evaluate cross-talk for a single-electrode sensor. In this thesis, the cross-talk for the single-electrode sensor is defined as the ratio between the sensing width and the spacing of electrodes

$$\text{Crosstalk} = \frac{\text{Sensing width}}{\text{Spacing of electrodes}} \tag{3.1}$$

The sensing width of the single-electrode sensor is first investigated. A single-electrode sensor is modelled by COMSOL using a 3D electro-static generalised module. The sensing space is 60×60×20 mm^3. The top boundary of the sensing space is set to ground and all the other outer boundaries set to electric insulation. The electrode has a varying side-length of 10, 12, 14, 16 and 18 mm, which corresponds to electrode separation of 10, 8, 6, 4 and 2 mm. A small dielectric MUT (10 × 10 × 10 mm^3, $\varepsilon_r = 5$, $\sigma = 0$) is moved along the X axes, and the normalised capacitance for different electrode sizes are plotted against the position of the MUT, as shown in Fig. 3.9. It can be seen that the normalised value at the boundary of the sensing element is well above 0. However, the effective sensing width can be determined using a threshold of 20% of the dynamic range (Da Silva 2008). Due to symmetry, the sensing width in the Y direction is assumed to be the same. The optimal single-electrode sensor should have a large dynamic range and a small cross-talk. Fig. 3.10 shows the normalised dynamic range and 1/cross-talk against the ratio of separation and length of electrodes. An optimal ratio

of 0.43 is found at the cross point, which leads to a side-length of 14 mm for the electrode and a separation of 6 mm.

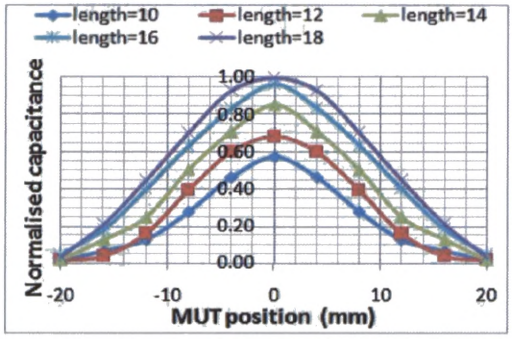

Fig. 3.9 Normalised capacitance against position of MUT

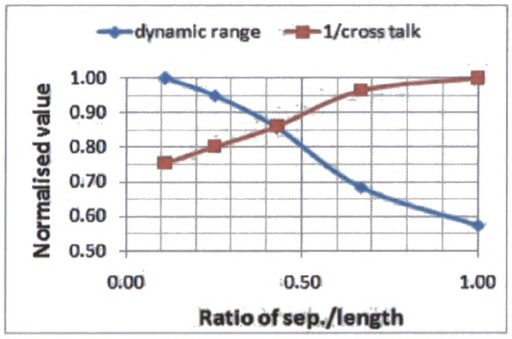

Fig. 3.10 Normlised dynamic range and 1/cross-talk against ratio of separation / length

B. Sensor array and measurement methods

A 4×4 single-electrode array has been manufactured using PCB and a rubber sheet (1 mm thick) is adhered to the surface of the electrodes as the insulation layer. In addition, the plastic cover with 2 copper sheets is used together with the sensor board. The bottom copper sheet is used as a big detection electrode, and the top copper sheet is used as grounded shield. The detailed connection to the imaging system will be introduced in Chapter 4. As the arrangement of the electrodes is the same as the square-electrode sensor array, both normal scan and adaptive scan can be implemented. The number of independent measurements for a normal scan is 16. The number of independent measurements for a coarse scan using groups of 2×2 electrodes and a fine scan within each group is 4. The total number of measurements for single-electrode sensor array is much smaller than the adaptive array.

C. Sensitivity distribution

The 3D sensitivity distribution between the sensor electrode and the virtual electrode is calculated using equation 2.5, and the accumulated 2D distribution is derived by summing up the sensitivity values in the z direction within the sensing space. Fig. 3.11 shows the 2D sensitivity distributions for one electrode used in the normal scan and fine

scan and 2×2 electrodes used in the coarse scan. Unlike the adaptive array, the sensitivity distributions for the coarse scan and fine scan have similar patterns and both evenly spread out across the XY plane.

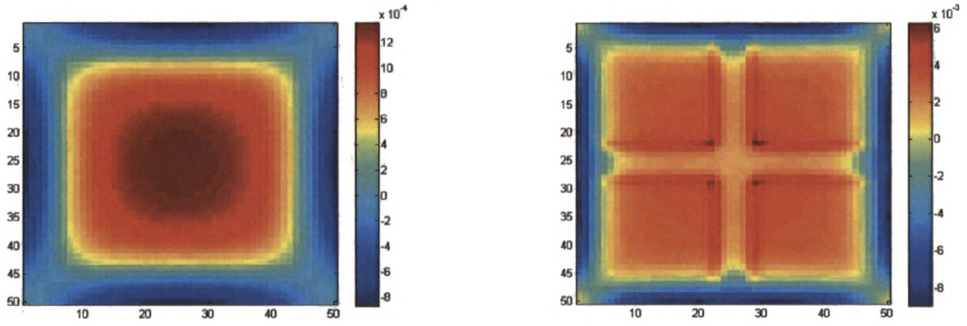

(a) One electrode (b) 2×2 electrodes

Fig. 3.11 Sensitivity distribution in XY plane for coarse scan and fine scan

D. Cross-talk and sensing depth

Cross-talk for the single-electrode sensor array was examined using the same square piece of Blu-Tack and copper sheet, which were placed individually at different positions relative to the same sensing element. Fig. 3.12 shows the measurement matrix in response to Blu-Tack or copper sheet after removing system noise.

It can be seen that both dielectric and conductive object give rise to positive changes in capacitance. The maximal cross-talk is 23.8% for copper placed on the edge. Cross-talk for the single-electrode array is generally greater than the ring sensor array. It has also been observed that the changes in capacitance is not necessarily bigger for conductive object, but more dependent on the overall contribution of the test sample to the parallel capacitor, including the thickness of the object and its material property. The MUT also contributes to the measurement of every sensing element it covers, and its contribution is proportional to the effective area covered in each sensing element. This feature is the same as the ring sensor array.

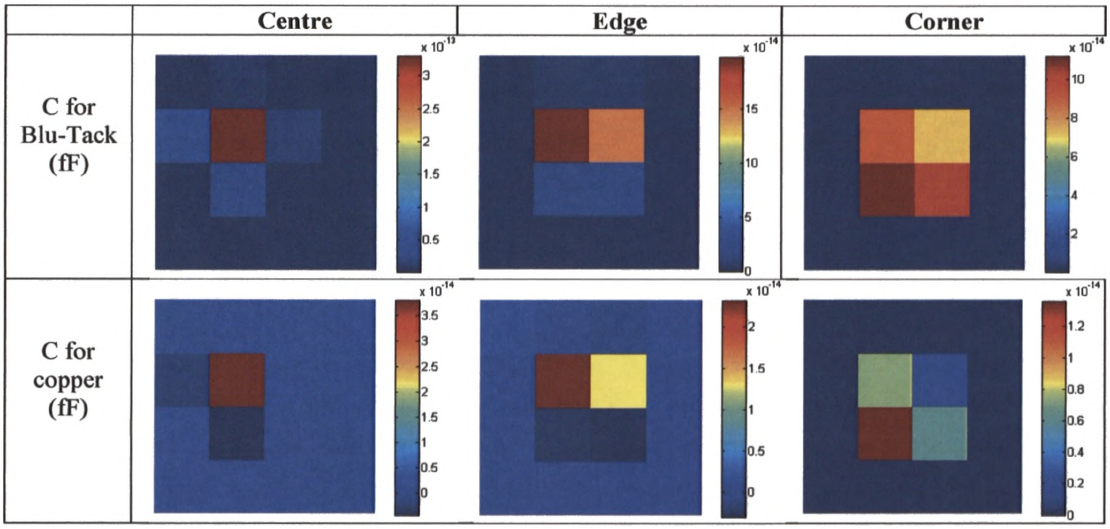

Fig. 3.12 Measurements from single-electrode sensor array for test sample placed at different positions

Sensing depths against lift-off and thickness of MUT for the single-electrode sensor were evaluated. To examine the sensor response to life-off of MUT, a square piece of Blu-Tack was placed at different heights above the same sensing elements. To examine sensor response to thickness of MUT, square pieces of Blu-Tack with the same thicknesses were stacked over the same sensing element. In both cases, the grounded virtual electrode is placed right above the test sample. The changes in capacitance against the dynamic range for lift-off and thickness of MUT are shown in Fig. 3.13.

Using the noise level of capacitance measurement, the sensing depth can be identified. For the single-electrode sensor, the sensing depth is about 10 mm with a dynamic range of 4.53 pF against lift-off of MUT, and about 12 mm with a dynamic range of 4.13 pF against thickness of MUT. The order of the sensing depths is in agreement with simulation given in Chapter 2, but the dynamic range is larger. This may be due to the insulation layer used with the ring sensor.

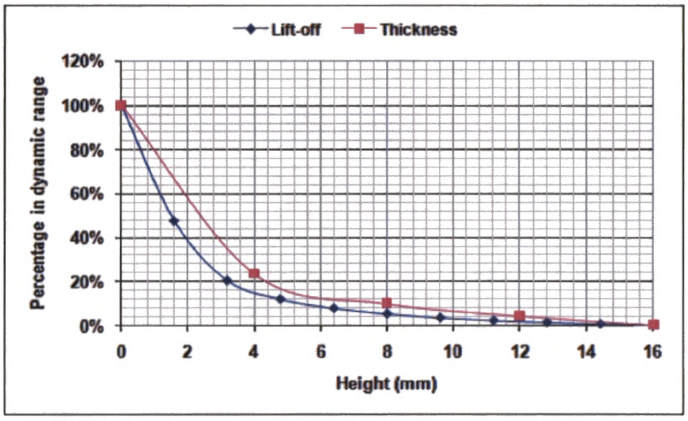

Fig. 3.13 Sensing depth against lift-off and thickness for capacitive sensor in single-electrode mode

3.3 Design of planar PCB-coil arrays

A. PCB coil sensor array

It is also of interest to investigate 2D imaging with planar PCB-coil array consisting of separate driver-pickup pairs. Burke and Ibrahim (2004) summarised the general arrangements for driving-pickup coils for measuring an MUT placed in a half space ($z < 0$), as shown in Fig. 3.14.

For the pancake coil configuration (Fig. 3.14 (a)), the primary field is isotropically penetrated into an MUT. The z component of the perturbation field is detected by the pickup coil. For the pancake-tangent configuration (Fig. 3.14 (b)), the primary field is isotropically penetrated into MUT, but the non-z component of the perturbation field is detected by the pickup coil, depending on the direction of pickup coil axes. For the tangent coil configuration (Fig. 3.14 (c)), the primary field is not isotropically penetrated into an MUT, and the non-z component of the perturbation field is detected by the pickup coil, both depending on the direction of their corresponding coil axes. The advantages of pancake coil configuration are:

(1) The sensor response is isotropic, because both the driving and pickup coils are normal to the MUT.

(2) When the lift-off of the driving coil is small, most of the primary field can penetrate into the MUT, and thus, maximises the perturbation field.

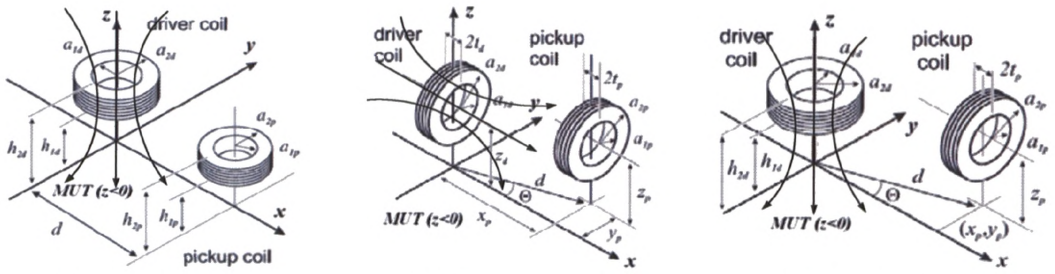

(a) Pancake coil configuration (b) Tangent coil configuration (c) Pancake-tangent configuration

Fig. 3.14 General arrangements for using coils to measure MUT in half space

Therefore, the pancake coil configuration is chosen in this work. To further increase the sensor response, the pickup coil is placed coaxially with the driving coil, where the perturbation field is strongest. In addition, a planar structure is used for both driving and pickup coils to minimise the coil lift-off and sensor size.

To maximise the effective coil area, the PCB-coil element takes a square spiral-shape, with an elementary area of 2×2 cm^2, 30 turns, a track width of 0.152 mm, a gap of 0.152 mm between tracks. Fig. 3.15 shows a planar PCB-coil element and part of a coil array board. The coil array board consists of 12×12 coil elements, with 12 coils in a row connected in series. The driving board is on the bottom while the pick-up board is right above it, with the coil elements in different boards superimposed in the z direction but orthogonal in connection. For a fast scan, the row-excitation and column-detection method is implemented, and the mutual inductance between the driving-pick pair in the form of $R + jX$ is simultaneously measured.

The square spiral PCB-coil elements and array were modelled using a 3D magneto-static module in COMSOL. The coils are approximated using 2D edges embedded into the 3D space. First, the magnetic field generated from serial connected driving coils of different number of elements (1, 3 and 5) were examined. Fig. 3.16 shows the

distributions of magnetic field lines and magnetic flux density in the XY and YZ planes. It can be seen that as the number of elements increases, the field distribution becomes more symmetric along the direction of the connection of coil elements. It can also be seen that there are some artefacts and discontinued field lines. These are due to the limited computing power of the PC used in this research, which significantly reduced the accuracy in solving the field equations. However, the accuracy can be improved by using a finer mesh and a solver with higher orders. The magnetic field will be used to generate the sensitivity distribution between the driving and pickup coils as will be explained shortly.

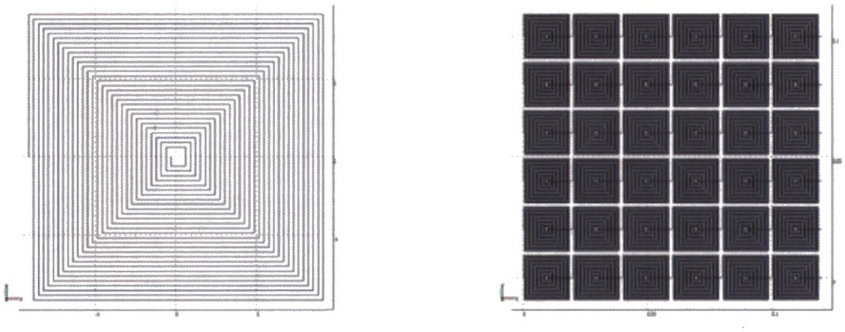

(a) Single PCB-coil element (b) Coil array and connection

Fig. 3.15 Planar PCB-coil element and array

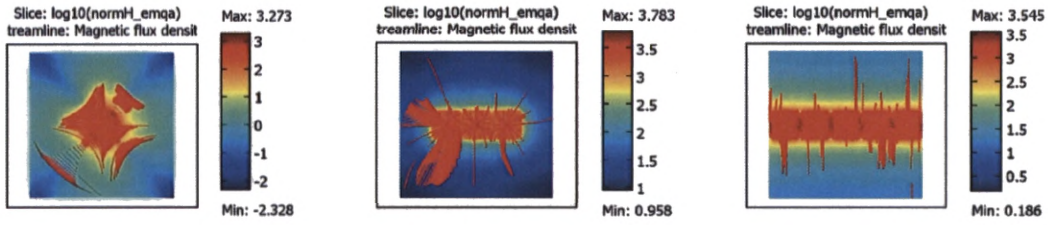

(a) 1 coil in XY plane (b) 3 coils in XY plane (c) 5 coils in XY plane

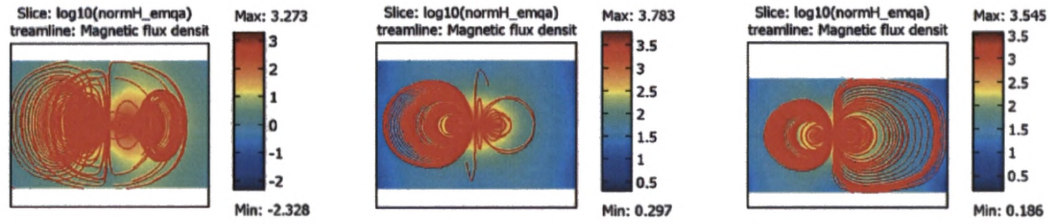

(d) 1 coil in YZ plane (e) 3 coil in YZ plane (f) 5 coil in YZ plane

Fig. 3.16 Distributions of magnetic field and flux density

B. Sensitivity distribution

To investigate the sensitivity distribution of the sensor array using the row-excitation and column-detection method, the typical sensitivity distribution of one driving-pickup pair in the coil sensor is obtained. The 3D sensitivity distribution can be calculated by dot-multiplying two magnetic fields generated by the driving and sensing coils respectively (Nakazawa-Gonzalez 2007)

$$S_j = -\int_V H_{d,j} \bullet H_{p,j} dv_j \tag{3.2}$$

where $H_{d,j}$ and $H_{p,j}$ are the values of magnetic fields in the j^{th} voxel when the driving and pickup coils are energised with a unit current, $v_j v_j$ is the volume of the j^{th} voxel and V is the sensing space. The accumulated 2D sensitivity distribution in the XY plane is obtained by summing up the 3D sensitivity in the z direction. Fig. 3.17 shows the 2D sensitivity distributions derived from driving-pickup pairs of 1-coil element, 3-coil element and 5-coil element.

It can be seen that the sensitivity distributions are mainly contained within the overlapping area between the driving-pickup pair, and the pattern of sensitivity distributions are the same for sensors with different number of coil elements. The main differences are in their values around the edges. This means that the sensitivity distribution of a pair of orthogonally placed multi-coils is comparable to that from a pair of 1-coil element, and thus, illustrates the viability of the row-excitation and column-detection method. Within the overlapped coil element, the sensitivity increases from the centre to the edge, because the spiral-structure of the coil makes the effective current density in the centre much less than near the edges. In addition, there are some negative sensitivity values surrounding the overlapped coil element, which can affect the measurements from neighbouring elements to some extent. Its influence will be discussed in section IV.

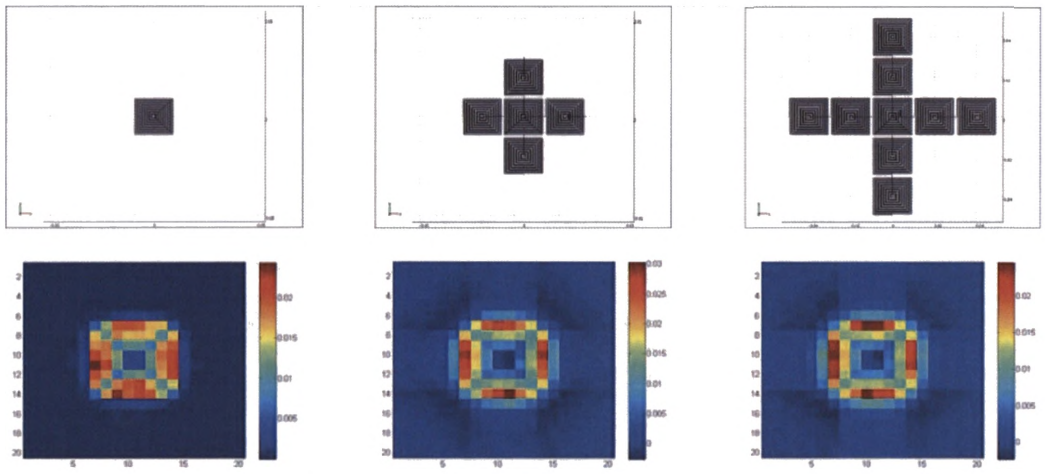

(a) Driving-pickup pair of 1-coil element

(b) Driving-pickup pair of 3-coil element

(c) Driving-pickup pair of 5-coil element

Fig. 3.17 distributions for row-excitation and column-detection

C. Frequency response

The frequency response of the multi-element coil sensor has also been evaluated in a frequency range from 1 kHz to 10 MHz (see Fig. 3.18) using the multi-channel multi-modality imaging system.

The resistance of the coil is constant (18.6 Ω) up to 100 kHz while the reactance of the coil is linearly increased with frequency up to 6 MHz. The resonant frequency of the coil is above 6 MHz. Therefore, up to 100 kHz, which is more than 10 times lower than the coil resonant frequency, the coil sensor can be used without considering the effect of parasitic capacitance. Fig. 18 (b) shows the mutual inductance between a pair of driving-pickup coils placed in an empty space up to 1 MHz. In this frequency range, the real part of the mutual inductance is almost constant, but changes dramatically above 100 kHz. The imaginary part of the mutual inductance is linearly increased with frequency up to 300 kHz. From both coil self-impedance and mutual inductance, it can be concluded that the working frequency for the PCB-coil array is below 100 kHz.

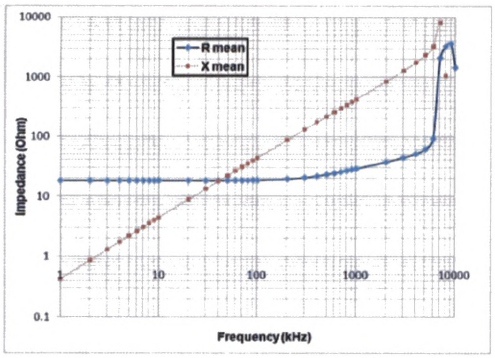

(a) Self-impedance of row coil

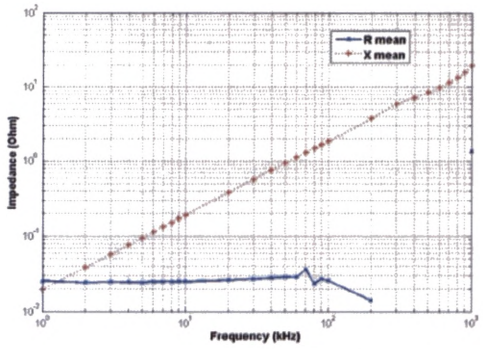

(b) Mutual impedance between coils

Fig. 3.18 Coil self- and mutual impedance

D. Cross-talk and sensing depth

Cross-talk and imaging depth for the coil sensor array were examined. A square piece of copper sheet (20×20 mm^2) was used as a test sample and placed at different positions relative to the same sensing element. Fig. 3.19 shows the measurement matrix for the above three cases after removing the system noise.

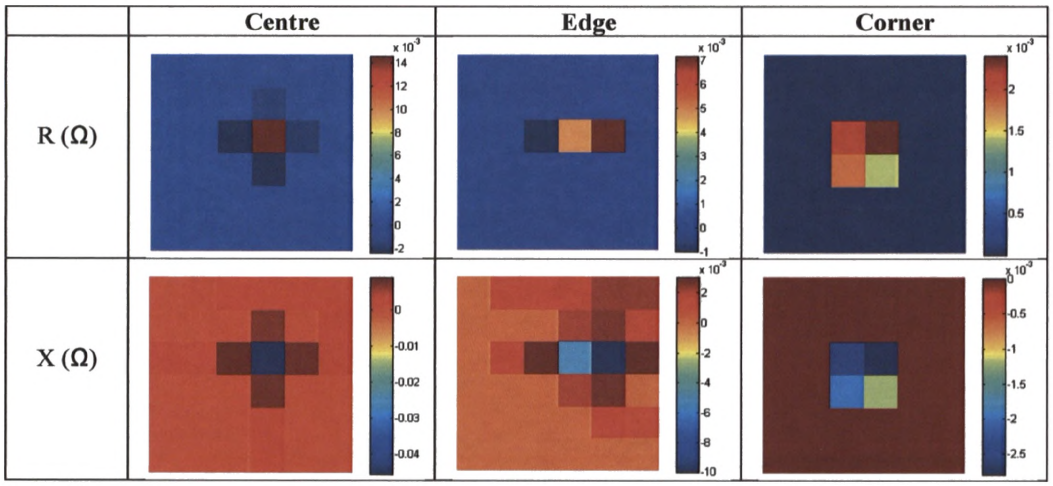

Fig. 3.19 Measurements for copper sheet placed in different positions on coil sensor array

It can be seen that cross-talk affects adjacent sensing elements by causing opposite changes for both R and X measurements. This is because the sensitivity values surrounding the overlapped element are negative, as illustrated in Fig. 3.17. The

influence of cross-talk on the adjacent elements is about -16% maximal for R and -30% maximal for X, when the sample is placed on the edge. The test sample also contributes to the measurement of every sensing element it covers, which may make the MUT appear bigger in an image.

To evaluate imaging depth for the coil sensor, the same square copper sheet was placed at different heights (0, 5 and 10 mm) away from the sensor. The percentages of those measurements against the dynamic range of the sensor are plotted against different heights, as shown in Fig. 3.20. The system noise was used as the threshold to determine the imaging depth, which is about 10 mm for both R and X.

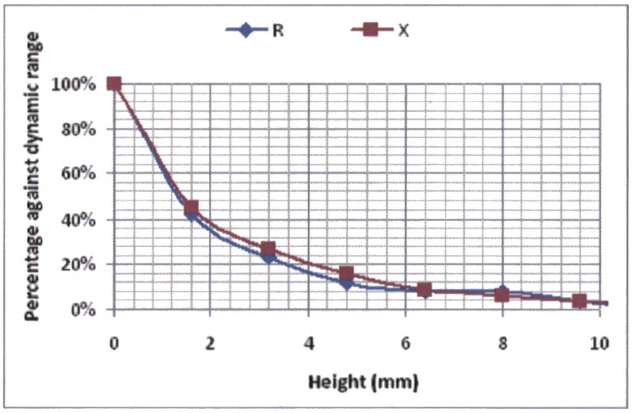

Fig. 3.20 Percentage of changes in measurement against lift-off

3.4 Assembly of dual-modality capacitive and coil sensor array

To provide complete information about the electrical properties of an MUT, a dual-modality capacitive and coil sensor array is assembled. Due to the similarity in array structure and measurement protocol, the ring based sensor array and the PCB-coil array are used to form a dual-modality array. The ring array is stacked on top of the coil array with the sensing elements superimposed in the z direction. A multi-channel multi-modality imaging system is used to acquire capacitance and mutual inductance measurements. The detailed interfacing and measuring method will be explained in Chapter 4. Due to the limited channels for the mutual induction configuration, only 6×6 sensing elements are used from both arrays.

The sensing depth for the dual-modality sensor array has been evaluated, and the changes in measurement against lift-off of MUT are plotted in Fig. 3.21. Using the noise level as threshold, the sensing depth is 3 mm for C, 5 mm for R and 8 mm for X. Due to the presence of an additional sensor board, sensing depths and dynamic ranges for the dual-modality sensor array are smaller than used individually.

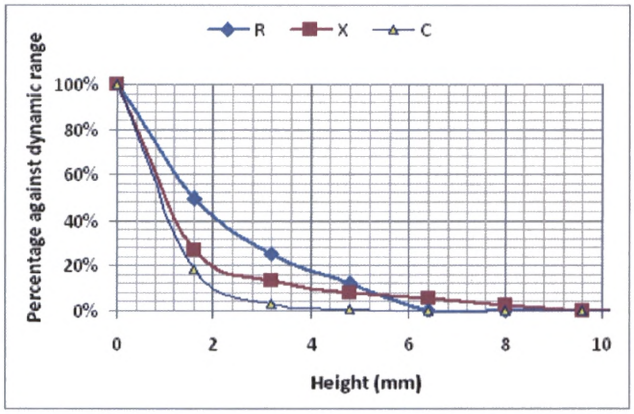

Fig. 3.21 Percentage of changes in measurement against lift-off for dual-modality sensor array

Cross-talk for the dual-modality sensor has also been evaluated. The influence of cross-talk on C, R and X measurements is similar to single modality sensor arrays.

3.5 Summary of designs of sensor arrays

This chapter presents the optimal designs and evaluations of the single-modality and dual-modality sensor arrays. To compromise between the penetration depth and spatial resolution, an elementary area of 2×2 cm^2 was chosen for all the sensor arrays.

A concentric-ring based array has been designed to work in the transmission mode and shunt mode. In the transmission mode, it can achieve a sensing depth of 6 mm against lift-off and 3 mm against thickness of MUT. In the shunt mode, it can achieve a sensing depth of 11 mm against lift-off and 14 mm against thickness of MUT. The square-electrode based array is designed for 2D tomography imaging. An improved adaptive

measurement protocol has been proposed, which can improve acquisition and imaging efficiency significantly when the number of electrodes in the sensor array is large. A single-electrode array has been designed also based on the square electrodes. It can achieve a sensing depth of 10 mm against lift-off and 12 mm against thickness of MUT. The order of the sensing depths for the capacitive sensor arrays in the transmission, shunt and single-electrodes modes is in agreement with simulations in Chapter 2.

A PCB-coil array has been designed consisting of separate driving-pick boards. It can achieve a sensing depth of 10 mm against life-off of MUT. A dual-modality sensor array has been assembled using the ring array and the PCB coil array. Due to the presence of additional sensor board, the dual-modality sensor array has a smaller dynamic range and shorter sensing depth for C, R and X measurements.

Cross-talk has different influences on different sensor arrays. For the ring array, single electrode array, PCB coil array and dual-modality array, a sample contributes to every sensing element it covers. This error is biggest when a sample is placed on the corner of a sensing element. For the adaptive array, the sample appears bigger when placed in the centre and on the corner, but smaller when placed on the edge.

Chapter 4 Imaging system, image reconstruction and fusion

This chapter presents the design of a multi-channel, multi-modality imaging system, as well as image reconstruction and fusion algorithms. To address the challenges of interfacing to various sensor arrays designed in Chapter 3, different methods of taking measurements with capacitive and coil sensors are reviewed. A multi-channel multi-modality imaging system based on an impedance analyser has been developed and evaluated. Image reconstruction and fusion are also reviewed, and suitable algorithms are developed.

4.1 Overview circuits and systems used with capacitive and coil sensors

In Chapter 2, different methods for taking measurements with capacitive and coil sensors have been discussed. It is desirable to develop an imaging system to acquire measurements from various planar sensor arrays designed in Chapter 3, especially from the dual-modality sensor array. To identify the most suitable solution, the circuits and the imaging systems used with capacitive and coil sensors will be reviewed at first.

4.1.1 Circuits and systems used with capacitive sensors

As discussed in chapter 2, the suitable circuits for taking measurements with capacitive sensors in the transmission mode and shunt mode include the charge/discharge circuit, the ac-based circuit and the auto-balancing bridge circuit, while the current injection-based circuits are suitable for capacitive sensors in the single-electrode mode. In recent years, there is a growing emergence of capacitance sensing ICs from different manufactures. These circuits and ICs and their applications will be briefly reviewed.

A. Charge/discharge circuit

The charge/discharge circuit is a popular capacitance measuring circuit based on the charge-transfer principle. It uses a set of 4 switches to repeatedly charge the unknown

capacitor, C_x, to a dc voltage, and discharge it to ground. The resulting charge/discharge currents flowing through the unknown capacitor in the two phases are fed to separate current-to-voltage (I-V) converters to produce voltage outputs proportional to C_x. The differential configuration of the circuit, which can eliminate the offset error from op-amps, is shown in Fig. 4.1 (a), and the switch control signals are shown in Fig. 4.1 (b). The voltage output from the differential amplifier is given as (Huang *et al.* 1992)

$$V_x = 2fV_c R_f C_x \tag{4.1}$$

where f is the operating frequency of the switches, V_c is the voltage input, R_f is the feedback resistor in the I-V converter, C_x is the unknown capacitance to be measured.

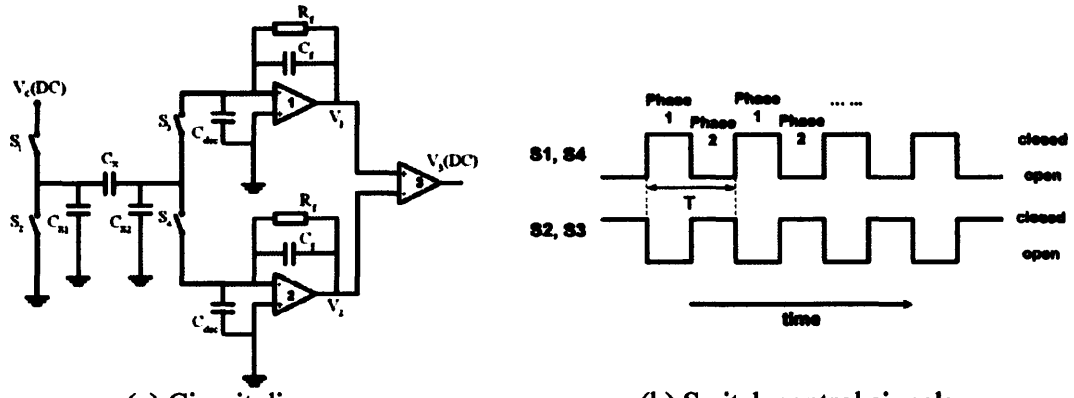

(a) Circuit diagram (b) Switch control signals

Fig. 4.1 Charge/discharge capacitance measuring circuit

The charge/discharge circuit is simple, low-cost and easy to be integrated into IC. It can achieve a resolution of 0.3 fF (Huang *et al.* 1992). However, the problems with this circuit include baseline drift, charge-injection from CMOS switches, and thus should be recalibrated frequently (Yang 1996 1). The switching frequency is limited by the speed of CMOS switches and is normally below 10 MHz. This circuit is primarily used for capacitance measurement, and its performance is affected by conductivity in the MUT (Huang 1988 1). The transient processes and steady-state response for the circuit can be found in (Hu *et al.* 2007). The charge/discharge circuit has been used in an ECT system (Huang *et al.* 1992) and a portable envelopee scanner (Cheng 2008).

B. AC-based circuit

The ac-based circuit uses a sine wave voltage as excitation and measures the ac current flowing through the unknown capacitor by an I-V converter with a capacitive dominant feedback. The resulting voltage output from the I-V converter is proportional to C_x, which is given as (Yang 2001)

$$V_x = -\frac{C_x}{C_f} V_i \tag{4.2}$$

where V_i is the input sine wave voltage, C_f is the feedback capacitor in the I-V converter. This voltage is then demodulated by a phase sensitive demodulation (PSD) to measure the capacitive component. The circuit diagram for the ac-based circuit is shown in Fig. 4.2. A detailed description of this circuit can be found in (Yang 2001). The transient processes and influence of noise on circuit performance can be found in (Gonzalez-Nakazawa *et al.* 2005).

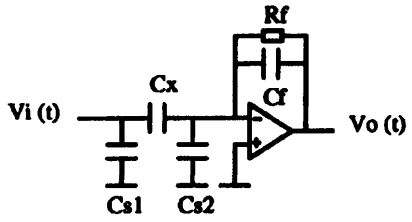

Fig. 4.2 Ac-based capacitance measuring circuit

Compared with the charge/discharge circuit, the ac-based circuit has low base-line drift and a 19 times smaller noise level (Yang 2001). The operating frequency is normally several hundred kHz, mainly limited by the bandwidth of the op-amp in the I-V converter. This circuit can also measure conductive component if the feedback in the I-V converter is chosen to be resistive dominant (Yang 2001). The ac-based circuit has been used in an ECT system (Yang and York 1999), a flow measuring system (Da Silva 2008) and a foot scanner with capacitive sensor array (Cheng 2008).

C. Auto-balancing-bridge-based circuit

The auto-balancing-bridge (ABB) circuit is a popular method for accurate impedance measurement in the low frequency range. The circuit consists of a signal source, a vector current meter based on an I-V converter and a vector voltage meter, as shown in Fig. 4.3 (Agilent Technologies 2000). The signal source provides a sine wave voltage with programmable frequency and magnitude, which is applied to the device under test (DUT) via the H_{cur} terminal. The resulting current flowing through the DUT, I_x, is measured by the vector current meter via the L_{cur} terminal. The voltage drop across the DUT, V_x, is measured by the vector voltage meter via H_{pot} and L_{pot} terminals. Detailed description of the ABB circuit can be found in (Agilent Technologies 2000). The ABB circuit measures $R + jX$ (R: resistance, X: reactance) by a series circuit mode and $G + jB$ (G: conductance, B: susceptance) by a parallel circuit mode. Other impedance parameters, such as inductance (L), capacitance (C), magnitude of impedance (Z) and phase angle (θ) can be calculated from these measurements. The complex impedance, Z, is expressed by

$$Z = \frac{V_x}{I_x} = R + jX = \frac{1}{G + jB} \tag{4.3}$$

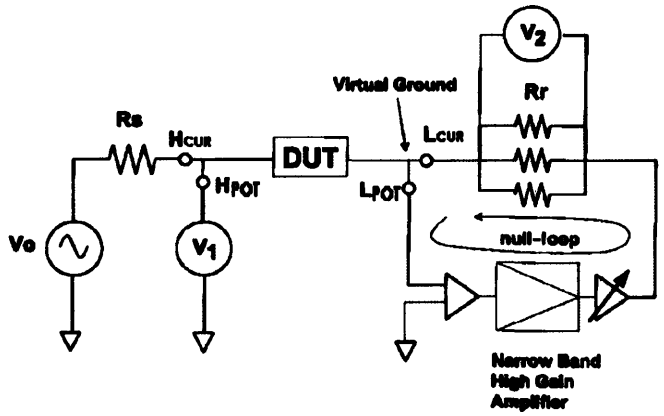

Fig. 4.3 Auto-balancing-bridge circuit for impedance measurement

The ABB circuit is widely used in impedance analysers. It uses several range resistors to achieve a high resolution over a wide measurement range. The problems with ABB

circuit are (Agilent Technologies 2006): (1) difficult to balance the bridge at high frequency or when the cable length is too long, (2) high noise at low-Z and high-Z ends and (3) unstable measurements when the range changes. Impedance analyser has been used to build multi-channel ECT systems (Chondronasios *et al.* 2001, Yang 2007).

D. Current injection-based circuit

The current injection-based circuit uses a current source to energise a grounded unknown capacitance, and measures the resulting voltage across it or the time for the voltage to reach a certain level. Figure 4.4 shows the current-injection voltage-detection method based on a modified enhanced Howland ac current source reported by Nerino (1997).

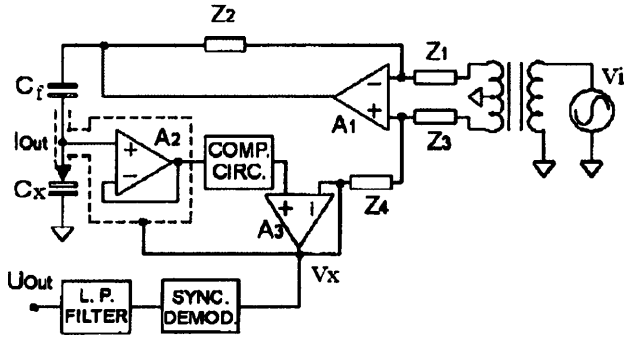

Fig. 4.4 Howland current source based capacitance measuring circuit

The Howland current source is a voltage-controlled current-source (VCCS) widely used in various applications with resistive load, such as in electrical impedance tomography (EIT) (Ross *et al.* 2003). A high-speed voltage buffer network is used together with the Howland current source to eliminate the stray capacitance by drive the active guard, and to provide a voltage input to a PSD. In an ideal case, the input voltage, V_x, is given by (Nerino *et al.* 1997)

$$V_x = -\frac{C_f}{C_x} V_i \tag{4.4}$$

where V_i is the input to the Howland current source and C_f is the range capacitor used to determine the magnitude of the output current.

Common problems with the Howland current source are component mismatch and the finite open-loop gain of the op-amp (Franco 2002), both of which can degrade the output impedance of the current source. As the capacitive load has much higher impedance than a resistive load, the requirement for component match and the bandwidth of the op-amp in this circuit is even higher. This current source based circuit has been used in capacitance based displacement measurement (Nerino *et al.* 1997).

E. Capacitance sensing ICs

In recent years, there is a growing emergence of capacitance sensing ICs, notably, the capacitance-to-digital converters (CDC) from Analog Devices, CapSense ICs from Cypress Semiconductor, the E-field sensing devices from Freescale Semiconductor and the Touch Control ICs from Quantum Research Group. Their working principles and features are reviewed here.

The CDC is based on a switched-capacitor sigma-delta (Σ–Δ) modulator. It has different implementations to support the measurement of floating capacitor (suitable for the transmission/shunt mode) and grounded capacitor (suitable for single-electrode mode). The conceptual diagram of the CDC is shown in Fig. 4.5 (O'Dowd *et al.* 2005). Instead of taking the variable voltage as input, the modified Σ–Δ modulator uses a fixed voltage as a reference and takes the unknown capacitor, C_x, as input. In such a way, simplicity and accuracy of Σ–Δ modulator can be maintained, and more importantly, capacitance can be directly transferred into a digital form. The detailed descriptions for the CDC ICs can be found in (O'Dowd *et al.* 2005). Analog Devices offers CDC ICs with different number of channels and resolutions. The CDCs also include on-chip offset-compensation, calibration engine, register control and serial communication (SPI or I^2C). Typical CDC ICs are AD7746 (24-bit, 2 channels, measuring floating capacitor) for industrial applications, AD7142 (16-bit, 14 channels, measuring floating capacitor) and AD7147 (16-bit, 13 channels, measuring grounded capacitor) for touch-control applications (Analog Devices 2009).

The CapSense ICs from Cypress Semiconductor are based on current-injection and time-measurement. It uses a fixed current source and an unknown capacitor to charge and discharge an external capacitor to different voltage levels. The rising time for the voltage ramp or the subsequent pulse width generated by the comparator is measured to calculate the value of C_x. The conceptual circuit diagram of the CapSense IC is shown in Fig. 4.6 (Marsh 2006). It is designed to be used with capacitive sensors in the single-electrode mode. The detailed descriptions for the CapSense ICs can be found in (Cypress Semiconductor 2007). The feature of the CapSense ICs is that the capacitance sensing module is included in a Programmable-System-on-Chip (PSoC) IC, which also contains many other peripherals (Cypress Semiconductor 2008). CapSense ICs are mainly targeted at touch control applications.

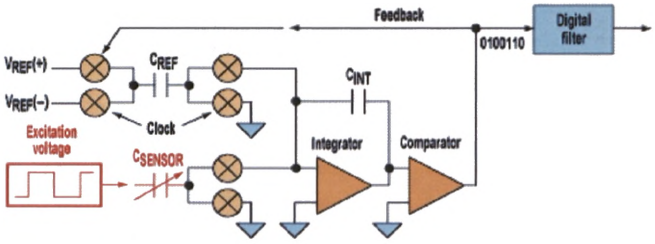

Fig. 4.5 Modified Σ–Δ modulator for capacitance-to-digital converter

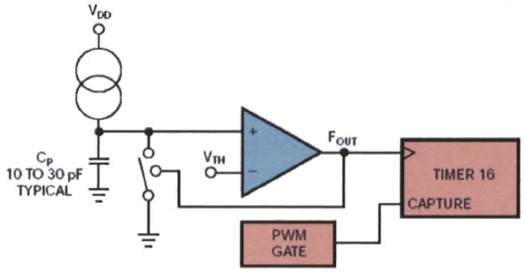

Fig. 4.6 Current injection based method for measuring grounded capacitor

The E-field sensing device from Freescale Semiconductor makes use of a sine wave voltage source as excitation. An electric field is generated between the active electrode and the "ground", which consists of not only a grounded DUT, but also the deselected electrodes. The conceptual circuit diagram of the E-field sensing device is shown in Fig.

4.7 (Freescale Semiconductor 2006 1) and the detailed descriptions of the IC can be found in (Freescale Semiconductor 2006 2). It is also designed to be used with capacitive sensors in the single-electrode mode. The E-field sensing ICs are targeted at both general industrial and touch control applications.

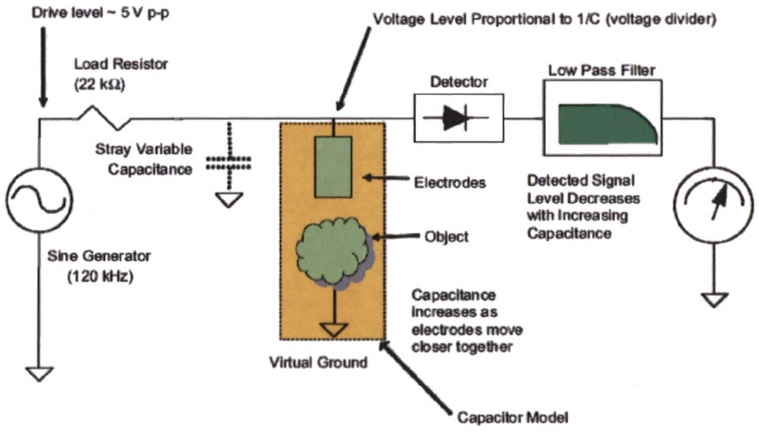

Fig. 4.7 Block diagram for E-field sensing from grounded capacitor

The Touch Control ICs from Quantum Research Group is based on the charge transfer principle, but uses randomised narrow-width pulses as excitation, which can reduce lowers power consumption and cross-sensor interference (Marsh 2006). Quantum Research Group provides ICs to support both the shunt mode (QMatrix) and the single-electrode mode (QTouch) as shown in Fig. 4.8 (Quantum Research Group 2009). They are mainly targeted at touch control applications.

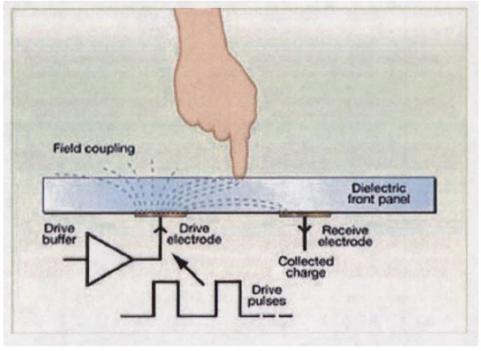

(a) QMatrix

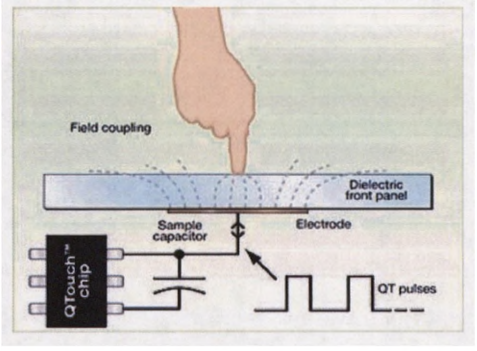

(b) QTouch

Fig. 4.8 Touch control ICs from Quantum Research Group

4.1.2 Circuits and systems used with coil sensors

As discussed in from Chapter 2, different methods to take measurement with coil sensors include measuring the self-impedance, the resonance factor, the induced voltage and the mutual inductance. The implementations for those methods and their applications will be briefly reviewed.

A. Self-impedance

Measuring the self-impedance is widely used with single coil sensors. Fig. 4.9 shows the conceptual circuit diagram for this method. An ac signal, either in the form of voltage or current, is applied to a single coil. Both the current flowing through the coil and the voltage across it are measured. The self-impedance of a coil can be expressed by

$$Z = \frac{V}{I} \tag{4.5}$$

where I is the current flowing through the coil and V is the voltage across the coil.

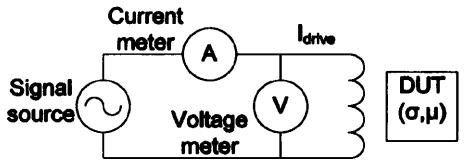

Fig. 4.9 Conceptual circuit diagram for measuring coil self-impedance

This method is the same as the ABB circuit, which is widely used in impedance analysers, such as HP4294A from Agilent (2008) or 1260A from Solartron Analytical (1996). This method has been used for lift-off measurement (Yin *et al.* 2004) with a single coil sensor.

B. Q-factor

Measuring the Q-factor is another method used with single coil sensors. Fig. 4.10 shows the conceptual circuit diagram for this method. The coil sensor is connected with a tuneable capacitor to form a LC oscillation circuit, which has a resonance frequency as given by

$$f = \frac{1}{2\pi\sqrt{LC}} \tag{4.6}$$

At resonance, $X_D = -X_C$, and the Q-factor is given by (Agilent 1998)

$$Q = \frac{|X_D|}{R_D} = \frac{|X_C|}{R_D} = \frac{|V|}{e} \tag{4.7}$$

where X_D is the reactance of the coil, X_C is the reactance of the capacitor and R_D is the resistance in the oscillation loop.

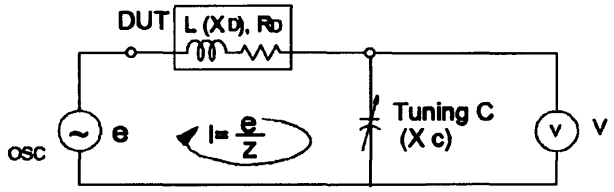

Fig. 4.10 Conceptual circuit diagram for measuring Q-factor

As the changes in Q result in changes in amplitude or frequency of V, either peak detection or frequency detection can be used for Q measurement. A peak-detection based Q-factor measuring system has been developed for reinforcement imaging with a single coil sensor (Miller *et al.* 2005).

C. Induced voltage

For separate driving-pickup coils, it is common to only measure the induced voltage from the pickup coil to estimate the properties of MUT. The conceptual circuit diagram for this method is shown in Fig. 4.11. A VCCS with a constant ac current is used for energise the driving coil, so that a stable primary magnetic field, B_0, is created. When the DUT is placed in the sensing space, it induces a perturbation field, B'. The total field, B_{total}, is superimposed from the primary field and the perturbation field

$$B_{total} = B_0 + B' \tag{4.8}$$

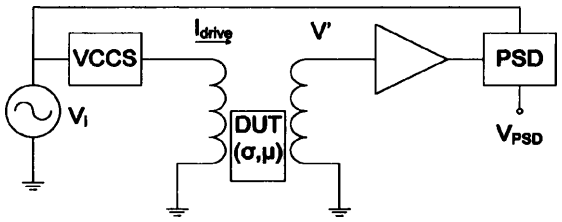

Fig. 4.11 Conceptual circuit diagram for measuring induced voltage

The induced voltage from the pickup coil, which can be described in equation 2.9, is measured and demodulated to derive the in-phase and quadrature components relative to the driving signal. The influence of the primary field can be subtracted using the calibration data taken from an empty space or from a reference coil.

The measuring circuitry of this method is simpler than the self-impedance method, because only the induced voltage is measured. However, the working frequency is usually cannot exceed several hundred kHz, because the output impedance of the current source degrades significantly at higher frequencies. Therefore, this method is suitable for measuring MUT with high conductivity/permeability values, so that the generated perturbation field is strong enough to be detected. This method is used in Electromagnetic Tomography (EMT) systems for conductivity imaging (Peyton *et al.* 1996) and many other NDT related applications (Blitz 1991).

D. Mutual inductance

Another method used with separate driving-pickup coils is to measure the mutual inductance between them. Similar to measuring the self-impedance, this method requires measuring both the driving current and the induced voltage. Fig. 4.12 shows the conceptual circuit diagram for this method. The mutual inductance between a pair of driving-pickup coil can be expressed by

$$M_{12} = \frac{V'}{I_{drive}} \tag{4.9}$$

where I_{drive} is the current flowing through the driving coil and V' is the induced voltage from the pickup coil.

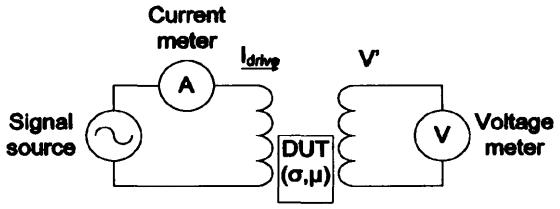

Fig. 4.12 Conceptual circuit diagram for measuring mutual inductance

This method can also be implemented with an impedance analyser. In contrast to the previous method, the signal source in this method can be either current or voltage. Therefore, a signal with higher frequencies (above MHz) can be used to drive the coil, which makes this method suitable for measuring MUT with low conductivity/permeability values. This method has been used in EMT systems for medical imaging of human body compositions (Griffiths 2001).

4.1.3 Challenges for multi-channel multi-modality sensing system

It is desirable to develop a multi-channel system to interface to the capacitive and coil sensor array designed in Chapter 3. In particular, the system should be able to take measurements from the dual-modality sensor array.

General issues with a multi-channel multi-modality system include interfacing with different sensors and data coordination (Hoyle *et al.* 2001). Instead of combining the individual instrumentation systems to form a multi-modality system, Hoyle proposed a general platform, which shares the common parts in data acquisition and communication, so that the multi-modality system is more integrated and easier to coordinate (Qiu *et al.* 2007).

Imaging systems based on impedance measurement are widely used in medical (Webser 1995, Brown 2001), process monitoring (Beck *et al.* 1996, York 2001) and NDT (Blitz 1991), where their hardware designs, measurement range and accuracy are often application-specific. Impedance analysers are designed for general-purpose impedance measurement, which can be used in many different applications. The shortcomings of impedance analysers are that they are bulky, have low acquisition rate and limited measurement channels. In particular, when different types of sensors are used or measurements are taken from different sensor electrodes, the measurement setup or terminal connections need to be changed manually.

However, impedance analysers can deliver excellent performance in terms of reliability, resolution and accuracy. It will be shown that an impedance analyser can be used to take measurements from both capacitive and coil sensors. To enhance the flexibility in sensor connection, a multiplexer (MUX) unit can be purposely designed to work with an impedance analyser (e.g. HP4192A from Agilent), forming a multi-channel multi-modality imaging system. In this thesis, an HP4192A-based ECT system (Yang 2007) is further developed to enable multi-modality sensing for capacitive and coil sensors.

4.2 HP4192A-based multi-channel multi-modality imaging system

4.2.1 Hardware design

The overview of the multi-channel multi-modality imaging system is shown in Fig. 4.13. There are three major parts in the system: a host PC, an HP4192A and an MUX unit. The MUX unit consists of reed relay switch arrays to extend the number of measurement

channels, and to enable different terminal configurations for various sensors and measurement protocols. It has two sub-MUX units: one in 4TP configuration with up to 256 channels, and the other in mutual inductance configuration with up to 20 channels. The MUX unit is connected to H_{CUR}, L_{CUR}, H_{POT} and L_{POT} terminals of HP4192A and can switch between the 4TP and the mutual inductance configurations. The MUX unit is controlled by a data acquisition board (NI PCI-6024E) and two data acquisition units (NI USB-6008). A PCI IEEE-488 board is used for communication between HP4192A and the host PC.

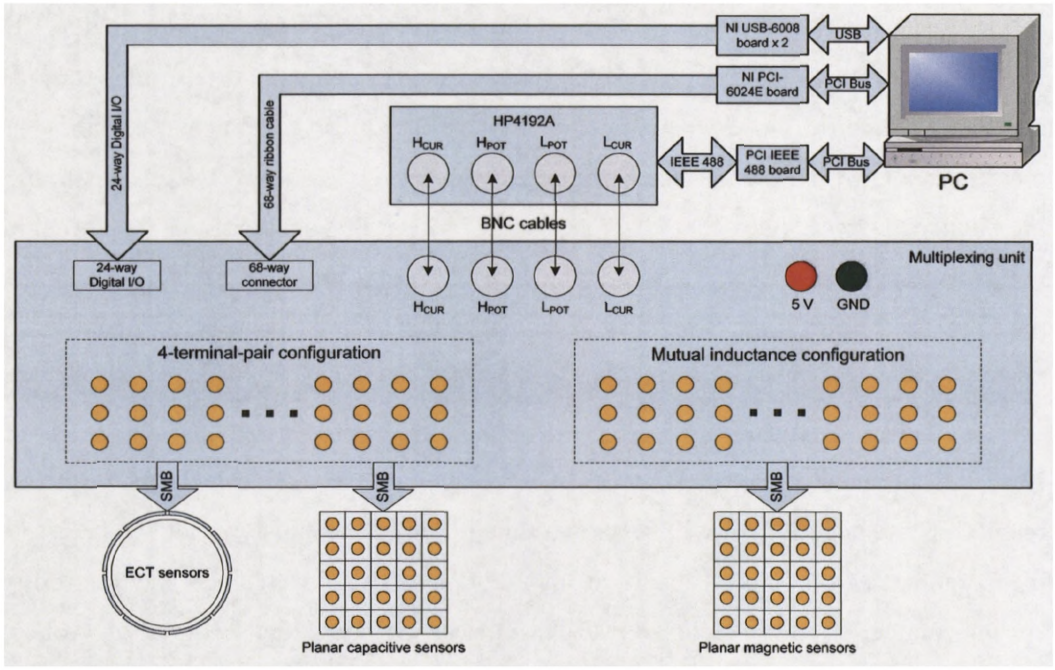

Fig. 4.13 Overall system diagram

The 4TP configuration is recommended to connect a DUT to HP4192A (see Fig. 4.14 (a)) (Agilent Technologies 2006). It can be used to measure *C* and *G* between different electrodes of a capacitive sensor or the self impedance of a coil, but not the mutual inductance between two coils. To make use of HP4192A for mutual inductance measurement, a different terminal configuration should be considered. If a driving coil is connected to the signal source via the H_{cur} terminal, the driving current can be measured by the vector current meter via the L_{cur} terminal. If the pick-up coil is connected directly to H_{pot} and L_{pot} terminals, the induced voltage can be measured by

the vector voltage meter (see Fig. 4.14 (b)). In this way, the mutual inductance can be expressed by

$$M_x = \frac{V_x}{I_x} = R + jX \tag{4.10}$$

where V_x is the voltage measured from the pickup coil and I_x is the current measured from the driving coil.

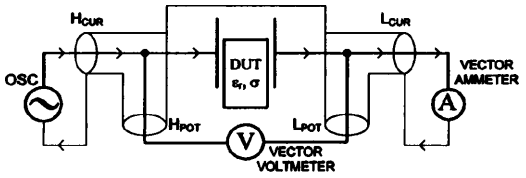

(a) 4-terminal-pair configuration

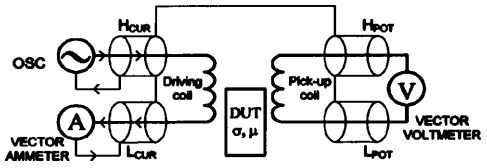

(b) Mutual inductance configuration

Fig. 4.14 Equivalent circuits for different sensor connections

To further enhance the flexibility for electrode configuration, each measurement channel is assigned to a number of different modes. In the 4TP configuration, each channel can be configured as excitation, detection, floating or grounded. In the mutual inductance configuration, each channel can be configured as excitation or detection. The reed relays in the MUX are controlled by NPN transistors as shown in Fig. 4.15. The connection diagram for switching between the 4TP and mutual inductance configurations is shown in Fig. 4.16.

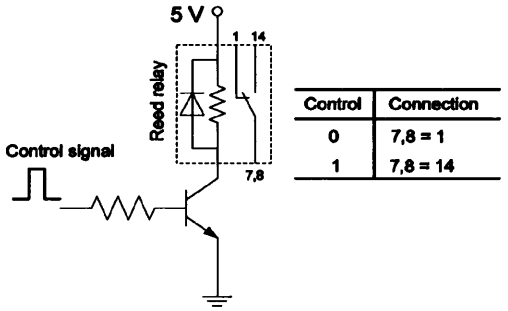

Fig. 4.15 Reed relay control

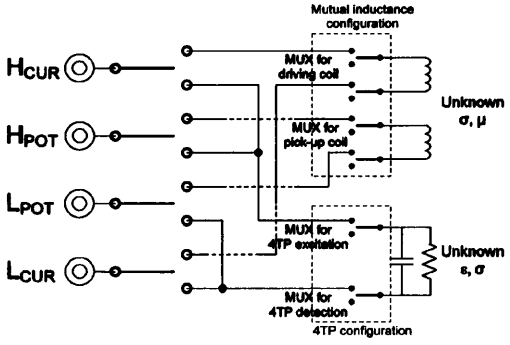

Fig. 4.16 Switching between 4TP and mutual inductance configurations

The data acquisition rate of HP4192A depends on the integration time – high speed, normal or averaged (HP 1987). In this system, normal speed is selected as a default setting to compromise between the data acquisition rate and the measurement accuracy. The integration time for *C/G* or *R/X* measurement is between 152 – 162 ms when the measurement frequency is set above 1 kHz. The acquisition rate of the overall system depends on the number of electrodes in a sensor and the measurement protocol. For example, taking into account the time for multiplexing, it takes about 6 seconds to collect 28 independent measurements from an 8-electrode ECT sensor, and about 8 seconds to obtain 36 measurements from the 6×6 coil array. High speed or averaged integration time can also be selected as appropriate.

4.2.2 Software design

The system software has a layered structure. A DLL written in C++ manages the lower level communication and data exchange between the host PC and the USB units and the PCI board by using device drivers. The DLL also provides a script-based software interface that enables integration with Matlab. A GUI has been designed in Matlab to control data acquisition in the Get Dialog, to implement different algorithms in the Reconstruction Dialog and to carry out further data analysis in the Compare Dialog. Fig. 4.17 shows the structure of the system software. Fig. 4.18 shows the GUI with an image obtained from an ECT sensor.

To implement data acquisition, several settings need to be specified in the GUI. First, the electrodes used with a specific sensor need to be defined as a group, where the channel numbers and the associated scan functions need to be specified. This enables the GUI to take measurements from sensors of different types or different number of electrodes. It also enables easy implementation of different measurement protocols. Second, the measuring mode for HP4192A (e.g. *C/G*, *R/X* or *Z/θ*) and the scanning frequency or frequency sweep points need to be specified. Finally, the number of iterations, delay time and the name and directory of the file for saving the measurement data need to be specified.

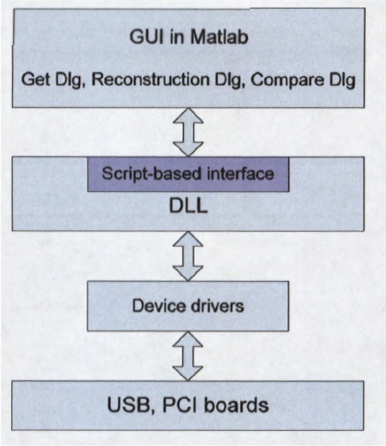

Fig. 4.17 Structure of the software

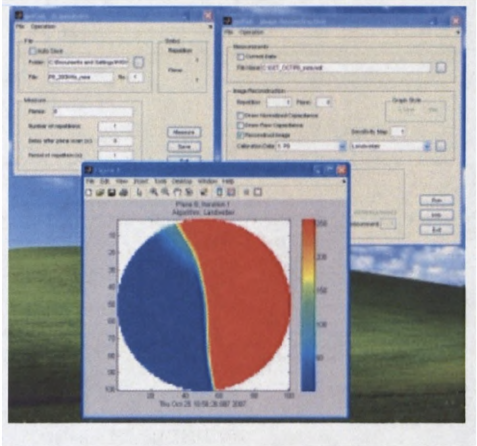

Fig. 4.18 GUI with reconstructed image

4.2.3 System performance evaluation

System performance has been evaluated for the 4TP and the mutual inductance configurations.

A. 4TP configuration

An 8-electrode ECT sensor was used to evaluate system performance in the 4TP configuration, with the electrodes connected to a group of 8 channels in a sub-MUX unit. The independent inter-electrode measurements were acquired in a frequency range of 100 kHz – 10 MHz with 10 frequency points per decade. The measurement distribution is assumed normal when the instrument noise, temperature, frequency and humidity are taken into account. To estimate the measurement uncertainty with the minimised acquisition time, 30 measurements were taken for each electrode pair at every frequency point. C and G measurements were taken to calculate their means & standard deviations. To estimate the drift, the same tests were repeated the next day and the differences between the two sets of measurements were calculated. The means, standard deviations and drift for C and G measurements are given in Fig. 4.19. The resolutions for C and G are 0.1 fF and 1 nS respectively. The noise level for C and G measurements in the frequency range of 100 kHz – 2 MHz is less than 1 fF, and less than 10 nS respectively. At below 2 MHz, the drift for C in one day is less than 10 fF

and less than 10 nS for *G*. Similar resutls were obtained for other channels in the 4TP sub-MUX unit.

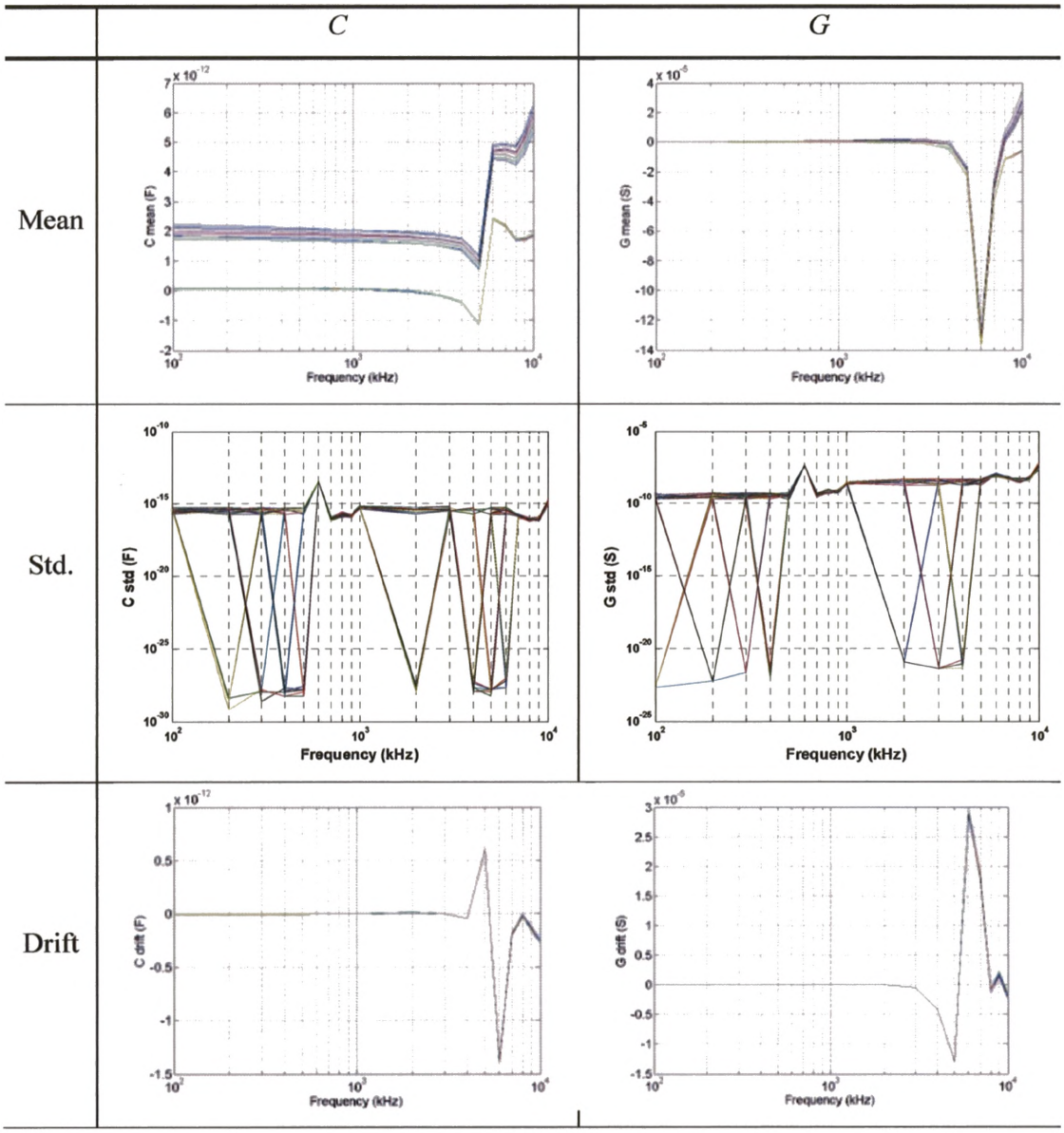

Fig. 4.19 Mean, standard deviation and drift of *C* and *G* measurements

It is also noticed that the measurements for C and G are both frequency dependent, with some measurements being negative in a certain frequency range. In addition, the resonance-like effect have been observed at higher frequencies around 5 to 10 MHz. To understand these observations, it is necessary to further analyse the 4TP configuration

with the consideration of parasitic components along the measuring channel, e.g. from MUX box and coaxial cables.

Negative capacitance measurement has been reported and explained in (Mamichev *et al.* 1998, Okawa *et al.* 2003). In their circuit topologies, the unknown capacitance and the parasitic components in the circuit formed a three-terminal system, and the measurement was taken from the two terminals connected to the test fixture. The measured impedance can be modelled using the components in the three-terminal system.

As opposed to the ideal case, the coaxial cable, reed relay and PCB tracks can be modelled by the combinations of L, R and C components in a real world (Agilent Handbook 2006). As the coaxial cable, reed relay and PCB tracks are connected in series in one measurement channel, L_P and R_P can be used to represent the total parasitic inductance and resistance respectively along the signal path. C_{S1} can be used to represent the total parasitic capacitance from the excitation side while C_{S2} can be used to represent the total parasitic capacitance from the detection side. Therefore, the equivalent circuit for measuring a dielectric DUT using the 4TP configuration can be described as shown in Fig. 4.20.

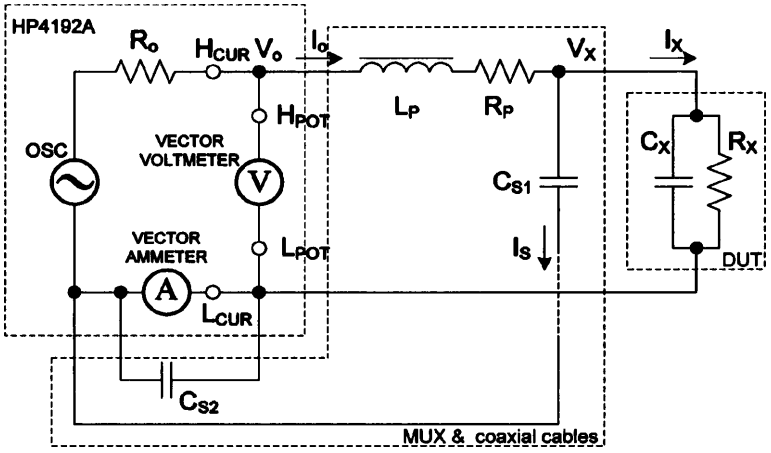

Fig. 4.20 Circuit diagram for measuring dielectric with 4TP configuration

From the circuit diagram, we have

$$I_o = I_s + I_x \tag{4.11}$$

$$I_o = \frac{V_o - V_x}{Z_p} \tag{4.12}$$

$$I_s = \frac{V_x}{Z_s} \tag{4.13}$$

$$I_x = \frac{V_x}{Z_x} \tag{4.14}$$

where V_o is the voltage output from the signal source, I_o is the current flowing out of the signal source, V_x is the voltage drop across the DUT, I_x is the current flowing through the DUT, I_s is the current flowing through the parasitic capacitance, Z_p is the impedance of the parasitic in the signal path, Z_x is the impedance of the DUT and Z_s is the impedance of the stray capacitance.

The measured impedance, Z_{mea}, using the 4TP configuration is

$$Z_{mea} = \frac{V_o}{I_x} \tag{4.15}$$

Eliminating and rearranging the variables from equations (4.11 – 14), the above equation becomes

$$Z_{mea} = Z_x + Z_p + \frac{Z_x Z_p}{Z_s} \tag{4.16}$$

In an ideal case, when the parasitic components from the signal path are negligible ($Z_p = 0$) and the stray capacitance is sufficiently small ($Z_s = \infty$), the measured impedance equals to the impedance of the DUT ($Z_{mea} = Z_x$). If the parasitic components and the DUT are all considered, where

$$Z_p = R_p + j\omega L_p \tag{4.17}$$

$$Z_s = \frac{1}{j\omega C_{s1}} \tag{4.18}$$

$$Z_x = R_x // \frac{1}{j\omega C_x} = \frac{R_x}{1 + j\omega R_x C_x} \tag{4.19}$$

the measured impedance can be expanded and given as

$$\begin{aligned} Z_{mea} &= \frac{1}{1+\omega^2 R_x^2 C_x^2} \cdot \begin{Bmatrix} \left[R_x + R_p + \omega^2 \left(R_x C_x L_p + R_x^2 R_p C_x C_{s1} - R_x C_{s1}\right)\right] \\ + j\omega\left[\left(L_p + R_x R_p C_{s1} - R_x^2 C_x\right) + \omega R_x^2 C_x C_{s1} L_p\right] \end{Bmatrix} \\ &= R + jX \end{aligned} \tag{4.20}$$

The measured conductance and capacitance are given as

$$G = \frac{X^2 R}{R^2 + X^2} \tag{4.21}$$

$$C = \frac{B}{\omega} = \frac{R^2 X}{\omega\left(R^2 + X^2\right)} \tag{4.22}$$

While the MUX box can enhance the flexibility in sensor connections for HP4192A, it significantly extends the length of the signal path between the DUT and HP4192, and increases the influence of parasitic components in the system, in that (1) R_P and L_P are significantly increased, which are measured to be 1.3 Ω and 5.6 μH at 1 kHz, 1.8 Ω and 1.8 μH at 100 kHz, and 3.2 Ω and 1.1 μH at 1 MHz; (2) the length of the coaxial cable is more than 1.5 m, and thus C_S is in the order of more than 100 pF (Yang 1996 2). Long coaxial cable also makes the ABB circuit difficult to balance at higher frequencies (Agilent Technologies 2006). The recommended length for the coaxial cable should be less than 0.5 m.

From equation 4.20–22, both the measured conductance and capacitance have frequency dependent negative components. For the G measurement, having neglected the smaller order terms, its polarity mainly depends on the value of $R_x(1 - \omega^2 C_{s1})$, which starts to become negative when $\omega^2 C_{s1} < 1$. If C_{S1} = 100 pF, the cross-zero frequency point is 15.9

kHz. This is why the G measurements are mainly negative throughout the test frequency range. For the C measurement, its polarity depends on the value of $R_xR_PC_{SI}$ + $\omega R_x^2C_xC_{SI}L_P$ - $R_x^2C_x$, which is much more complex. Given the values for R_P, L_P, C_{SI}, and considering that R_x in the order of GΩ, the C measurements remain positive throughout the test frequency range.

Resonant-like effect appeared around 5 MHz, which not only results in negative C measurements, but also increases the measurement noise and drift significantly. This is because the parasitic components are also frequency dependent, as can be seen from the variations in measurements. It is difficult to model the frequency characteristics of the parasitic components. Therefore, to ensure reliable C/G measurements, the working frequency for the 4TP configuration should be below 5 MHz.

B. Mutual inductance configuration

Using HP4192A for mutual induction measurement has not been reported in literature. To validate the proposed method, a pair of concentric air-core solenoids (30 turns each, 76 mm in diameter, spacing of 6 mm) was used as the test object. The mutual inductance between them was measured from 1 kHz to 100 kHz with 10 frequency points per decade using both the HP4192A-based system and a Solartron impedance analyser (1260A). R and X measurements were compared in Fig. 4.21.

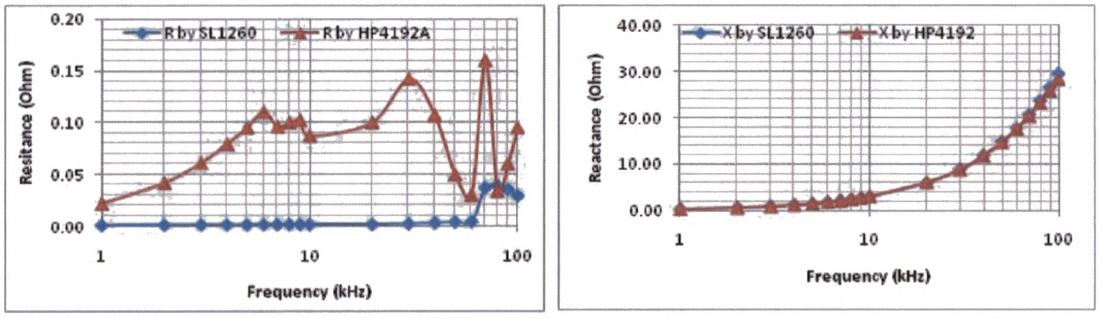

(a) R over frequency (b) X over frequency

Fig. 4.21 Mutual inductance measured by HP4192A and SL1260

It can be seen that *X* measurements by HP4192A are almost identical with measurements from 1260A, but *R* measurements by HP4192A are not as stable as from 1260A. The magnitude of *R* is more than 100 times smaller than *X*, showing that the inductive component is predominant in the impedance. This test confirmed that HP4192A can measure mutual inductance.

To evaluate the system performance with the mutual inductance configuration, a 6×6 PCB-coil array designed in Chapter 3 was connected to the appropriate sub-MUX unit. *R/X* measurements were taken from 36 pairs of driving/pick-up coils in a frequency range of 1 kHz – 100 kHz with 10 frequency points per decade. Other experiment settings are the same as in 4TP evaluation. The means, standard deviations and drift for *R/X* measurements are given in Fig. 4.22. From the plots, the resolution for *R/X* measurements is 0.1 mΩ, the noise level for R/X is less than 2.5 mΩ and drift in one day for R/X is less than 7 mΩ.

	R	*X*
Mean	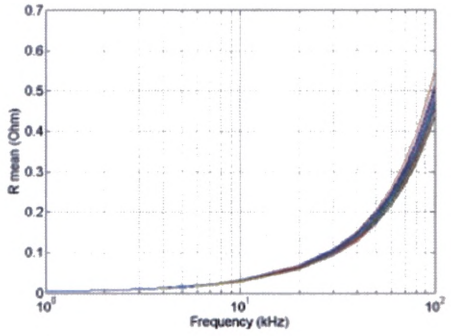	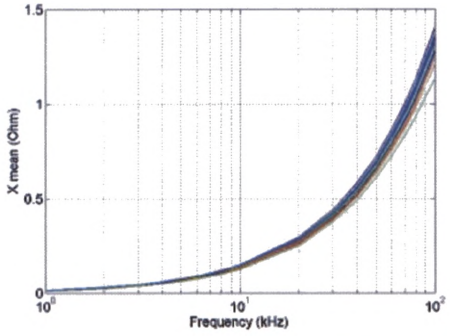
Std.	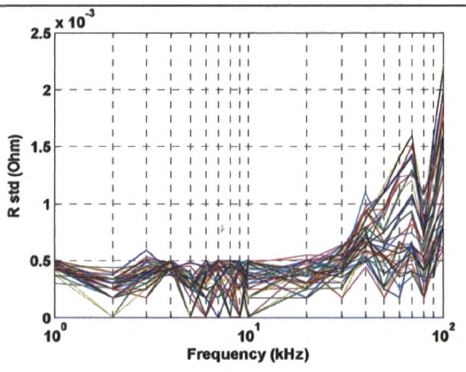	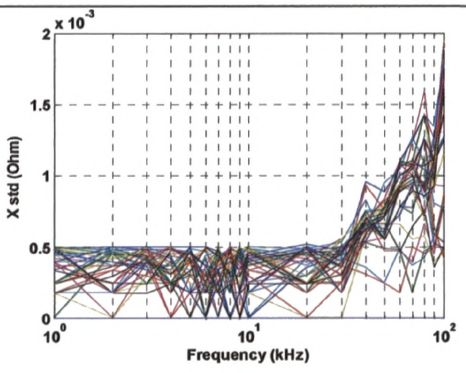

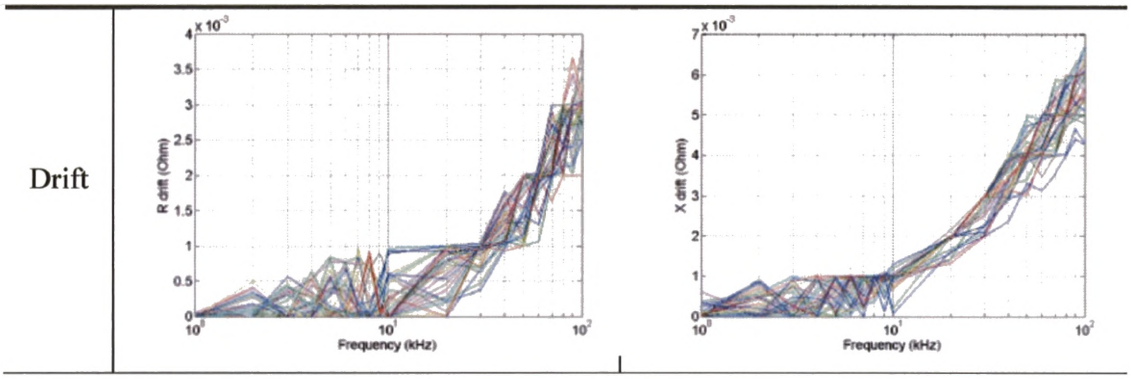

Fig. 4.22 Mean, standard deviation and drift for R and X measurements

It has been observed that the drift in the mutual induction configuration increases with frequency significantly. Further analyse for the system performance in the mutual inductance configuration has also been carried out. Fig. 4.23 shows the equivalent circuit for the mutual inductance configuration with the consideration of of parasitic components, including the MUX box, coaxial cables and PCB-coil itself.

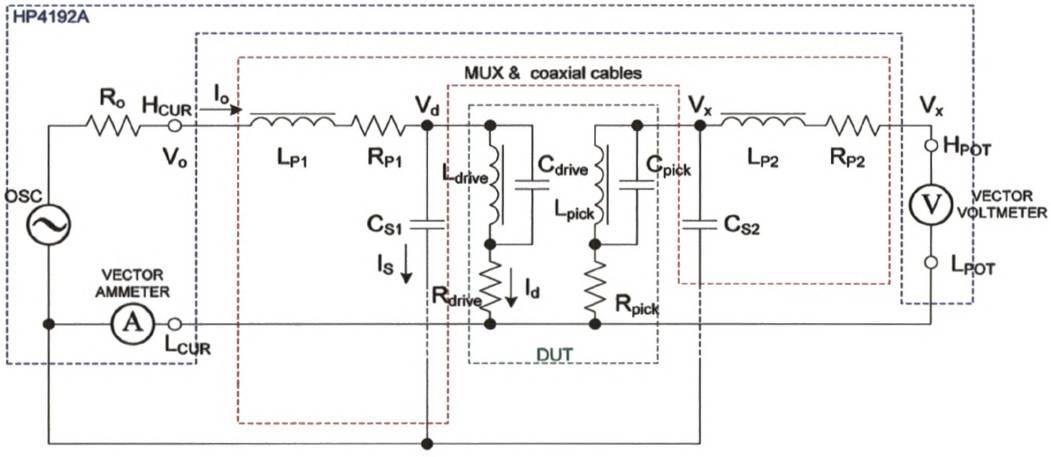

Fig. 4.23 Circuit diagram for mutual inductance configuration

As the coaxial cable, reed relay and PCB tracks are connected in series with the PCB coil, L_{P1} and R_{P1} are used to represent the total parasitic inductance and resistance respectively along the driving path, and C_{S1} is used to represent the total parasitic

capacitance from the driving side. L_{P2} and R_{P2} are used to represent the total parasitic inductance and resistance respectively along the pickup path, and C_{S2} is used to represent the total parasitic capacitance from the pickup side. R_{drive} and C_{drive} are the resistance and the parasitic capacitance of the driving coil while R_{pick} and C_{pick} are the resistance and the parasitic capacitance of the pickup coil. The driving coil and pickup coil are in a separate loop. As the pickup coil is in a loop with the vector voltage metre, the current in this loop is negligible. From the circuit diagram,

$$I_o = I_s + I_d \tag{4.23}$$

$$I_o = \frac{V_o - V_d}{Z_{p1}} \tag{4.24}$$

$$I_s = \frac{V_d}{Z_{s1}} \tag{4.25}$$

$$I_d = \frac{V_d}{Z_d} \tag{4.26}$$

where V_o is the output voltage from the signal source, I_o is the output current from the signal source, I_s is the current flowing through the stray capacitance, V_d is the voltage across the driving coil, I_d is the current flowing through the driving coil, V_x is the induced voltage from the pickup coil, Z_{p1} is the impedance of the signal path along the driving coil, Z_d is the impedance of the driving coil and Z_{s1} is the impedance of the stay capacitance associated with the driving coil.

The measured mutual inductance between the driving-pickup coil is given as

$$M = \frac{V_x}{I_d} \tag{4.27}$$

Eleminating and rearranging the variables, the above equation becomes

$$M = \frac{V_x}{V_o}\left(Z_d + Z_{p1} + \frac{Z_d Z_{p1}}{Z_{s1}}\right) \tag{4.28}$$

In an ideal case, when the parasitic component along the signal path is negligible ($Z_{p1} = 0$) and the stray capacitance is small ($Z_{s1} = \infty$), the measured mutual inductance is given as

$$M = \frac{V_x}{V_o} Z_d \tag{4.29}$$

When the parasitic components are included, where

$$Z_{p1} = R_{p1} + j\omega L_{p1} \tag{4.30}$$

$$Z_s = \frac{1}{j\omega C_{s1}} \tag{4.31}$$

$$Z_d = R_d + j\omega L_d \,//\, \frac{1}{j\omega C_d} \approx R_d + j\omega L_d \tag{4.32}$$

the measured mutual inductance can be expanded and given as

$$\begin{aligned} M &= \frac{V_x}{V_o} \cdot \begin{Bmatrix} \left[R_d + R_{p1} - \omega^2 C_{s1}\left(L_d R_{p1} + L_{p1} R_d\right)\right] \\ + j\omega\left[\left(L_d + L_{p1}\right) + C_{s1} R_d R_{p1} - \omega^2 C_{s1} L_d L_{p1}\right] \end{Bmatrix} \\ &= R + jX \end{aligned} \tag{4.33}$$

The MUX box increases parasitic components in the mutual inductance configuration and causes similar problems. For the mutual inductance configuration, R_P + R_D are measured to be 24.4 Ω at 1 kHz, 30.7 Ω at 100 kHz, 41.1 Ω at 500 kHz and 44 Ω at 1 MHz. L_P + L_D are measured to be 75 μH at 1 kHz, and 61.7 μH at 100 kHz, 57.7 μH at 500 kHz and 47.9 μH at 1 MHz. C_S is in the order of more than 150 pF due the length of the coaxial cables.

From equation 4.33, R and X measurements also have frequency dependent negative components. For R measurements, its polarity depends on the value of R_d + R_P -

$\omega^2 C_{SI}(L_d R_{PI} + L_{PI} R_d)$. It indicates that R measurement is constant at low frequencies and drops significantly when the frequency increases, which is reflected in Fig. 3.18. Given the values for the parasitic components at 500 kHz, $\omega^2 C_{SI}(L_d R_P + L_P R_d)$ is in the order of 3 Ω, which is about 10 % of $R_d + R_P$. As this term introduces non-linearity and uncertainty in measurements, to ensure reliable measurements, the workign frequency for measuring R should be below 500 kHz. For X measurements, its polarity mainly depends on $L_d + L_P - \omega^2 C_{SI} L_d L_P$. It indicates that at lower frequencies, X measurement increases linearly frequency, but drops significantly at higher frequencies. Given the values the parasitic components at 500 kHz, $\omega^2 C_{SI} L_d L_P$is in the order of 5×10^{-6}, which is about 10 % of $L_d + L_P$. Therefore, the working frequency for X measurement should also be below 500 kHz. Concluding from both R and X measurements, the working frequency for the mutual inductance configuration should be below 500 kHz.

To further extend the working frequency range and to reduce the uncertainty in measurements, it is necessary to reduce the values for the parasitic components and make it less frequency dependent. This can be achieved by reducing the length of the signal path and careful PCB design for the MUX.

C. Comparing performance with other systems

The HP4192A-based multi-channel multi-modality imaging system has been further compared with an AC-ECT system (Yang 2001) and a 1260A (Solartron Analytical 1996) in terms of the measured parameter (*C*, *G*, *R* or *X*), measurement range, resolution, number of channels, spectroscopy, data acquisition rate and sensing modality (see Table 4.1). The HP4192A-based system has better performance in most aspects, except for data acquisition rate, which is lower than the AC-ECT system, and resolution, which is lower than 1260A.

Table 4. 1 Comparison of performances of different systems

	HP4192A-based system	AC-ECT system	1260A
Measured parameter	*G/C* or *R/X*	*C* or *G*	*R/C* or *R/X*
Range and Resolution	*R*: 1 Ω – 10 MΩ, 4½ digits *G*: 10 μS – 10 S, 4½ digits *C*: 1 pF – 10 mF, 4½ digits *L*: 100 nH – 1000 H, 4½ digits	*C*: 0 – 2 pF Resolution: 0.1 fF	*R*: 10 mΩ – 100 MΩ, 5 digits *C*: 1 pF – 10 mF, 5 digits *L*: 100 nH – 1000 H, 5 digits
Number of channels	256 for *G/C*, 20 for *R/X*	16	2 for *R/C* or *R/X*
Spectroscopy	5 Hz – 13 MHz	10 kHz – 500 kHz	10 μHz – 32 MHz
Data acquisition rate	50 ms – 3.1 s for one measurement	1.1 – 1.4 ms for one measurement	10 ms – 10^5 s for one measurement
Sensing modality	Resistive, capacitive, magnetic	Capacitive	Resistive, capacitive, magnetic

4.2.4 A method to obtain measurement from single-electrode capacitive sensor

HP4192A cannot be directly used to measure capacitance from the single-electrode sensor, because the virtual terminal usually cannot be connected to the measuring circuit. However, as the single-electrode capacitance sensor can be modelled as a parallel-plate capacitor, a method which uses an array of electrodes as excitation and a big electrode as detection can be used to simulate the single-electrode sensor. The big detection electrode made from a plastic cover will act as the virtual terminal, so that measurements can be taken by the HP4192-based system. Fig. 4.24 shows the diagram for taking measurements from the single-electrode sensor array by HP4192-based system.

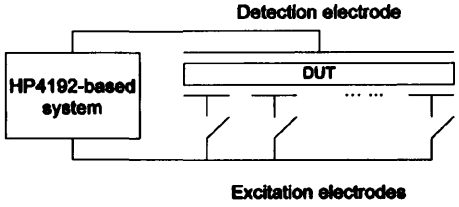

Fig. 4.24 Method to measure from single-electrode sensor by HP4192-based system

4.3 Imaging reconstruction algorithms

4.3.1 Imaging methods used with capacitive and coil sensors

Although capacitive and coil sensors have different sensing principles, image reconstruction with capacitive and coil sensors are similar to each other, which can be categorised into a number of different methods, including direct imaging, model-based imaging, tomography, and interpolation-based imaging.

In a direct method, an image is directly derived from measurements without solving any forward or inverse problem. This method is simple, fast, and can be implemented online. However, as the number of pixels in an image is related to the number of electrodes, the size of the sensor array will be large if a high image resolution is required. The direct method has been used in fingerprint imaging with single-electrode capacitive sensor array (Lee *et al.* 1999) and fast flow imaging with inter-digital sensor array (Da Silva 2008).

The model-based method involves generating the measurement grid or look-up table by analytically solving the sensor response, and applying the inverse interpolation to produce an image (Schliker 2006). Although generating the measurement grid is a time-consuming task, the simplicity and fast speed of the inverse interpolation makes it possible to implement imaging and parameter estimation online. However, deriving analytical solutions can be difficult and limited to sensors with simple or symmetrical geometries to facilitate approximation in field calculations. The model-based method has been used in absolute imaging by inter-digital capacitive and magnetic sensor arrays (Mameshev *et al.* 2004, Schliker 2006).

Tomographic imaging with capacitive and coil sensors belongs to a family called electrical tomography. It requires solving the forward problem to obtain the sensitivity distribution for a sensor, and solving the inverse problem to obtain an image (Xie *et al.* 1992, Yang *et al.* 2003). In contrast to the model-based method, tomography has a relatively general applicability in that it can be used with different sensors and applications. Tomography has been used in dielectric imaging with ring-shaped capacitive sensor array (Frounchi *et al.* 2003), landmine detection with square-electrode

capacitive sensor array (Cheng 2008) and security scanning with coil arrays (Gonzalez-Nakazawa 2007).

The interpolation-based imaging consists of various interpolation and image enhancement methods. Interpolation can be implemented in the frequency domain or in the spatial-domain, depending on the application and availability of analytical models. A frequency-domain based interpolation method has been used in reinforcement imaging with coil sensor (Zaid *et al.* 2002). A spatial-domain-based interpolation method has been used with solid-state sensor array (Benitez *et al.* 2007). Another type of spatial-domain interpolation is based on the sensitivity coefficients, where a set of coefficients obtained from a sensitivity distribution is used in interpolation. This method is used for security imaging with ring-shaped capacitive sensor array (Cheng 2008). In general, the interpolation-based method can generate an image with higher resolution than the dimension of the measurement without high computational cost, and thus can be implemented online.

In Chapter 3, the sensitivity distributions for various sensors were investigated to facilitate sensor design, which can also be used for image reconstruction. To compromise between accuracy, resolution and imaging speed, the sensitivity-coefficients-based interpolation method will be used for 2D imaging with the ring array, single-electrode array, coil array and dual-modality array. In addition, tomography will be used for 2D imaging with the adaptive array.

4.3.2 Image construction by tomography

The forward problem in electrical tomography concerns with modelling the sensor to predict the sensor output in response to a set of boundary conditions being applied to a certain material distribution. The linearised approximation of the forward problem can be given as (Xie *et al.* 1992)

$$\lambda = Sg \tag{4.34}$$

where λ is the normalised measurement vector, S is the sensitivity map for the sensor model and g is the normalised distribution of a material.

The inverse problem concerns with obtaining the distribution of a material property using the measurements and the sensitivity map. Ideally, if the inverse of the sensitivity map exists, the distribution of a material can be derived from

$$g = S^{-1}\lambda \tag{4.35}$$

In most electrical tomography applications, however, the inverse of the sensitivity map does not exist and the inverse problem to be solved is often ill-posed and ill-conditioned (Yang *et al.* 2003). To solve such a problem, either the non-iterative or iterative algorithm can be used. A non-iterative algorithm is relatively simple and can be implemented online. However, it can only achieve a moderate accuracy for qualitative analysis. An iteratively algorithm is usually solved in a least square sense, i.e. minimising the error term $\|Sg - \lambda\|$, and thus, a higher accuracy can be achieved for the image. However, it is time-consuming and difficult to implement on-line.

Linear back projection (LBP) is the simplest non-iteration method, which uses the transpose of the sensitivity map, S^T, to replace the inverse of the sensitivity map (Xie *et al.* 1992)

$$\hat{g} = S^T\lambda \tag{4.36}$$

where $\hat{g}$ is the reconstructed image representing the distribution of material.

This method is a poor mathematical approximation, which results in poor accuracy for the reconstructed image. However, it is still widely used in electrical tomography due to its simplicity (Yang *et al.* 2003).

Landweber iteration is an optimisation method based on steepest gradient decent, which was introduced to ECT by Yang (1999). It can be expressed by

$$\begin{cases} \hat{g}_0 = S^T \lambda \\ \hat{g}_{k+1} = P\left[\hat{g}_k - \alpha S^T (S\hat{g}_k - \lambda)\right] \end{cases} \tag{4.37}$$

$$P\left[f(x)\right] = \begin{cases} f(x) & \text{if} \quad 0 \le f(x) \le 1 \\ 0 & \text{if} \quad f(x) < 0 \\ 1 & \text{if} \quad f(x) > 1 \end{cases} \tag{4.38}$$

where α is the relaxation factor, $\hat{g}_0$ is the initial solution for starting the iteration, $\boldsymbol{P}$ is a projection operator used to control the convergence of iteration.

Landweber iteration is fast in reducing the error term and less computational demanding than other iterative algorithms. However, it has semi-convergence characteristics, which causes the increase in image error after passing the minimal point. Landweber iteration is still a popular choice and widely used in ECT (Li 2008).

Due to the above features, both LBP and Landweber iteration will be used with the adaptive array in this thesis. The flowchart for tomographic imaging with the adaptive array is given in the appendix.

4.3.3 Image reconstruction by interpolation based on sensitivity coefficients

The sensitivity coefficients based interpolation method consists of three steps: First each sensing element is divided into n×n pixels, and each pixel is assigned with a normalised sensitivity coefficient based on the 2D sensitivity distribution of a sensor. Second, this set of sensitivity coefficients is applied to the normalised measurement, so that a raw image of n^2 times higher resolution than the measurement matrix can be derived.

$$\hat{g}_o(n,i) = \lambda_n S_i \tag{4.39}$$

where $\hat{g}_o$ is the raw image, λ is the normalised measurement, n is the index of measurement vector, i is the index of the sensitivity coefficients.

The final image is produced by pixel-averaging to smooth the edges.

$$\hat{g}(k,l) = \frac{1}{M} \sum_{k-1}^{k+1} \sum_{l-1}^{l+1} \hat{g}_o(k,l) \tag{4.40}$$

where $\hat{g}$ is the final image, M is the number of pixels for averaging.

Sensitivity coefficient based imaging is used with the ring array, single electrode array, coil array and dual-modality array.

4.4 Fusion

As information obtained from a single modality sensor is usually limited to certain material properties, multi-modality sensors can be used to provide additional or complementary information for an MUT. Consequently, fusion is necessary to improve the accuracy of inference, which can be parameter estimation, image reconstruction or image synthesis. Image fusion with the dual-modality capacitive and coil sensor array will be discussed in the following section.

4.4.1 Fusion in multi-modality imaging

In recent years, there is a growing interest in fusion in multi-modality imaging. In general, fusion can be implemented at different levels: signal level, pixel level and feature level (West *et al.* 1999).

Qiu (2007) presented a simple pixel level fusion used with a dual-modality ECR/ERT system, where the images obtained from ECT/ERT are merged to indicate the boundaries between air/oil/water. Steiner (2006) presented a sequential fusion method used with an ECT/Ultrasound system. In this method, an image is first obtained from the ultrasound sensor, which is then used for ECT to update the sensitivity map and

relaxation factor in a non-linear image reconstruction process. This technique is also used in an EIT/Ultrasound system for bio-electromechanical imaging (Steiner *et al.* 2008), showing that sequential fusion can improve the spatial resolution and detection depth of the system. Basarab-Horwath (2001) presented a fusion based material classification method used with an EIT/Infrared system, where principle component analysis (PCA) is applied to image parameters derives from the dual-modality sensors to identify samples of different materials.

The above methods are based on spatial fusion with images obtained from single-frequency measurements. As an MUT may exhibit frequency dispersive characteristics, spectrum fusion based on wideband measurements is exploited by Nahvi (2008, 2009). Two fusion methods have been used: a lookup table based on spectral characteristics is used for component identification while a model-based method is used for parameter estimation. Images obtained from different frequencies can be used to illustrate the transition in a mixing process.

4.4.2 A fusion method with the capacitive and coil sensor array

The electrical properties of an MUT can be generally characterised by permittivity, conductivity and permeability. Concluding from the analysis and experiments in the previous chapters, a capacitive sensor array can produce permittivity image. However, the performance of the capacitive sensor array may be affected by conductivity in the system. A coil sensor array can produce conductivity/permeability images and is not affected by permittivity. Therefore, the dual-modality capacitive and coil sensor array can be used to generate permittivity/conductivity/permeability images for an MUT.

Using the sensitivity coefficients, the interpolated C, R and X images can be obtained from the measurements. From the experiments for cross-talk evaluation, a lookup table between the values of the normalised C, R, X measurements and the corresponding material properties can be established, as given in Table 4.2. The detailed explanation of material properties and pixel assignment is given in the dual-modality experiments in the next chapter. Using this lookup table, pixel based fusion can be carried out, and the binary permittivity/conductivity/permeability images can be generated from the

interpolated C/R/X images. The flowchart for implementing imaging and fusion algorithms with the dual-modality sensor array is given in Appendix.

Table 4.2 Lookup table for pixel assignment

C	>0	>0	>0	Others
R	0	>0	>0	
X	0	<0	>0	
Pixel assignment	ε=1, σ=0, μ=0	ε=0, σ=1, μ=0	ε=0, σ=0, μ=1	ε=0, σ=0, μ=0

4.5 Summary

This chapter presents the design of an imaging system, image reconstruction and fusion algorithms. Having reviewed different methods for taking measurements from capacitive sensors and coil sensors, an HP4192A-based multi-channel multi-modality system has been developed to interface to the single-modality and dual-modality sensor arrays designed in Chapter 3. Although this system cannot be directly used to take measurements from the single-electrode capacitive sensor array, a big electrode made from a plastic cover is used as the virtual terminal, so that the single-electrode sensor array can be measured by HP4192A based system. The performance of the system has been evaluated. The resolutions for C and G measurements are 0.1 fF and 1 nS respectively. The noise level for C and G measurements in the frequency range of 100 kHz – 2 MHz is less than 1 fF, and less than 10 nS respectively. At below 2 MHz, the drift for C in one day is less than 10 fF and less than 10 nS for G. The resolution for R/X measurements is 0.1 mΩ, the noise level for R/X is less than 2.5 mΩ and drift in one day for R/X is less than 7 mΩ. The system is further analysed with the consideration of parasitic components in the MUX box and coaxial cables. It shows that parasitic components may lead to negative measurements and results in measurements uncertainty at higher frequencies. For the current design, the working frequency for the 4TP configuration should be below 5 MHz, and the working frequency for the mutual inductance configuration should be below 500 kHz.

The image reconstruction algorithms are reviewed. LBP and Landweber are chosen to be used with the capacitive adaptive sensor array, while the sensitivity-coefficients-based interpolation method is used with the other sensor arrays. In addition, a lookup table based pixel level fusion will be used to generate permittivity, conductivity and permeability images from the interpolated C, R and X images.

Chapter 5 Results and analysis

This chapter presents the imaging results and analysis for all the sensor arrays. The performance of the sensor arrays are qualitatively analysed in terms of edge detection and spatial resolution, and quantitatively analysed in terms of position and area estimations. Fusion results based on the dual-modality sensor array are also presented.

5.1 Test conditions and definitions

5.1.1 Samples and test conditions

A variety of samples of different materials and shapes have been used, including: a ceramic knife, square and rectangular pieces of Blu-Tack, square pieces of copper sheet, a rectangular piece of aluminium, a steel knife and a pair of steel scissors.

All the experiments were carried out in room temperature. 500 kHz was used for capacitance measurement while 10 kHz was used for mutual inductance measurement. For each sample, 10 measurements were taken and averaged. Noise is removed by applying thresholds using the system noise levels in C, R and X measurements. The measurements were normalised against the calibration from empty sensor arrays.

Table 5.1 Test samples and their dimensions

Samples	Dimension (length × width × height, mm)	Area (mm^2)
Ceramic knife	Irregular	1640
Square piece of Blu-Tack	20 × 20 × 3	400
Rectangular piece of Blu-Tack	60 × 30 × 3.5	1800
Rectangular piece of aluminium	55 × 42 × 1.5	2310
Square piece of copper sheet	20 × 20 × 0.5	400
Steel knife	Irregular	1450
Steel scissors	Irregular	2280

5.1.2 Evaluation methods and parameters

Imaging with single and multiple objects was carried out to qualitatively examine edge detection and spatial resolution for different sensor arrays. To further quantify the imaging results, position and area errors have been used (Xie *et al.* 1994).

The area error, *AE*, can be defined as the ratio of the difference between the estimated area and the true area against the true area

$$AE = \frac{A' - A}{A} = \frac{N_p \times A_{pixel}}{A} - 1 \tag{5.1}$$

where A' is the area of an MUT in an image, N_p is the number of pixels representing the MUT in the image, A_{pixel} is the effective area of a pixel, A is the true area of the MUT.

The effective area of a pixel depends on the resolution of an image and the total area it represents. For the ring array, the single-electrode array, the coil array and the dual-modality array, although the numbers of sensing elements in the arrays are different, every sensing element has the same size of 20 × 20 mm^2, and is evenly divided into 9 pixels. Therefore, each pixel corresponds to an area of 400/9 = 44.4 mm^2. For the adaptive array, the whole sensing area is 80 × 80 mm^2, and the image resolution is 20 × 20. Thus, each pixel corresponds to an area of 80 × 80 / (20 × 20) = 16 mm^2.

The true area of an MUT is obtained by direct measurement, as given in Table 5.1. To obtain the estimated area, A', it is necessary to calculate how many number of pixels an MUT possesses in an imaget. An image threshold has been used to define the boundaries of an MUT, where the pixels of greater than the threshold value are set to 1 while others are set to 0. In such a way, a binary image is derived from the reconstructed image, and the number of pixels of an MUT is the number of 1s in the binary image.

$$\hat{g}_B(p) = \begin{cases} 0, & \hat{g}(p) < t \\ 1, & \hat{g}(p) > t \end{cases} \quad (p = 1,2,...,N) \tag{5.2}$$

where $\hat{g}_B$ is the binary image, $\hat{g}$ is the reconstructed image, p is the index of pixels, t is the threshold value and N is the total number of pixels in an image. For imaging with multiple objects, the estimated area represents the overall area of all the objects.

The absolute position error is defined as the difference between the estimated position of an MUT from an image and its true position. To make it dimensionless, the relative position error, PE, can be related to pixel size by

$$PE = \frac{\|C'(\bar{x}', \bar{y}') - C(x, y)\|}{Pixel \quad size} = \frac{\sqrt{(x'-x)^2 + (y'-y)^2}}{Pixel \quad size} \tag{5.3}$$

where $C'(\bar{x}', \bar{y}')$ is the centre coordinates of an MUT in an image, $C(x, y)$ is the true centre coordinates of an MUT on a sensor array, the pixel size for interpolated image is 20/3 = 6.7 mm, the pixel size for tomographic image is 4 mm.

The true centre coordinates of the MUT were obtained from direct measurement after placing the test sample on the sensor array. The estimated centre coordinates of an MUT were calculated by averaging the coordinates of the pixels an MUT possesses in an image.

$$\bar{x}' = \frac{1}{N_p} \sum_{1}^{Np} x'(i) \tag{5.4}$$

$$\bar{y}' = \frac{1}{N_p} \sum_{1}^{Np} y'(i) \tag{5.5}$$

For imaging with multiple objects, the estimated coordinates represent the overall centre position of all the objects.

5.2 Imaging with capacitive sensor arrays

This section investigates imaging with the three capacitive sensor arrays designed in Chapter 3. Different image reconstruction methods were used.

5.2.1 Concentric-ring-based sensor array

As discussed in Chapter 3, the concentric ring sensor array can work in the transmission mode and the shunt mode, depending on the boundary condition of the object. This sub-section examines imaging with the ring sensor array in different sensing modes. The image reconstruction method is interpolation based on sensitivity coefficients.

A. Imaging with transmission mode and shunt mode

A ceramic knife and a rectangular piece of aluminium were used as test samples for the transmission mode. A grounded cover was used with the ring array to form the shunt mode, as explained in Chapter 3. For the shunt mode, the same test samples were used in three scenarios: (a) ceramic knife with top grounded boundary right above it, (2) aluminium piece with top grounded boundary right above it, and (3) aluminium piece with top grounded boundary 3mm above it. Fig. 5.1 shows the samples, the differences in capacitance between sample measurements and calibration data, and the reconstructed images in different sensing modes. Note that the differences in capacitance are plotted against the index of the measurements obtained from the ring sensor array.

For the transmission mode, the sample measurements are mostly bigger than the calibration data, and form peaks in measurements. For the shunt mode, however, due to the grounded top boundary, the capacitance values decrease. For a dielectric MUT, such as ceramic, although the measurements reduced in the shunt mode, the MUT still results in peaks in measurements as seen in the transmission mode. Therefore, the reconstructed image is also similar to the transmission mode. For a conductive MUT, such as aluminium, when the grounded boundary is close to the conductor, its potential drops significantly, and further reducing the capacitance measurements for the sensing elements it covers. The MUT results in valleys instead of peaks in the measurements, and thus it appears negative in the reconstructed image. When the grounded boundary is placed further away from the conductor, the potential of the conductor does not drop

very much. Therefore, the conductor also results in peaks in the measurements, and the reconstructed image is similar to the transmission mode.

The above observations indicate that the images obtained in the shunt mode depend not only on the property of the MUT, but also on the distance of the MUT to the grounded boundary. From Fig 5.1, it can be seen that by deriving the difference in images from the transmission mode and the shunt mode, conductive MUT can be identified. Material characterisation using this method has been used by Cheng (2008). However, this method is only applicable when the conductive MUT is placed close enough to the grounded boundary so that changes of different polarities in capacitance measurements can be detected. In other cases, where the conductivity is low or the MUT is far away from the grounded boundary, the difference in images from different sensing modes may not be obvious. Thus, it is difficult to characterise material property using capacitance measurements only.

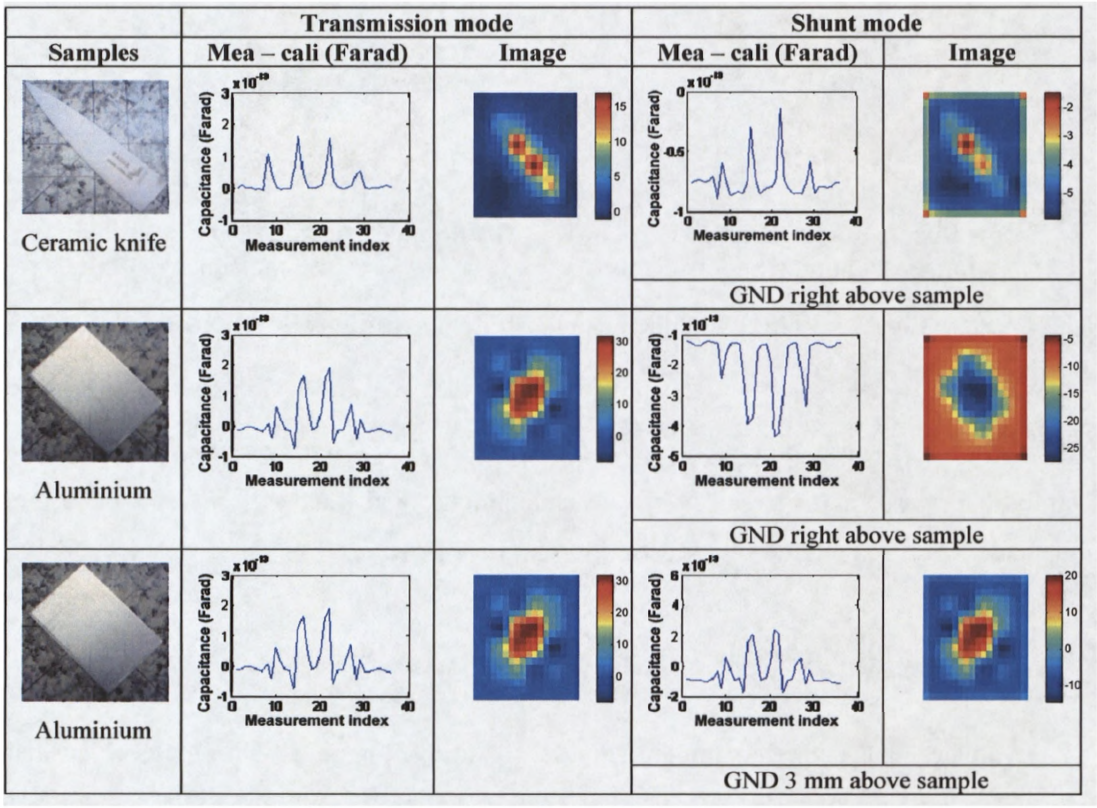

Fig. 5. 1 Imaging with ring sensor array in transmission mode and shunt mode

As discussed in Chapter 3, that the sensitivity distributions for the transmission mode and the shunt mode are different, the sensitivity coefficients derived from those distributions are different. Similar to the transmission mode, a set of coefficients for the shunt mode has been derived for the ring sensor. as given in Fig. 5.2 (b). It is of interest to examine the imaging results using different sensitivity coefficients for the same sample. Fig. 5.2 (c) and (d) show the reconstructed images using different set of coefficients. It can be seen that no significant improvement can be achieved. This is because the patterns of the sensitivity coefficients are the similar. In addition, pixel averaging reduces the influence of difference coefficients values.

0.212	0.414	0.212
0.414	1	0.414
0.212	0.414	0.212

(a) Sensitivity coefficients for transmission mode

0.185	1	0.185
1	0.694	1
0.185	1	0.185

(b) Sensitivity coefficients for shunt mode

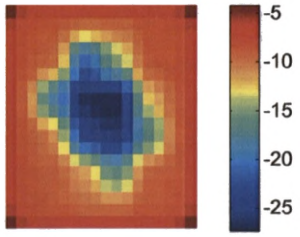

(c) Reconstructed image using transmission mode coefficients

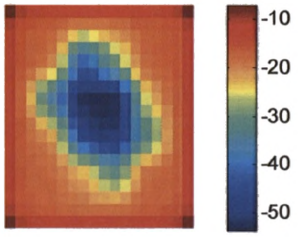

(d) Reconstructed image using shunt mode coefficients

Fig. 5.2 Images obtained using different sensitivity coefficients

For the above, it can be concluded that imaging with the transmission mode is more straight forward than imaging with the shunt mode, and thus will be used to further evaluate imaging with the ring sensor array in the following.

B. Imaging with single object

To evaluate edge detection for the ring sensor array, imaging with single object has been carried out. Samples of different shapes and properties are used, including a ceramic knife, a rectangular piece of Blu-Tack, a rectangular piece of aluminium and a steel knife. The test sample has been placed at different positions on the ring sensor

array. The samples are shown in the first row in Fig. 5.7. The reconstructed images are shown in the second row. The position and area errors are shown in the third row.
From the reconstructed images, it can be seen that that dielectric MUTs result in positive values in the images. The location, shape and orientation of dielectric MUTs can be successfully identified by the ring sensor array. For conductive MUTs, however, it is difficult to identify their shape and orientation, because artefacts of either positive or negative values are generated in images. Artefacts are significant especially when the conductive MUT is placed diagonally in the sensor array. This is because the conductor distorts the electric field and causes unwanted cross-talk when the row-excitation and column detection method is used. Further understanding of this phenomenon and image compensation method needs to be investigated in the future. For calculating position and area errors, artefacts are removed manually. In addition, a fixed threshold for C image has been used in area estimation. To ensure cross-reference in area estimation, the same threshold value is used in the rest of the chapter for C images. In addition, fixed thresholds for R and X images are also used.

In terms of position estimation, the position errors for the dielectric MUTs are less than 1 pixel, which is in the order of less than half of one sensing element. For conductive MUTs, the position error may be much bigger due to the artefacts in the image. In terms of area estimation, the area errors are not consistent, ranging between 55 % to -8 %. As an MUT contributes to every sensing element it covers, as discussed in Chapter 3, error in area estimation depends on the edge of the MUT relative to the sensing elements.

C. Imaging with multiple objects

Imaging with multiple objects was carried out to examine the spatial resolution for the ring sensor array. Mixtures of dielectrics and a mixture of dielectrics and conductor are used as test samples, including three small pieces of Blu-Tack placed at different positions with different spacing between them, two small pieces of Blu-Tack with ceramic knife or steel knife. The samples are shown in the first row in Fig. 5.8. The reconstructed images are shown in the second row. The position and area errors are given in the third row.

It can be seen from the images that when the dielectric MUTs are placed near each other, it is difficult to distinguish between them, as they will merge together as a big block. This is worse when the objects are covering multiple sensing elements. When the objects are placed with 1 element spacing apart, they could be identified individually from the images when placed in the centre of a sensing element, but not distinguishable in other cases. This means that the spatial resolution of ring array is about one sensing element at best.

For the mixture of the ceramic knife and the Blu-tack pieces, ceramic knife results in bigger values in the image, and the Blu-tack pieces result in small values, although it is much thicker than the ceramic knife. This is because the ring sensor has a small sensing depth, and thus, is sensitivity to the surface material property of the MUT. For mixture of steel knife and Blu-tack, the Blu-tack pieces cannot be seen at all due to the artefacts generated by the steel knife.

In terms of position estimation, the position error is less than 1 pixel for mixtures of dielectrics, but is 2.8 pixels for the mixture of dielectrics and conductor. In terms of area estimation, the errors are not consistent, with a worst case of 233.3% when Blu-tack pieces are placed with 1 element apart and on the corner of sensing elements.

From the above, the ring sensor array is suitable for imaging floating dielectric in the transmission mode. It has a spatial resolution of one sensing element, a position resolution is better than half of one sensing element. However, area estimation using the ring sensor array is not accurate, depending on the edges of the MUT relative to sensing elements.

5.2.2 Adaptive sensor array

This sub-section examines imaging with the adaptive array, including different scan methods and image reconstruction algorithms, including LBP and Lanweber iteration.

E. Normal scan and adaptive scan

To improve scanning efficiency for the adaptive array, an adaptive scan consisting of coarse scan and fine scan has been proposed in Chapter 3. To compare imaging results with normal tomography scan and adaptive scan, single object imaging with a 4×4 square-electrode sensor array using LBP was carried out. A rectangular piece of Blu-Tack and a ceramic knife were used as test samples, which were placed at different positions on the sensor array. Fig. 5.3 shows the reconstructed images obtained from the normal scan and adaptive scan.

The location, shape and orientation of the sample can be clearly identified from the images obtained from the normal scan. However, samples appear to be segmented in the images obtained from the adaptive scan. To understand the problem with the adaptive scan, the typical electric field and sensitivity distributions of a pair of electrodes in the adaptive array are examined (see Fig. 5.4).

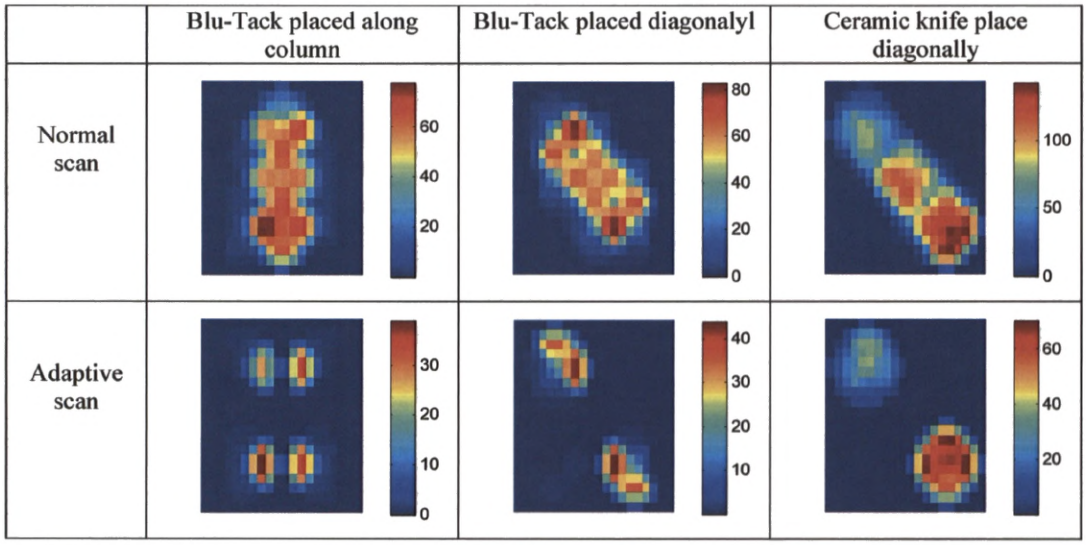

Fig. 5.3 Images obtained using normal and adaptive scans for adaptive array

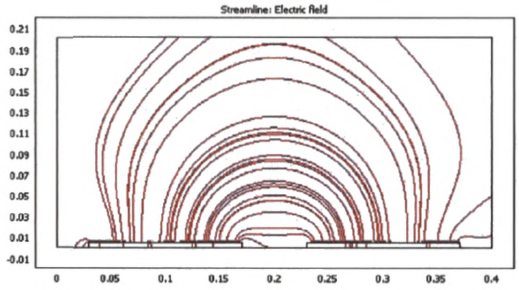

(a) Electric field distribution

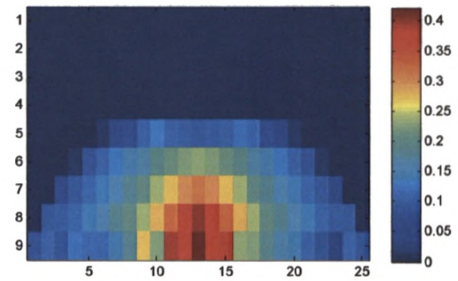

(b) Sensitivity distribution in XZ plane

Fig. 5.4 Electric field and sensitivity distributions for adjacent electrode pair in adaptive array

From Fig. 5.4, it can be seen that the electric field and the higher sensitivity values are mainly concentrated between the excitation and detection electrodes. The sensitivity values near the boundaries of the sensing space are very small or even equal to 0, forming dead regions. If a sensitivity matrix of such a feature is used in image reconstruction, most information in those dead regions in the sensing space will be lost in image reconstruction. This is a major problem when tomography is used with planar capacitive sensor array. For fine scan with a sub array of 2 × 2 electrodes, information near the edges of the 2×2 array is lost. As the final image for the adaptive scan is combined from 4 small images obtained from fine scans, an MUT may appear segmented in the final image.

From the above, it can be concluded that normal tomography scan is more suitable for the adaptive array. It will be used for single- and multiple-object imaging in the following.

F. Imaging with single object

Single-object imaging has been carried out to evaluate edge detection by the adaptive array. Test samples were the same as used for the ring array. The reconstructed images by LBP and Landweber iteration are shown in the fourth and sixth row respectively in Fig. 5.7. The respective position and area errors are given in the fifth and seventh row.

The location, shape and orientation of the samples can be clearly identified from the images using both algorithms. Unlike the ring sensor array, conductive object does not produce artefacts, and the values in the images are positive for both dielectric and conductive MUTs. Although this feature is good for imaging, it indicates that the adaptive sensor array cannot distinguish between dielectric and conductive objects.

In terms of the position estimation, the errors from LBP are less than 1.2 pixels while the errors from Landweber iteration are less than 2 pixels. This means that the adaptive

array has a position resolution better than half of one sensing elements. In terms of area estimation, both algorithms tend to underestimate the size of the MUT, as area errors are all negative. In addition, Landweber iteration tends to further underestimate the size and even distort the shape of the MUT, especially for conductive objects.

G. Imaging with multiple objects

To examine the spatial resolution, the same mixtures of samples as used for the ring array were used for multiple-object imaging with the adaptive array. The reconstructed images using LBP and Lanweber iteration are shown in the fourth and sixth row in Fig. 5.8. The respective position and area errors are given in the fifth and seventh row.

From the images, it can be seen that the adaptive array is able to distinguish the mixture of Blu-tack pieces in all cases. This means that the adaptive array has much better spatial resolution than the ring array. The mixture of Blu-Tack pieces can be better identified using Landweber iteration than using LBP, because iterative algorithm is more suitable for complex distributions (Li 2008). The drawbacks of adaptive array are that the shapes of the objects are distorted in many images, and the object boundaries are not smooth. Adaptive array can also better distinguish the mixture of ceramic and Blu-tack pieces. For the mixture of steel knife and Blu-Tack pieces, they can be distinguished using LBP. However, the Blu-Tack pieces can hardly be seen using Landweber iteration. This indicates that Landweber iteration is more suitable for multi-object imaging or mixtures with low contrast in permittivity. LBP is more suitable for mixtures with high contrast in permittivity.

In terms of position estimation, the errors for LBP are smaller than 2.2 pixels while the errors for Landweber are smaller than 1.8 pixels. Concluding from both single-object imaging and multi-object imaging, the adaptive array has a position resolution about half of one sensing element, which is similar to the ring array. In terms of area estimation, the errors are not consistent, and depend on the edges of MUT relative to sensing elements.

5.2.3 Single-electrode sensor array

This sub-section investigates imaging with the single-electrode sensor array. A plastic cover with copper sheets was used together with the sensor board to form the single-electrode array. The copper sheet on the bottom side of the cover is used as a big detection electrode, while the copper sheet on the top side is connected to shielding. Images are obtained by interpolation with sensitivity coefficients.

A. Normal scan and adaptive scan

As discussed in Chapter 3, the adaptive scan can also be used with the single-electrode array to improve scan efficiency. To compare the results using the normal scan and adaptive scan, single-object imaging using a rectangular piece of Blu-tack and a ceramic knife was carried out. Fig. 5.5 shows the reconstructed images obtained using different scan methods.

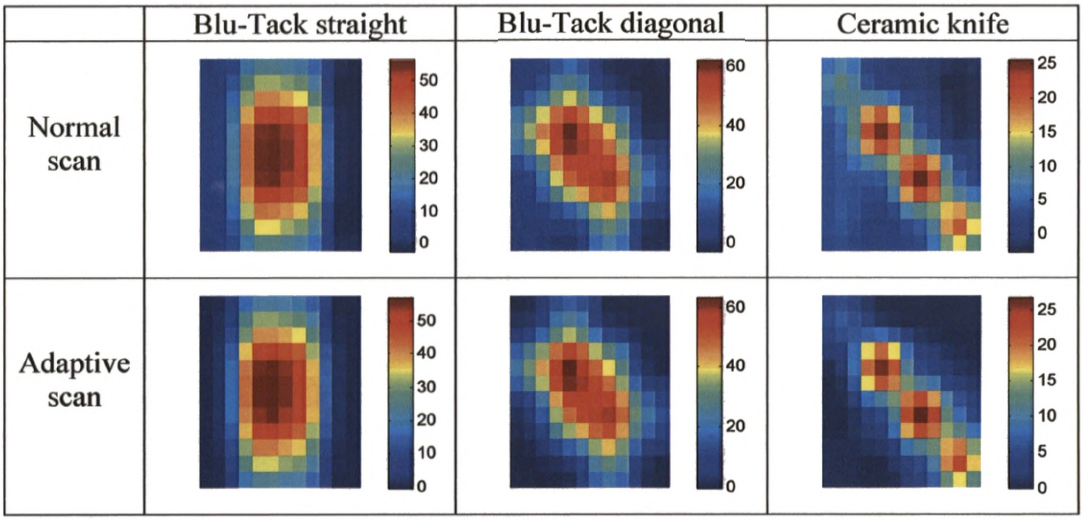

Fig. 5.5 Images obtained using normal and adaptive scans for single-electrode array

Unlike the adaptive array, the single-electrode array produces almost identical images from the adaptive scan and normal scan. To explain the feature of the single-electrode array, electric field and sensitivity distributions for a one-element single-electrode sensor are given in Fig. 5.6.

Due to the structure of single-electrode sensor, where the sensor electrode and the virtual electrode form a parallel capacitor, the electric field is almost uniformly distributed in the sensing space. The sensitivity distribution is therefore more uniform, with almost no dead region. This ensures the use of different measurement protocols produce comparable measurements, and thus comparable images.

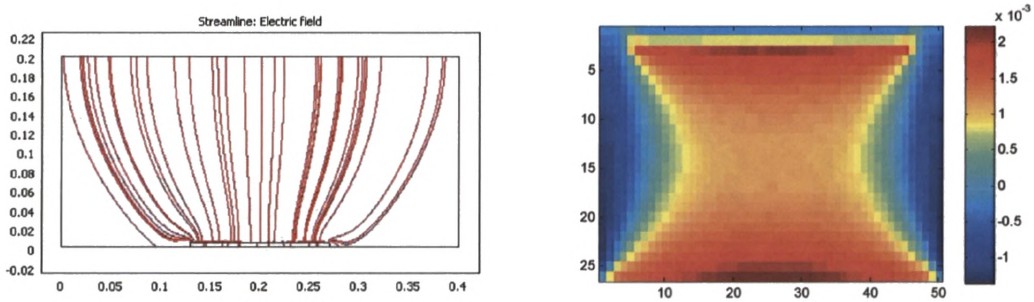

(a) Electric field distribution (b) Sensitivity distribution

Fig. 5.6 Electric field and sensitivity distributions for single-electrode sensor

From the above, it can be concluded that adaptive scan is better for the single-electrode array, because scan efficiency can be improved while maintaining image correctness. Adaptive scan will be used in single-object and multi-object imaging in the following.

B. Imaging with single object

Single-object imaging has been carried out using the same varieties of samples used for ring array. The reconstructed images are shown in the eighth row in Fig. 5.7. Their respective position and area errors are given in the last row.

It can be seen that the single-electrode array can also identify the location, shape and orientation of the sample. Unlike the ring array, both dielectric and conductive samples result in positive values in images. This is because the single-electrode can be modelled as a parallel capacitor, and both dielectric and conductor placed between the two electrodes give rise to positive changes in capacitance. This means that the single-electrode array cannot distinguish between dielectric and conductive objects. As opposed to the ring sensor array, conductive object does not produce artefacts, because the electric field distribution in the sensing space is more uniform than the ring sensor.

In terms of position estimation, the errors for the single-electrode array are similar to the ring array for single object imaging. For area estimation, the errors are not consistent, depending on the edges of an MUT relative the sensing elements.

C. Imaging with multiple objects

Multiple-object imaging has been carried out with the same mixtures of samples used for ring array. The reconstructed images are shown in the eighth row in Fig. 5.8. Their respective position and area errors are given in the last row.

It can be seen that the single-electrode array has similar performance as the ring sensor array in detecting multiple pieces of Blu-Tack. When the samples are placed adjacent to each other, they appear to be merged together as a big block. When placed at least one sensing element apart, they can be distinguished only when placed in the centre of sensing elements. The spatial resolution for the single-electrode array is also one sensing element at best.

However, images for Blu-Tack pieces with ceramic knife or steel knife are different from those obtained from the ring sensor array. Blu-Tack pieces have bigger values in the images and can be better identified by the single-electrode array and the ceramic knife has smaller values in the image. This is because the capacitance measurement from the single-electrode sensor depends on the overall contribution of an MUT to the parallel capacitor, including its properties and dimension. As the Blu-Tack pieces are much thicker than the ceramic knife, it results in bigger capacitance measurement. Furthermore, the steel knife does not produce artefacts in the image, which allows the Blu-Tack to be identified. These indicate that, for imaging with grounded MUT, the single-electrode array is better than the ring sensor array in the shunt mode.

In terms of position and area estimation, the single-electrode array has similar performance as the ring sensor array. This is because the two sensor arrays have the same elementary size and use the same image reconstruction method.

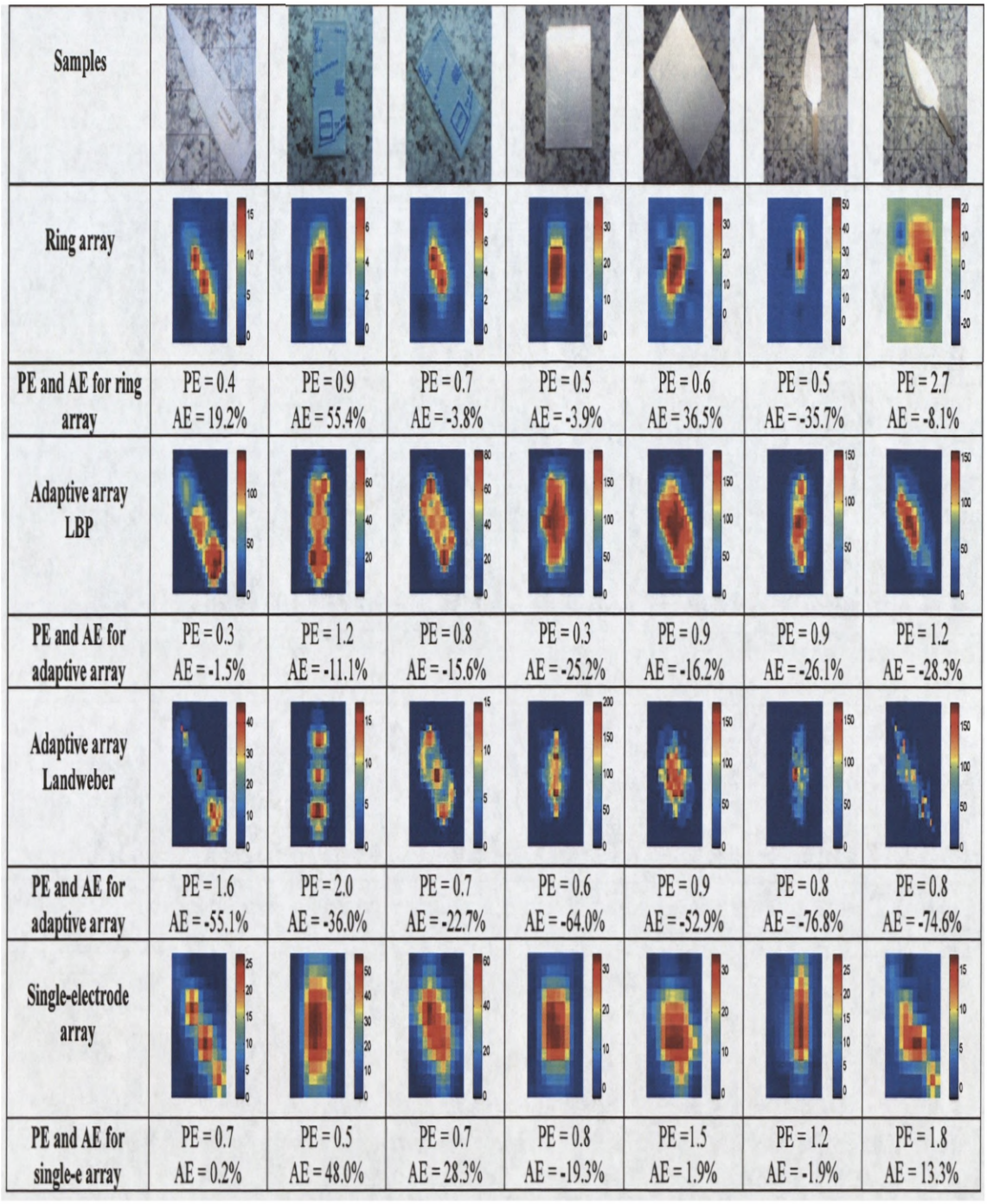

Fig. 5.7 Imaging single object with different capacitive sensor arrays and image reconstruction methods

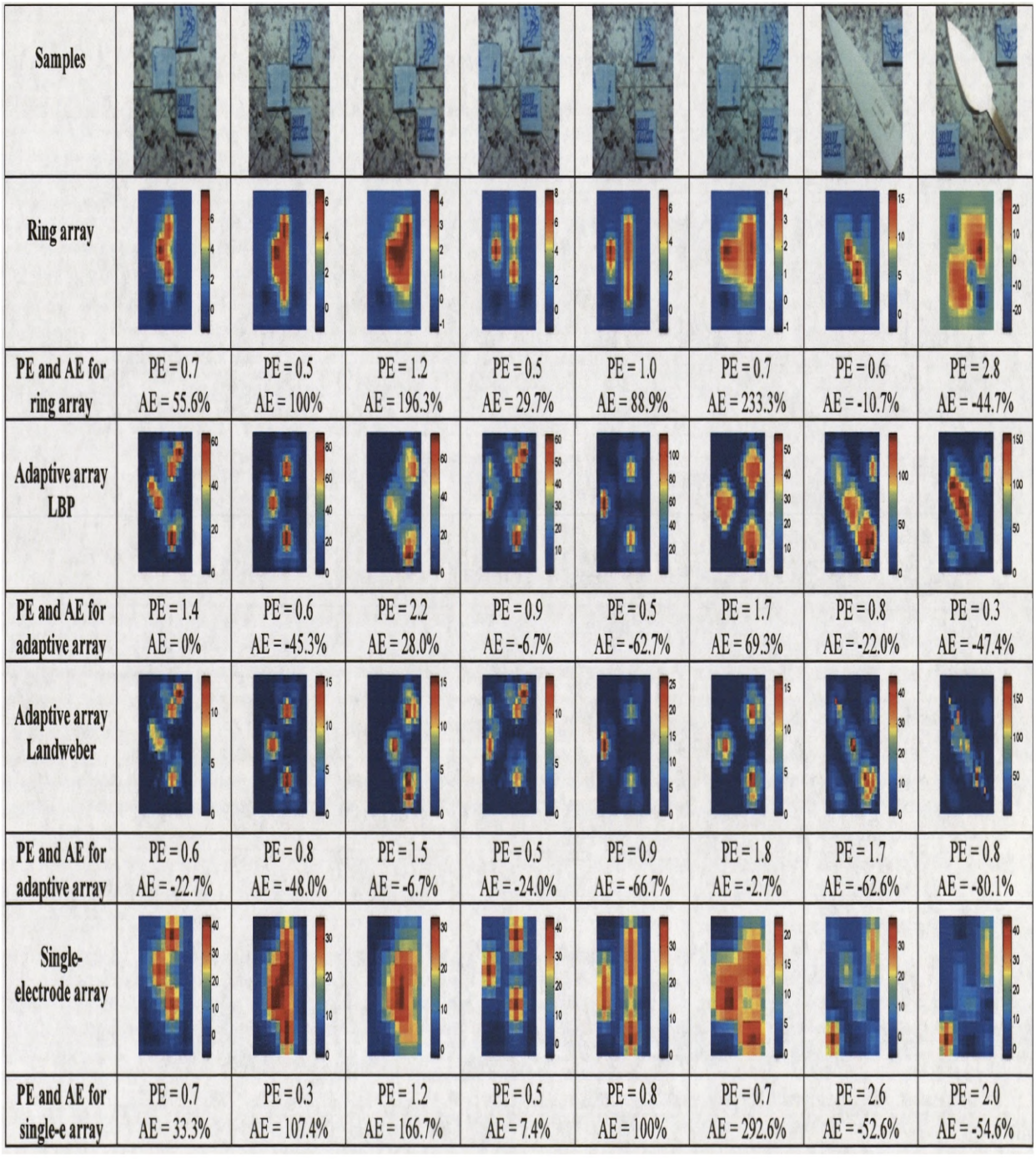

Fig. 5.8 Imaging multiple objects with different capacitive sensor arrays and image reconstruction methods

5.2.4 Comparing imaging results with different capacitive sensor arrays

Based on the imaging results, the features of the three capacitive sensor arrays are summarised in the following.

The ring sensor array is suitable for imaging floating MUTs in the transmission mode, especially for floating dielectrics. It has a spatial resolution of one sensing element, a position resolution of half a sensing element. Conductive MUT generates artefacts in the image and significantly degrade edge detection and position estimation. The ring sensor array is sensitivity to the surface property of an MUT due to small sensing depth. Imaging with the ring sensor array in the shunt mode is complicated, with imaging results depending not only on the properties of MUT, but also on its z position to the grounded boundary. Therefore, it is not recommended for imaging with grounded MUT.

The adaptive array works better with normal tomography scan than with the adaptive scan. As the sensitivity distribution of the planar sensor array has dead regions near the boundaries of the sensing space, adaptive scan may result in segmented MUT in the reconstructed image. The adaptive array cannot distinguish between dielectric and conductive objects. The spatial resolution and position resolution of adaptive array are both half a sensing element.

The single-electrode array works better with the adaptive scan than the normal scan, because the scan efficiency can be improved. It is different from the adaptive array because the structure of the single-electrode sensor ensures a much more uniform sensitivity distribution without dead region in the sensing space. The single-electrode array also cannot distinguish between dielectric and conductive objects. The measurement from single-electrode sensor depends on the overall contribution of an MUT to the parallel capacitor model. It has a spatial resolution of one sensing element, and a position resolution of half a sensing element. Single-electrode sensor array is more suitable for imaging grounded MUT.

Area estimation is not accurate for the three capacitive sensor arrays, all depending on the edges of MUT relative to sensing elements.

5.3 Imaging with PCB-coil array

This section investigates imaging with the PCB-coil array. Interpolation based on sensitivity coefficients is used for image reconstruction.

5.3.1 Imaging single object

To evaluate edge detection for the coil array, single-object imaging was carried out using samples of different shapes and properties, including a rectangular piece of aluminium (conductive but non-magnetic) and a pair of steel scissors (conductive and magnetic). Fig. 5.9 shows the reconstructed images and respective position and area errors.

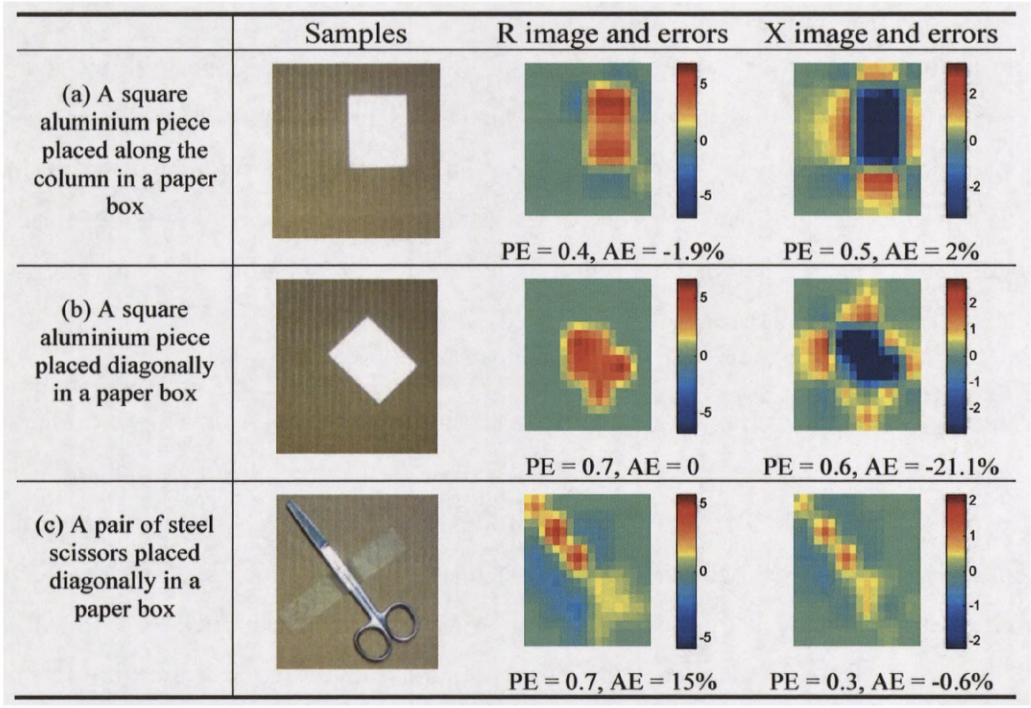

Fig. 5.9 Imaging single object with PCB-coil array

From the images, the shape, position and orientation of the samples can be clearly identified by the coil array. In addition, the imaginary part of the mutual inductance has different responses to conductivity and permeability, in that it decreases with

conductive but non-magnetic object, but increases with conductive and magnetic object. This means that the sensor array can be used to generate images of conductivity and permeability distributions at the same time. Due to the negative sensitivity surrounding the sensing elements as discussed in Chapter 3, artefacts with opposite values exist in R images, and are especially significant in X images. Further work is needed to compensate for the negative sensitivity. In the following, the artefacts are removed by applying image threshold before calculating the position and area errors.

From the position and area errors, the coil array has a position resolution better than 0.7 pixels, and an area error depending on the edges of MUT relative to sensing elements.

5.3.2 Imaging multiple objects

To evaluate the spatial resolution for the coil array, multiple-object imaging has been carried out using different mixtures of metallic objects, including square pieces of copper sheet, a mixture of copper sheet and a rectangular piece of aluminium, and a mixture of aluminium and steel knife. Fig. 5.10 shows the samples, the reconstructed images after removing the artefacts and the respective position and area errors.

Similar to the ring array, the coil array cannot distinguish multiple objects when they are placed adjacent to each other, as they will merge together in the image. When the objects are placed at least 1 sensing space apart, they can be easily distinguished. Metallic objects with different properties can also be distinguished from the image, as can be seen for the mixture of steel knife and aluminium. The errors in position estimation are below 1 pixel and the errors in area estimation are not consistent.

From the results from single-object and multiple-object imaging, the coil sensor array has a spatial resolution of one sensing element, a position resolution of half a sensing element. Area estimation is not accurate, depending on the edges of the objects relative to the sensing elements. Using the coil array, images of conductivity and permeability distributions can be generated simultaneously. In addition, the planar PCB-coil sensor array is compact and easy to extend the number of sensing elements.

	Samples	R image and errors	X image and errors
3 square pieces of copper sheets adjacent to each other, placed in centre of sensing elements	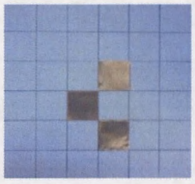	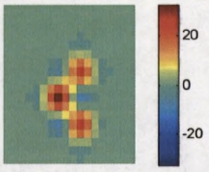 PE = 0.5 AE = 29.7%	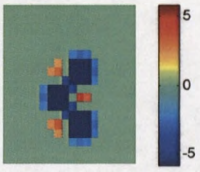 PE = 0.5 AE =7.4%
3 square pieces of copper sheets adjacent to each other, placed on corner of sensing elements	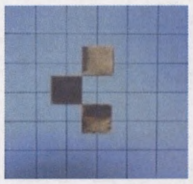	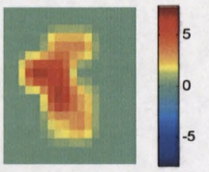 PE = 0.3 AE = 74.1%	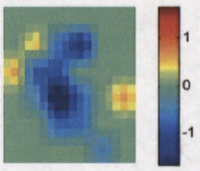 PE = 0.5 AE = 137%
3 square pieces of copper sheets one sensing element apart, in centre of sensing elements	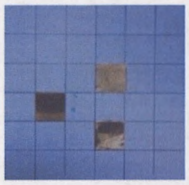	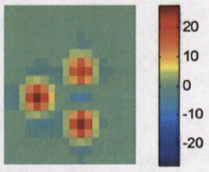 PE = 0.9 AE = 0%	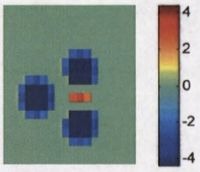 PE = 0.9 AE = 0%
3 square pieces of copper sheets one sensing element apart, on the corner of sensing elements	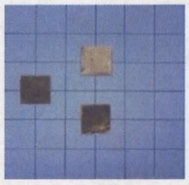	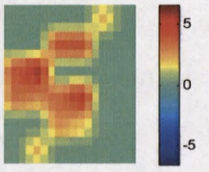 PE = 0.3 AE = 170%	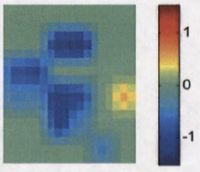 PE = 0.9 AE = 289%
2 pieces of square copper sheets and a piece of aluminium	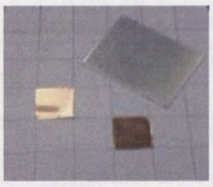	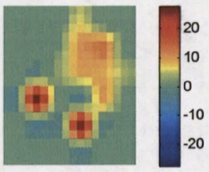 PE = 0.9 AE = -51.4%	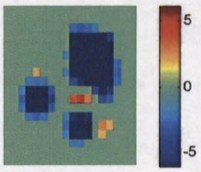 PE = 0.8 AE = -21.4%
A steel knife and a piece of aluminium		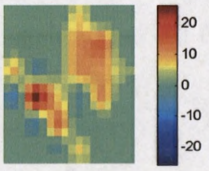 PE = 1.0 AE = -55.1%	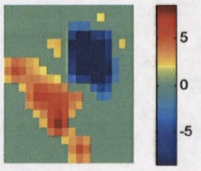 PE = 0.4 AE = 4%

Fig. 5.10 Imaging multiple objects with PCB-coil array

Imaging using interpolation based on sensitivity coefficients can deliver similar results to tomographic imaging, but requires much less computation and do not distort the shape of MUT. Imaging by interpolation based on sensitivity coefficients is a good alternative for imaging with planar sensors. To improve image fidelity, the issues with cross-talk and image errors due to object covering multiple sensing elements should be compensated as future work.

5.4 Imaging with dual-modality sensor array

In the previous sections, the performances of the single-modality sensor arrays have been evaluated in terms of edge detection, spatial resolution, position estimation and area estimation. As the dual-modality sensor array is assembled from the ring sensor array and the coil sensor array, the performance in terms of edge detection, spatial resolution and position resolution are the same as been used individually. In this section, evaluation of the dual-modality array will focus on material characterisation and fusion.

A. Imaging single object

To examine how the dual-modality sensor array can be used to distinguish MUTs, single-object imaging has been carried out using samples of different material properties and shapes, including a ceramic knife (dielectric only), a rectangular piece of aluminium (conductive only), a steel knife and a pair of scissors (conductive and permeable). To minimise artefacts in C images, the metallic objects are placed along the column one the array. The samples and the reconstructed images are shown in Fig. 5.11.

In Chapter 4, a lookup table has been established based on the relationships of C, R and X measurements and material properties. As C/R/X images have the same pixel number and sequence, the index of pixels can be cross referenced in C/R/X images. From Fig. 5.11, a dielectric MUT can be clearly identified in a C image in terms of its location, shape and orientation, but it does not appear in R and X images. Therefore, an index with a positive pixel value in the C image and zero in both R and X can be characterised as dielectric. For a metallic MUT, it appears in C, R and X images. However, the location, shape and orientation are more accurately reflected in R/X images than in the

C image. If an index has positive pixel values in both R and X images, it can be characterised as conductive. If an index has a positive pixel value in R and a negative pixel value in X image, it can be characterised as permeable. Thus, using the lookup table based fusion method, permittivity/conductivity/permeability images can be generated from C/R/X images.

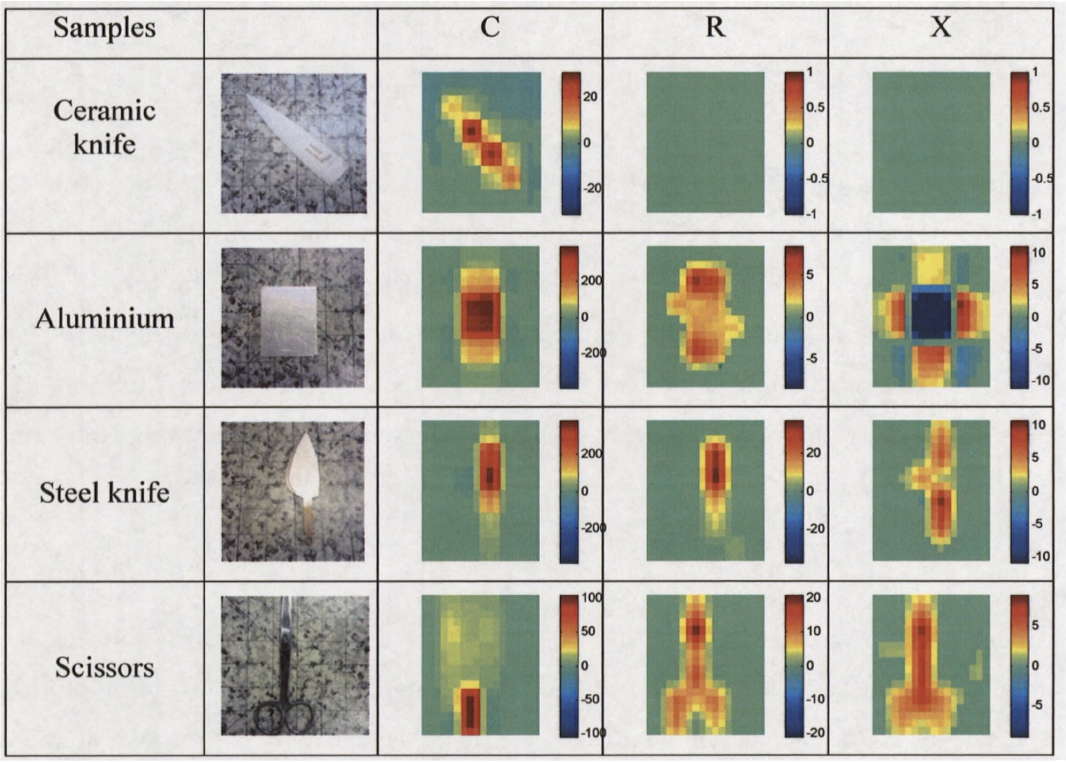

Fig. 5.11 Imaging single object with dual-modality sensor array

B. Imaging and fusion with multiple objects

To examine fusion with the dual-modality sensor array, multiple-object imaging has been carried out using different combinations of materials. The samples include a mixture of dielectrics (Blu-tack and ceramic knife), a mixture of dielectric and conductor (ceramic knife and steel knife), a mixture of conductive and permeable metallic objects (copper and steel knife), and a mixture of dielectric, conductive and permeable objects (Blu-tack, copper and steel knife). Fig. 5.12 shows the samples, reconstructed C/R/X images and the binary permittivity/conductivity/permeability images.

From the fusion results, it can be seen that the location, shape and orientation of different materials can be clearly identified. Unlike single-modality sensor arrays, the dual-modality array can provide complementary information for the MUT. Based on the response features of capacitive and coil sensors, the effect of conductivity can be decoupled from the capacitance measurements. Therefore, the interpretation of the information is more accurate.

However, small artefacts exist in the permittivity image. This is due to the use of the ring sensor array. As conductive object may generate large artefacts with positive values in the C image, this positive pixels will lead to artefacts in the permittivity image. Image compensation may need to be investigated to remove the artefacts before fusion is carried out. Another method is to use the single-electrode sensor array, which does not have problems with artefact generated from metallic objects. As the single-electrode array requires the MUT to be grounded, a dual-modality sensor based on the single-electrode array and coil array may be more suitable for security shoe scanner, which is of interest to be investigated in the future.

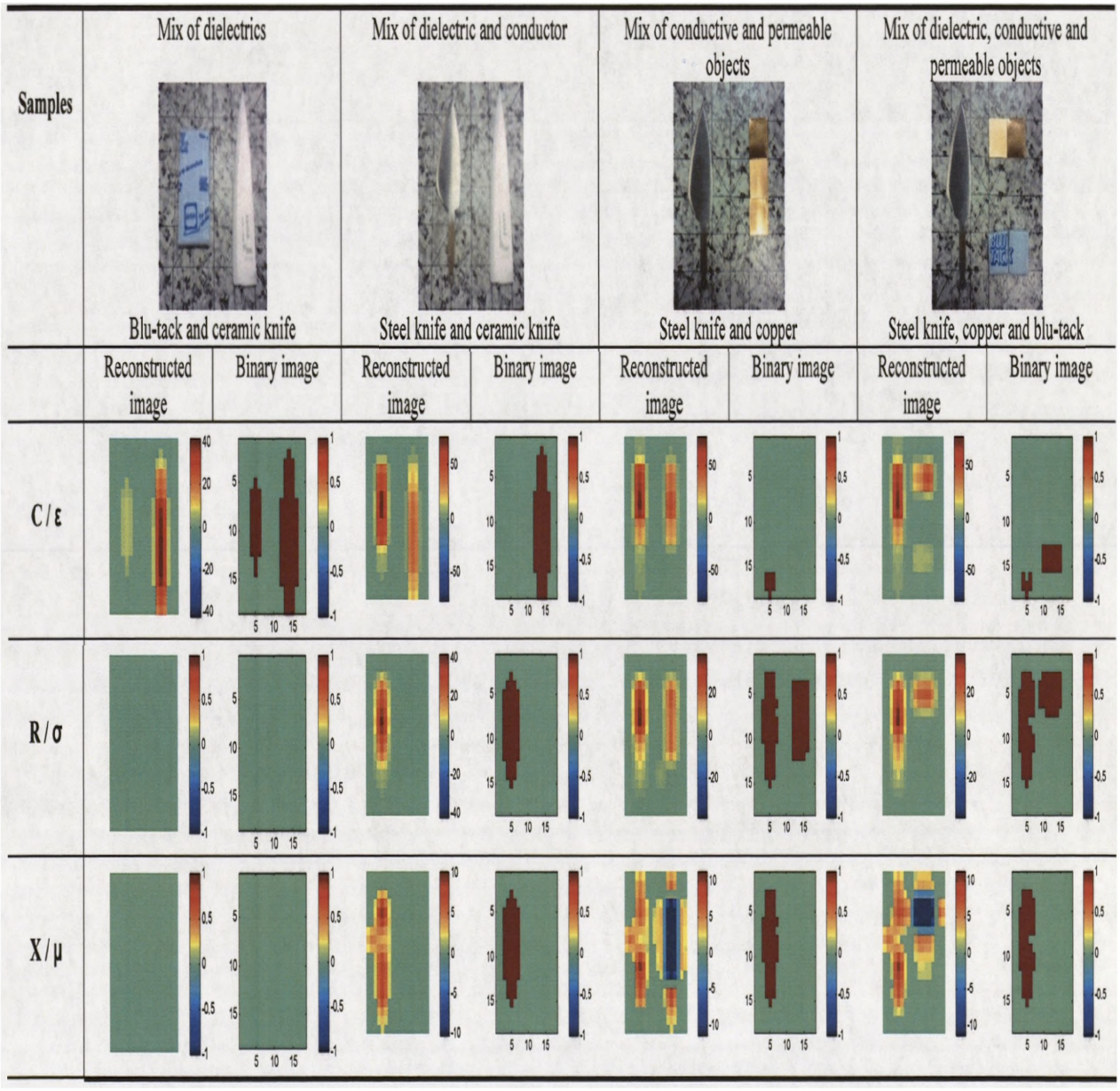

Fig. 5.12 Imaging and fusion of multiple objects with dual-modality sensor arrays

5.5 Summary

In this chapter, imaging with different sensor arrays has been evaluated in terms of edge detection, spatial resolution, position and area estimation. The ring sensor array in the transmission mode is good in imaging floating MUTs, especially for floating dielectrics. It has a spatial resolution of one sensing element, a position resolution of half a sensing element. Conductive MUT will generate artefacts and significantly influence edge detection and position estimation. As imaging with the ring sensor array in the shunt mode is complicated, it is not recommended for imaging with grounded MUT. The adaptive array works better with normal tomography scan than with adaptive scan, because the dead region in sensitivity distribution results in segmented MUT in the reconstructed image. It has a spatial resolution and a position resolution of half a sensing element. The single-electrode array works better with the adaptive scan because the structure of the single-electrode sensor ensures uniform sensitivity distribution without dead region in the sensing space. It has a spatial resolution of one sensing element, and a position resolution of half a sensing element. Single-electrode sensor array is more suitable for imaging grounded MUT. The coil sensor array can generate conductivity/permeability simultaneously, and has a spatial resolution of one sensing element, a position resolution of half a sensing element.

Imaging using interpolation based on sensitivity coefficients can deliver similar results to tomography imaging, but requires much less computation and do not distort the shape of MUT. Imaging by interpolation based on sensitivity coefficients is a good alternative for imaging with planar sensors.

Using a lookup table based fusion method, permittivity/conductivity/permeability images can be generated from C/R/X images, which are able to clearly identify the location, shape and orientation of different materials. A dual-modality sensor array based on the single-electrode array and the coil array maybe more suitable for scanning shoes.

Chapter 6 Conclusions and future work

This chapter concludes the major findings from this research and gives suggestions for future work.

6.1 Conclusions

To provide an alternative security screening method for checking shoes, envelopes and small parcels, investigations of imaging by capacitive and coil sensor arrays were carried out in sensor designs, development of imaging system, image reconstruction and fusion, and evaluation of imaging results.

Planar sensors can provide one-sided access to a MUT, which makes it suitable for scanning shoes. However, the planar structure complicates sensor response features and design issues. According to the potential boundary conditions of an MUT, a planar capacitive sensor can be described using one of the three different sensing modes: (1) the transmission mode, (2) the shunt mode and (3) the single-electrode mode. To achieve an optimal design, a trade-off between different evaluation parameters has to be made. The uniformity and the depth of sensitivity distribution of the sensor depend largely on the geometry of the electrodes. In addition, conductivity would cause positive changes for a planar capacitive sensor in the transmission and the single-electrode modes, but negative changes in the shunt mode. Planar PCB-coil sensors have the advantages of high sensitive, small lift-off and compact in size, which need to be further exploited imaging applications. It is of interest to investigate imaging with planar capacitive and coil sensor arrays using different sensing modes and image reconstruction methods. The use of a dual-modality capacitive and coil sensor array is of particular interest, because it can provide complementary information for an MUT.

The optimal designs of the single-modality and dual-modality sensor arrays have been carried out with the same elementary size of 2×2 cm^2. The single-modality sensor arrays include a centric-ring-based capacitive array, a square-electrode-based adaptive capacitive array, a square-electrode-based single-electrode capacitive array and a PCB-

coil array. The dual-modality sensor array is assembled using the ring array and the PCB-coil array. The sensing depths for the single-modality sensor arrays are generally between 10 – 14 mm, except for the ring array, which is 6 mm against lift-off and 3 mm against thickness of MUT. The dual-modality sensor array has a smaller sensing depth due to the presence of additional sensor board. An adaptive measurement protocol based on coarse scan and fine scan can be used with the adaptive array and the single-electrode array. This measurement method can significantly improve acquisition time and imaging efficiency when the number of electrodes in the sensor array is large.

Cross-talk has different influences on different sensor arrays. For the ring array, single electrode array, PCB-coil array and dual-modality array, a sample contributes to every sensing element it covers. This error is biggest when a sample is placed on the corner of a sensing element. For the adaptive array, the sample appears bigger when placed in the centre and on the corner, but smaller when placed on the edge.

To address the challenges in interfacing to different single-modality and multi-modality sensor arrays, a novel multi-channel multi-modality system based on an impedance analyser HP4192A has been developed. Flexibility in sensor connection is achieved by using a specifically designed MUX box to extend the number of measurement channels, and to support the measurement using the 4TP configuration and the mutual inductance configuration. The system software is developed using a layered-structure, with a DLL to manage low-level communications and a Matlab-based GUI to control data acquisition, image reconstruction and post-analysis.

The performance of the HP4192A-based system has been evaluated. The resolutions for C and G measurements are 0.1 fF and 1 nS respectively. The noise level for C and G measurements in the frequency range of 100 kHz – 2 MHz is less than 1 fF, and less than 10 nS respectively. At below 2 MHz, the drift for C in one day is less than 10 fF and less than 10 nS for G. The resolution for R/X measurements is 0.1 mΩ, the noise level for R/X is less than 2.5 mΩ and drift in one day for R/X is less than 7 mΩ. The system is further analysed with the consideration of parasitic components in the MUX box and coaxial cables. It shows that parasitic components may lead to negative measurements and results in measurements uncertainty at higher frequencies. For the

current design, the working frequency for the 4TP configuration should be below 5 MHz, and the working frequency for the mutual inductance configuration should be below 500 kHz. The HP4192A-based system has better performance in most aspects, except for data acquisition rate, which is lower than the AC-ECT system, and resolution, which is lower than 1260A. Although this system cannot be directly used to take measurements from the single-electrode capacitive sensor array, a big electrode made from a plastic cover is used as the virtual terminal, so that the single-electrode sensor array can be measured by HP4192A-based system.

Image reconstruction and fusion for capacitive and coil sensors have been considered. Compared with model-based imaging, tomography has more general applicability and can be used for different sensors. LBP and Landweber iteration, which are representative image reconstruction algorithms used in tomography, are used with the capacitive adaptive sensor array. The sensitivity-coefficients-based interpolation method can generate images with higher resolutions than direct imaging, and thus is used with the other sensor arrays. Based on the features of C, R and X measurements to different materials, a lookup table based pixel level fusion is used with the dual-modality sensor array.

Imaging with the single-modality and dual-modality sensor arrays has been evaluated. The ring sensor array is suitable for imaging floating MUTs in the transmission mode. It has a spatial resolution of one sensing element and a position resolution of half a sensing element. Conductive MUT may generate artefacts in image and significantly degrade edge detection and position estimation. The ring sensor array is sensitivity to the surface property of an MUT. Imaging with the ring sensor array in the shunt mode is complicated, with imaging results depending not only on the properties of MUT, but also on its z position to the grounded boundary. Therefore, it is not recommended for imaging with grounded MUT. The adaptive array works better with normal tomography scan than with adaptive scan. The adaptive array cannot distinguish between dielectric and conductive objects. The spatial resolution and position resolution are both half a sensing element. The single-electrode array works better with the adaptive scan than the normal scan, and is more suitable for imaging grounded MUT. However, it cannot distinguish between dielectric and conductive objects. The measurement from single-

electrode sensor depends on the overall contribution of an MUT to the parallel capacitor model. It has a spatial resolution of one sensing element, and a position resolution of half a sensing element. The coil array has a spatial resolution of one sensing element, a position resolution of half a sensing element. Area estimation is not accurate for all the sensor arrays, with area error depending on the edges of MUT relative to sensing elements.

Imaging by interpolation based on sensitivity coefficients can deliver similar results to tomographic imaging, but requires much less computation and does not distort the shape of MUT. It can be a good alternative for imaging with planar sensors.

The dual-modality array can provide complementary measurements, so that the effect of conductivity can be decoupled from the capacitance measurements. By the lookup table based fusion, permittivity/conductivity/permeability images can be generated from C/R/X images, which is a more accurate representation of material property distribution.

6.2 Future work

To improve imaging with the single-modality and dual-modality sensor arrays, future research work can be carried out in a number of aspects.

A common problem with imaging using the sensitivity coefficients based interpolation method is that an object will contribute to every sensing element it covers, and thus results in image error which depends on the position of the object relative to the sensing elements. A compensate method needs to be investigated to deal with such error, so that edge detection and spatial resolution can be improved.

A problem with PCB-coil array is that negative sensitivity values exist around the sensing element, and significantly increase cross-talk. A compensation method needs to be sought to deal with the cross-talk resulting from the negative sensitivity values. It has also been observed that the sensitivity values within the overlapped region are positive. Therefore, to eliminate the influence of negative sensitivity values, a sensor array with a

big excitation coil and multiple sensing coils may be used. The sensitivity distribution for such a configuration needs to be investigated.

To reduce the influence of the parasitic components in the system, an improved design with wider spacing for the reed relay switches and careful shielding along the signal path is needed for the MUX box. The length of the signal path also needs to be minimised.

For the dual-modality sensor array, the capacitive sensor array and coil sensor array can be implemented in multi-layered PCB, so that the sensor is more compact and less susceptible to relative movement of the sensor boards. In addition, gradiometer of differential windings for the pickup coil can be implemented using multiple PCB to improve the sensitivity in R/X measurements.

As the single-electrode array is more suitable for imaging grounded MUTs, it may be better to combine the single-electrode array and the coil array to form the dual-modality array for scanning shoes.

References

[1] Agilent Technologies (1998), LCR / Impedance measurement basics, application note, available at http://www.home.agilent.com/upload/cmc_upload/All/E206COMPTEST_LCR.pdf

[2] Agilent Technologies (2000), New technologies for accurate impedance measurement, Agilent PN 4294A

[3] Agilent Technologies (2006), Impedance measurement handbook

[4] Agilent Technologies (2008 1), Data sheet for Agilent 4294A precision impedance analyser, available at http://www.home.agilent.com/agilent/product.jspx?pn=4294A&NEWCCLC=USeng

[5] Agilent Technologies (2008 2), New technologies for accurate impedance measurement (40 Hz to 110MHz), Produce note 4294A, available at http://cp.literature.agilent.com/litweb/pdf/5968-4506E.pdf

[6] Analog Devices (2009) Capacitance-to-Digital Converter Overview, available at http://www.analog.com/en/analog-to-digital-converters/capacitance-to-digital-converters/products/overview/CU_over_CDC_Technology/resources/fca.html

[7] Basarab-Horwath I, Daniels A T and Green R G (2001), Image analysis in dual modality tomography for material classification, *Meas. Sci. Technol.*, 12, pp 1153-1156

[8] Beck M S and Williams R A (1996), Process tomography: a European innovation and its applications, *Meas. Sci. & Technol.*, 7, pp 215-224, 1996

[9] Benitez D S, Quek S and Gaydecki P (2007), Efficient image enhancement algorithm for images of steel reinforcing bars in concrete obtained by a new solid-state sensor-based system, *IET Sci. Meas. Technol.*, 1 (5), pp 255-260

[10] Blitz J (1991), Electrical and magnetic methods of non-destructive testing, IOP publishing, Adam Hilger, New York, 1991

[11] Brown B H (2001), Medical impedance tomography and process impedance tomography: a brief review, *Meas. Sci. & Technol.*, 12, pp 991-996

[12] Bruschini C (2000), Metal detectors in civil engineering and humanitarian de-mining: overview and tests of a commercial visualising system, *Insight*, 42, pp 89-97

[13] Buffler A (2004), Contraband detection with fast neutrons, *Radiat. Phys. Chem.*, 71, pp. 853–861

[14] Burke S K and Ditchburn R J (2008), Mutual impedance of planar eddy-current driver-pickup spiral coils, *Research in Nondestructive Evaluation*, 19 (1), pp 1-19

[15] Burke S K and Ibrahim M E (2004), Mutual impedance of air-cored coils above a conducting plate, *J Phys. D: Appl. Phys.*, 37, pp 1857-1868

[16] Cawley P (2001),"Non-destructive testing - current capabilities and future directions, *Proc. Inst. Mech. Eng.*, 215, pp 213–223

[17] Centre for Protection of National infrastructure (2009), An introduction to screening mail and deliveries, available at http://www.cpni.gov.uk/WhatsNew/postrooms.aspx#02

[18] Chen Z C and Luo R C (1998), Design and implementation of capacitive proximity sensor using microelectromechanical systems technology, IEEE Trans. Ind. Electron., 45, pp 886-894

[19] Cheng B (2008), Security imaging devices with planar capacitance sensor arrays, PhD thesis, The University of Manchester, UK

[20] Chondronasios A, Yang W Q and Nguyen V T (2001), Impedance analyser based tomography system, *2nd World Congress on Industrial Process Tomography*, Hannover, Germany, 29-31 August, pp 573-579

[21] COMSOL (2008), AC/DC module user guide

[22] Cypress Semiconductor (2007), Capacitive sensing techniques and considerations, available at http://www.cypress.com/?rID=3569

[23] Cypress Semiconductor (2008), CapSense device and method selection guide, AN14459, available at http://www.cypress.com/?rID=2890

[24] Da Silva M (2008), Impedance sensors for fast multiphase flow measurement and imaging, PhD thesis, Technical University of Dresden, Germany

[25] Diamond G G and Hutchins D A (2006), A new capacitive imaging technique for NDT, *9th European Conference on NDT*, Berlin, Germany, Sept. 25-29, poster 229, pp 1-8

[26] Ditchburn R J and Burke S K (2005), Planar rectangular spiral coils in eddy-current non-destructive inspection, *NDT&E International*, 38, pp 690-700

[27] Ditchburn R J, Burke S K and Posada M (2003), Eddy-current non-destructive inspection with thin spiral coils: long cracks in steel, *J. Nondestructive Evaluation*, 22 (2), pp 63-77

[28] Dodd C V and Deeds W E (1968), Analytical solutions to eddy-current probe-coil problems, *J. Appl. Phys.*, 39, pp 2829-2838

[29] Federici J F, Schulkin B, Huang F, Gary D, Barat R, Oliveira F and Zimdars D (2005), THz imaging and sensing for security applications – explosives, weapons and drugs, *Semicond. Sci. Technol.*, 20, pp 266-280

[30] Ferguson B and Zhang X C (2002), Materials for terahertz science and technology, Nature Materials, 1 (1), pp 26-33

[31] Fisher J, Goldfine N and Zilberstein V (2000), Cold work quality assessment and fatigue characterisation using conformable MWM^{TM} eddy-current sensors, *49th Defense Working Group on NDT*, Biloxi, MS, USA, Oct. 31–Nov. 2

[32] Franco S (2002), Design with operational amplifiers and analog integrated circuits, 3rd Edition, McGraw-Hill Higher Education

[33] Freescale Semiconductor (2006 1), Electric field imaging device, MC34940 datasheet, available at www.freescale.com/files/sensors/doc/data_sheet/MC34940.pdf

[34] Freescale Semiconductor (2006 2), Touch panel application using MC34940/MC33794 ICs, AN1985, available at www.freescale.com/files/sensors/doc/app_note/AN1985.pdf

[35] Frounchi J and Dehkhoda F (2003), High-speed capacitance scanner, Proc. of 3rd World Congress on Industrial Process Tomography, 2-5 Sept., Banff, Canada, pp 846-852

[36] Gatzen H H, Andreeva E and Iswahjudi H (2002), Eddy-current micro sensor based on thin-film technology, *IEEE Trans. on Magnetics*, 38 (5), pp 3368-3370

[37] Goldfine, N J Schlicker D E, Zahn M and Ryan W D (2000), Magnetometer with waveform shaping, U.S. Patent Number: 6,144,206

[38] Goldfine N, Schlicker D, Sheiretov Y, Washabaugh A and Zilberstein V (2001), Conformable eddy-current sensors and arrays for fleet-wide gas turbine

component quality assessment, *ASME Turbo Expo Land, Sea & Air*, New Orleans, USA, June 4-7

[39] Gonzalez-Nakazawa A (2007), A security scanner using magnetic sensors and tomography, PhD Thesis, The University of Manchester, UK

[40] Gonzalez-Nakazawa A, Gamio J C and Yang W Q (2005), Transient processes and noise in a tomography system: an analytical case study, *IEEE Sensors J.*, 5 (2), pp 321-329

[41] Gozani T (1997), Inspection techniques based on neutron interrogation, Proc. SPIE, 2936, pp 9-20

[42] Gozani T, Elsalim M, Ingle M and Philips E (2003), Gamma ray spectroscopy features for detection of small explosives, *Nucl. Instrum. Methods Phys. Res. A,* 505, pp 482-485

[43] Griffiths H (2001), Magnetic induction tomography, *Meas. Sci. Technol.*, 12, pp 1126-1131

[44] Hirota T, Siraiwa T, Hiramoto K and Ishihara M (1993), Development of micro-coil sensor for measuring magnetic field leakage, *Jpn. J. Appl. Phys.*, 32, pp 3328-3329

[45] HP (1987), HP4192A LF impedance analyser operation and service manual

[46] Hu X H, Katsouros M, Yang W Q and Huang S M (2007), Further analysis of charge/discharge capacitance measuring circuit used with tomography sensors, Sensors & Transducers Journal, 80 (6), pp 1246-1256

[47] Huang S M, Green R G, Plaskowski A B and Beck M S (1988 1), Conductivity effects on capacitance measurements of two-component fluids using the charge transfer method, *J. Phys. E: Sci. Instrum.*, 21, pp 539-548

[48] Huang S M, Plaskowski A B, Xie C G and Beck M S (1989), Tomographic imaging of two-component flow using capacitance sensors, J. Phys. E: Sci. Instrum., 22, pp 173–177

[49] Huang S M, Stott A L, Green R G and Beck M S (1988 2), Electronic transducers for industrial measurement of low value capacitances, J. Phys. E: Sci. Instrum., 21, pp242-250

[50] Huang S M, Xie C G, Thorn, R, Snowden D and Beck M S (1992), Design of sensor electronics for electrical capacitance tomography, *IEE Proc. G*, 139, pp 83-99

[51] Hoyle B S, Jia X, Podd F J, Schlaberg H I, Tan H S, Wang M, West R M, Williams R A and York T A (2001), Design and application of a multi-modal process tomography system, *Meas. Sci. Technol.*, 12, pp 1157-1165

[52] Igreja R and Dias C J (2004), Analytical evaluation of the interdigital electrodes capacitance for a multi-layered structure, Sens. and Actuators A: Phys., 112, pp 291-301

[53] Kong S G, Heo J, Abidi B R, Paik J and Abidi M A (2004), Recent advances in visual and infrared face recognition – a review, Computer Vision Image Understanding, 97 (1), pp103-135

[54] Lee J W, Min D J, Kim J and Kim W (1999), A 600-dpi capacitive fingerprint sensor chip and image-synthesis technique, IEEE J. of Solid-State Circuits, 34, pp 469-475

[55] Li X B, Larson S D, Zyuzin A S and Mamishev A V (2006), Design principles for multichannel fringing electric field sensors, IEEE Sensors J., 6, pp 434-440

[56] Li Y (2008), Key issues of 2D/3D image reconstruction in electrical tomography, PhD thesis, The University of Manchester , UK

[57] Mameshev A V, Lesieutre B C and Zahn M (1998), Optimization of multi-wavelength interdigital dielectrometry instrumentation and algorithms, *IEEE Trans. Dielect. Elect. Insulation*, 5 (3), pp 408–420

[58] Mamishev A V, Sundara-Rajan K, Yang F, Du Y and Zahn M (2004), Interdigital sensors and transducers, Proc. of IEEE, 92, pp 808-845

[59] Marsh D (2006), Capacitive touch sensors gain fans, available at http://www.edn.com/article/CA6343249.html

[60] Merkel T, Pagel L and Glock H W (2000), Electric fields in fluidic channels and sensor applications with capacitance, Sens. and Actuators A: Phys., 80, pp 1-7

[61] Miller G, Gaydecki P, Quek S, Fernandes B and Zaid M (2005), A combined Q and heterodyne sensor incorporating real-time DSP for reinforcement imaging, corrosion detection and material characterisation, *Sensors and Actuators A: Physical*, 121 (20), pp 339-346

[62] Moore D S (2004), Instrumentation for trace detection of high explosives, *Rev. Sci. Instrum.*, 75 (8), pp 2499-2512

[63] Mukhopadhyay S C, Gooneratne C P, Gupta G S and Yamada S (2005), Characterization and comparative evaluation of novel planar electromagnetic sensors, IEEE Trans. on Magnetics, 41 (10), pp 3658-3660

[64] Mukhopadhyay S C, Yamada S, Iwahara M (2002), Experimental determination of optimum coil pitch for a planar mesh-type micromagnetic sensor, IEEE Trans. on Magnetics, 38 (5), pp 3380-82

[65] Murray N C, Lacey R J, Mason P H (1997), Exploitation of X-ray technology for the detection of contraband-aviation security applications, *IEE European Conference on Security and Detection*, London, UK, April 28-30, pp. 13–18

[66] Nahvi M and Hoyle (2008), Wideband electrical impedance tomography, *Meas. Sci. Technol.*, 19, pp 1-9

[67] Nahvi M and Hoyle (2009), Data fusion for electrical spectro-tomography, IEEE International workshop on Imaging systems and Techniques, Shenzhen, China, May 11-12, pp 229-234

[68] NDT resource centre (2009), http://www.ndt-ed.org/EducationResources/CommunityCollege/EddyCurrents/cc_ec_index.htm

[69] Nerino R, Sosso A and Bartolo Picotto G (1997), A novel ac current source for capacitance-based displacement measurement, *IEEE Trans. Instrum. Meas.*, 46 (2), pp 640-643

[70] O'Dowd J, Callanan A, Banarie G and Company-Bosch E (2005), Capacitive sensor interfacing using sigma-delta techniques, Proceeding IEEE Sensors, Oct. 30 2005-Nov. 3, Irvine, California

[71] Okawa Y, Norimatsu H, Suto H and Takayanagi M (2003), The negative capacitance effect on the C-V measurement of Ultra thin gate dielectrics induced by the stray capacitance of the measurement system, *Proc. Int. Conf. Microelectronic Test Structures*, 17-20 March, Monterey, California, USA, pp. 197–202

[72] Peyton A J, Yu Z Z, Lyon G, Al-Zeibak S, Ferreira J, Velez J, Linhares F Borges A R, Xiong H L Saunders N H and Beck M S (1996), An overview of electromagnetic inductance tomography: description of three different systems, *Meas. Sci. Technol.*, 7, pp 261-271

[73] Qiu C, Hoyle B S and Podd F J W (2007), Engineering and application of a dual-modality process tomography system, *Flow Meas. Instrum.*, 18, pp 247-254

[74] Quantum Research Group (2005), Secrets of a successful QTouch™ design, Quantum research application note AN-KD02, Rev. 1.03, Oct. 2005

[75] Quantum Research Group (2009), Technology overview, available at http://www.qprox.com/technologies/qtouch.html

[76] Rapidscan Systems (2009), Metal detectors, available at http://www.rapiscansystems.com/metaldetection.html

[77] Ross A S, Saulnier G J, Newell J C and Isaacson D (2003), Current source design for electrical impedance tomography, *Physiol. Meas.*, 24, pp 509-516

[78] Sadler D J and Ahn C H (2001), On-chip eddy current sensor for proximity sensing and crack detection, *Sensors and Actuators A*, 91, pp 340-345

[79] Schlicker D E (2006), Imaging of Absolute electrical properties using electroquasitatic and magnetoquasistatic sensor arrasy, PhD Thesis, Massachusetts Institute of Technology

[80] Schliker D, Washabaugh A, Shay I and Goldfine N (2004), Inductive and capacitive array imaging of buried objects, 16th World Conference on Nondestructive Testing, Montreal, Canada, August 30 – Sept. 3

[81] Sears J (2003), Interdigital dielectrometry based detection and identification of dangerous materials for security applications, MSc Thesis, Massachusetts Institute of Technology

[82] Sensatech (2000), Foot Gauge, available at http://www.sensatech.com/Applications/retail.html

[83] Seward D C and Yukl T (1991), Explosive detection using dielectrometry, *Proc. First Int. Symposium on Explosive Detection Technology*, ed. S. Khan. DOT/FAA/CT- 92/11, FAA Technical Center, Atlantic City, NJ, pp 441–453

[84] Shi T M, Xie C G, Huang S M, Williams R A and Beck M S (1991), Capacitance-based instrumentation for multi-interface level measurement, Meas. Sci. Technol., 2, pp 923-933

[85] Sinclair G N, Appleby R, Coward P R and Price S (2000), Passive millimetre-wave imaging in security scanning, Proc. SPIE, 4032 (40), pp 40-45

[86] Singh S and Singh M (2003), Explosives detection systems for aviation security, *Signal processing*, 83 (1), pp 31-55

[87] Smith J, White T, Dodge C, Paradiso J and Gershenfeld N (1998), Electric field sensing for graphical interfaces, IEEE computer graphics and applications, 18 (3), pp 54-60

[88] Solartron Analytica (1996), 1260 impedance/gain-phase analyzer operating manual, available at http://www.solartronanalytical.com/downloads/datasheets/1260.pdf

[89] Steiner G (2006), Sequential fusion of ultrasound and electrical capacitance tomography, *Int. J. Inform. Syst. Sci.*, 2, pp 484-497

[90] Tsopelas N and Siakavella N J (2007), Performance of circular and square coils in electromagnetic-thermal non-destructive inspection, *NDT&E International*, 40, pp 12-28

[91] Tumanski S (2007), Induction coil sensors – a review, Meas. Sci. Technol., 18, pp 31-36

[92] Uesaka M, Hakuta K, Miya K, Aoki K and Takahashi A (1998), Eddy-current testing by flexible microloop magnetic sensor array, IEEE Trans. on Magnetics, 34 (4) pp 2287-2297

[93] Uesaka M, Nakanishi T, Miya K, Komatsu H, Aoki K and Kasai K (1995), Micro eddy current testing by micro magnetic sensor array, IEEE Trans. on Magnetics, 31 (1) pp 870-876

[94] Van Berkel C and Lionheart W R B (2007), An iterative method for electrostatic object reconstruction in a half space, Meas. Sci. Technol., 18, pp 41-48

[95] Wajman R, Mazurkiewicz L and Sankowski D (2004), The sensitivity map in the image reconstruction process for electrical capacitance tomography, 3rd Int. Symposium on Process Tomography in Poland, 9-10. Sept., Łódź, Poland, pp 165-168

[96] Wang H X, Yin W L, Yang W Q and Beck M S (1996), Optimum design of segmented capacitance sensing array for multi-phase interface measurement, Meas. Sci. Technol., 2, pp 79-86

[97] Webser J G (1995), Medical instrumentation: application and design, Wiley, New York

[98] West R M and Williams R A (1999), Opportunities for data fusion in multi-modality tomography, *1st World Congress on Industrial Process Tomography*, Buxton, Greater Manchester, Sept. 14 – 17, pp 195 – 200

[99] Xie C G, Huang S M, Hoyle B S, Thorn R, Lenn C, Snowden D and Beck M S (1992), Electrical capacitance tomography for flow imaging: system model for development of image reconstreuction algorithms and design of primary sensors, *IEE Proc. G*, 139, pp 89-98

[100] Xie C G, Huang S M, Lenn C P, Stott A L and Beck M S (1994), Experimental evaluation of capacitance tomographic flow imaging systems using physical models, *IEE Proceedings Circuits, Devices and Systems*, 141 (5), pp 357-368

[101] Xie C G, Stott A L, Plaskowski A and Beck M S (1990), Design of capacitance electrodes for concentration measurement of two-phase flow, Meas. Sci. Technol., 1, pp 65-78

[102] Yamada S, Katou M, Iwahara M and Dauson F P (1995), Eddy current testing probe composed of planar coils, *IEEE Trans. on Magnetics*, 31 (6), pp 3185-3187

[103] Yang M (2007), Development of electrical tomography systems and application for milk flow metering, PhD thesis, The University of Manchester, UK

[104] Yang W Q (1996 1), Charge injection compensation for charge/discharge capacitance measuring circuit used in tomography systems, *Meas. Sci. Technol.*, 7, pp 1073-1078

[105] Yang W Q (1996 2), Hardware design of electrical capacitance tomography systems, Meas. Sci. Technol., 7, pp 225-232

[106] Yang W Q (2001), Further developments in an ac-based capacitance tomography system, *Rev. Sci. Instrum.*, 72, pp 3902-3907

[107] Yang W Q and Peng L H (2003), Image reconstruction algorithms for electrical capacitance tomography, Meas. Sci. Technol., 14, pp 1-13

[108] Yang W Q and York T A (1999), New AC-based capacitance tomography system, IEE Proc.-Sci. Meas. Technol., 146(1), pp 47-53

[109] Yin W L, Peyton A J and Dickinson S J (2004), Simultaneous measurement of distance and thickness of a thin metal plate with an electromagnetic sensor using a simplified model, IEEE Trans. Instrum. Meas., 53 (4), pp 1335-1338

[110] York T (2001), Status of electrical tomography in industrial applications, *J. Electron. Imaging*, 10, pp 608-619,

[111] Zaid M, Paydecki P, Quek S, Miller G and Fernandes B (2002), Image reconstruction of steel reinforcing bars in concrete using fourier-domain

interpolation applied to a sparsely populated data set, *J. Nondestructive Eval.*, 18 (3), pp119-130

[112] Zeothout J, Boletis A and Bleuler H (2003), High performance capacitive position sensing device for compact active magnetic bearing spindles, JSME Int. J. Ser. B, Fluids and Thermal Eng., 46 (3), pp 900-907

Appendix A Calculating sensitivity matrix using dot-multiplication method

```
%% This file implements sensitivity matrix calculation using the dot-
%% multiplication method
clear all;clc;
RES = 60; % grid resolution for COMSOL output data

% Read ring cap array potential data generated from COMSOL with
% coordinates, the first 3 columns are x, y and z coordinates
p1=load('Ring_E1.txt');
p2=load('Ring_E2.txt');
% extracts potential from the 4th column
pp1=p1(:,4);
pp2=p2(:,4);
%% Calculate electric field using potential gradient
e1=reshape(pp1,RES,RES,RES);
[ex,ey,ez]=gradient(e1);
e1_x=reshape(ex,RES*RES*RES,1);
e1_y=reshape(ey,RES*RES*RES,1);
e1_z=reshape(ez,RES*RES*RES,1);
e2=reshape(pp2,RES,RES,RES);
[px,py,pz]=gradient(e2);
e2_x=reshape(px,RES*RES*RES,1);
e2_y=reshape(py,RES*RES*RES,1);
e2_z=reshape(pz,RES*RES*RES,1);
%% Calculate sensitivity using electric field using dot multiplication
A=e1_x.*e2_x;
B=e1_y.*e2_y;
C=e1_z.*e2_z;
s=(-1)*(A+B+C);

% for coil array, read field data calculated using COMSOL
% p1_x=load('5Coil_MagField_x_1.txt');
% p1_y=load('5Coil_MagField_y_1.txt');
% p1_z=load('5Coil_MagField_z_1.txt');
% p2_x=load('5Coil_MagField_x_2.txt');
% p2_y=load('5Coil_MagField_y_2.txt');
% p2_z=load('5Coil_MagField_z_2.txt');
% e1_x=p1_x(:,4);
% e1_y=p1_y(:,4);
% e1_z=p1_z(:,4);
% e2_x=p2_x(:,4);
% e2_y=p2_y(:,4);
% e2_z=p2_z(:,4);
% A=e1_x.*e2_x;
% B=e1_y.*e2_y;
% C=e1_z.*e2_z;
%s=(-1)*(A+B+C);

% Normalize sensitivity matrix
s_norm = s/sum(s);
% associate sensitivity values with geometry coordinates
sen=p1;sen(:,4)=s_norm;
```

```
% Calculate SVP, where SVP = S_dev/S_mean
SVP=std(s_norm)/mean(abs(s_norm))

% reshape sensitivity column into 40x40x40 array
s_reshape = reshape(s_norm,RES,RES,RES);

% extrace half space, 1:RES/2 for upper half space,
s_reshape = s_reshape(RES/2:RES,:,:);

% sum in the z direction
sum_s=sum(s_reshape,1);
ss_z=sum_s(:);ss_z=reshape(ss_z,RES,RES); % change array dimension

% Calculate 3×3 sensitivity coefficients
STEP = 20;
for i=1:3
    for j=1:3
        ss3(i,j)=sum(sum(ss_z((STEP *(i-1)+1): STEP *i, ...
                                (STEP *(j-1)+1): STEP *j)));
    end
end

% save sen_Ring.dat ss3 -mat;
% save sen_coil.dat ss3 -mat;
```

Appendix B Tomography imaging using 4×4 square-electrode array

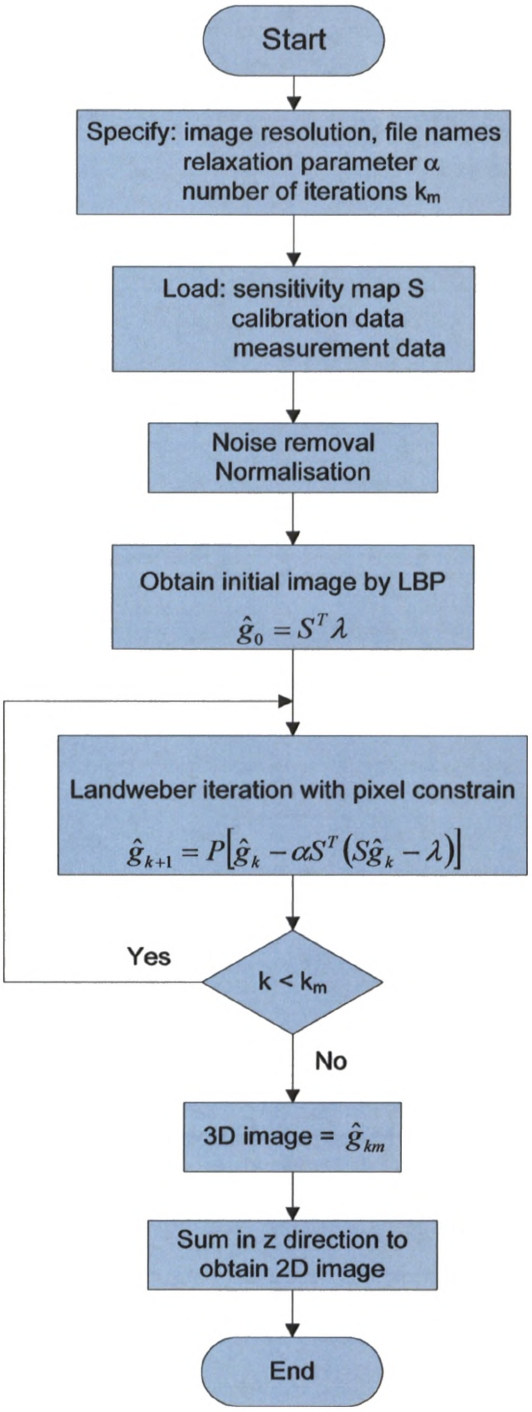

Fig. B.1 Flowchart for image reconstruction with Landweber iteration

```
%% This file implements Landweber iteration from 4x4 square-electrode
%% array using tomography scan
clear all; clc;
% define image resolution
XRES=20;
YRES=20;
ZRES=10;
mea_nb = 120;     % number of measurements in one set of data
R = 10;           % number of repetitions
normalised_sen=load('sen_NormalScan.dat');
normalised_sen_transpose = normalised_sen';
LowCap='Empty_AdaptiveN.mat';
MeaCap='Edge_SteelKnife_Straight_AdaptiveN.mat'
% specify parameters in landweber
number_of_iteration = 10;
alpha = 0.056;

%% Load calibration, measurement
% Low data
load(LowCap);%empty.r = measurements(1,1).data(:,1);empty.x =
measurements(1,1).data(:,2);
        for channel=1:mea_nb
            total_1=0;
            for rep=1:R
                total_1=total_1+measurements(rep,1).data(channel,1);
            end
            mean_1(channel)=total_1/R;
        end
empty = mean_1;
% Mea data
load(MeaCap);%empty.r = measurements(1,1).data(:,1);empty.x =
measurements(1,1).data(:,2);
        for channel=1:mea_nb
            total_1=0;
            for rep=1:R
                total_1=total_1+measurements(rep,1).data(channel,1);
            end
            mean_1(channel)=total_1/R;
        end
mea = mean_1;

%% Remove system noise from measurements
diff = (mea - empty);%./(empty.r);
idx=find(abs(diff)<1.5e-15);diff(idx)=0;
%% Normalise measurement
cap = (diff)./(0.5*empty);
cap(cap<0)=0;
cap(cap>1)=1;
cap=cap';
normalised_mea=cap;
% cap(cap<0)=0;
% cap(cap>1)=1;
```

```
%% Implement Lanweber iteration
% Obtain first guess using LBP
img_v=normalised_sen*normalised_mea;

% Iteration for n times
for n = 1 : number_of_iteration
img_v = img_v + alpha * normalised_sen * ...
                  (normalised_mea - normalised_sen_transpose * img_v);
    % Constrain pixel values
    img_v(img_v<0)=0;
    img_v(img_v>1)=1;
end

% Derive 2D image from 3D data
g_3d=reshape(img_v,ZRES,YRES,XRES);
g_2d=sum(g_3d,1);                    % sum in z direction
%change from 3D matrix to 2D matrix
g_2d=reshape(g_2d,XRES*YRES,1);g_2d=reshape(g_2d,XRES,YRES);
% apply grey level
img.c=g_2d*255;
% Display image, unit is the pixel of the screen
left = 500; bottom = 500; width = 240; height = 180
rect = [left, bottom, width, height];
figure('Position', rect);
imagesc(img.c);axis off;colorbar;
```

Appendix C Sensitivity-coefficient-based interpolation and fusion

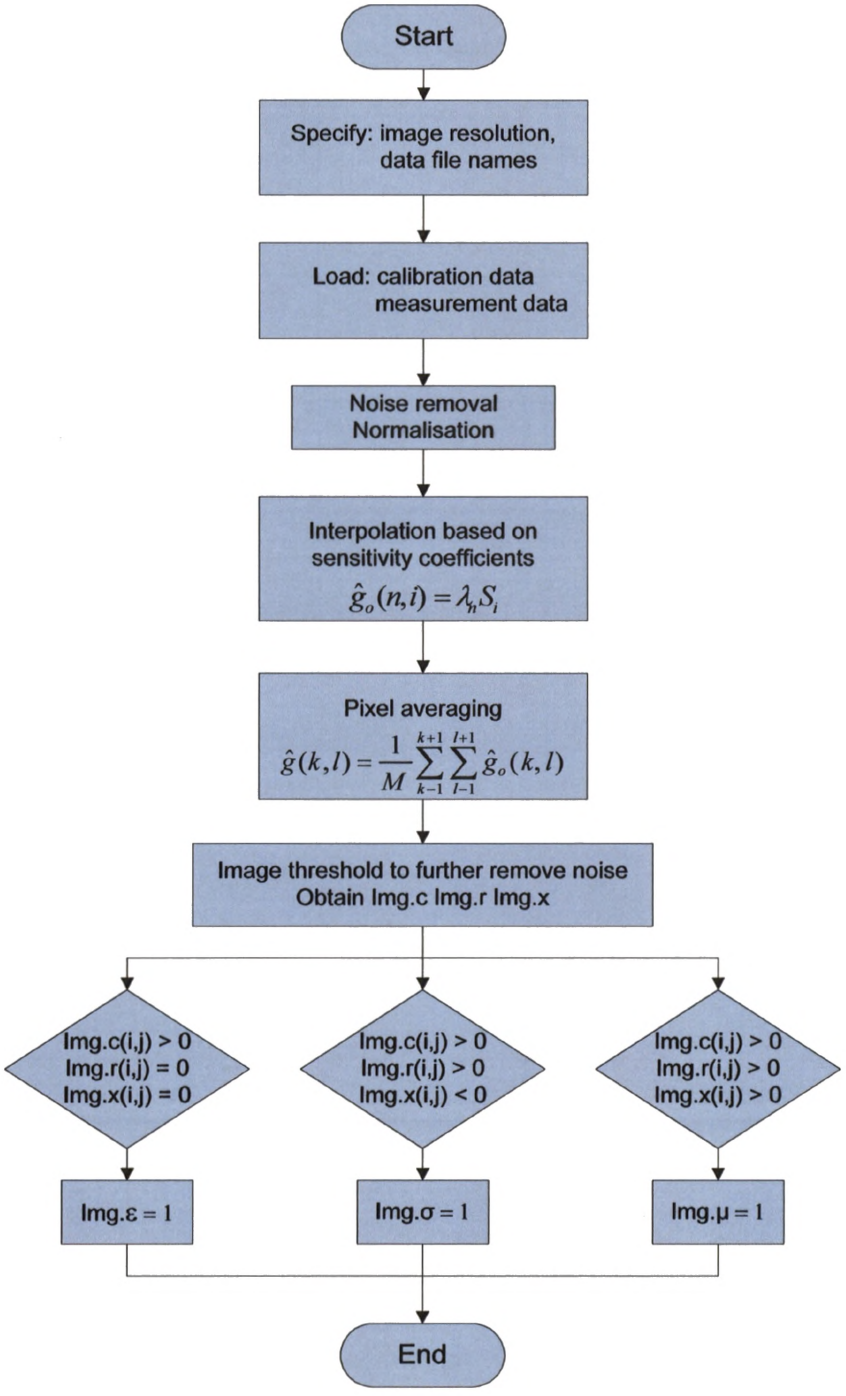

Fig. C. 1 Flowchart for interpolation and fusion for dual-modality array

```
%% This file implements imaging and fusion for the 2-Modality array
clear all;clc;
%% Settings
E_no = 6;       % number of excitation rows
D_no = 6;       % number of detection columns
SRES=3;         % resolution of sensitivity coefficients
XRES=18;        % x resolution of image
YRES=18;        % y resolution of image
mea_nb = 36;    % number of measurements in one set of data
R = 10;         % number of repetition for measurements
NoIter = 3;     % number of iteration for pixel averaging
% Load Measurements
LowCap = 'Empty_2Mod_C_500k.mat';
MeaCap = 'SteelCopperx3_Straight_2Mod_C.mat';
LowCoil= 'Empty_2Mod_M_10k.mat';
MeaCoil= 'SteelCopperx3_Straight_2Mod_M.mat';
%%%%%%%%%%%%%%%%%%%%%%%%%%%%%%%%%%%%%%%%%%%%%%%%%%%%%%%
%% Load measurement data and pre imaging process
%%%%%%%%%%%%%%%%%%%%%%%%%%%%%%%%%%%%%%%%%%%%%%%%%%%%%%%
%% Load calibration data from cap ring array
load(LowCap);
        for channel=1:mea_nb
            total_1=0;
            total_2=0;
            for rep=2:R
                total_1=total_1+measurements(rep,1).data(channel,1);
                total_2=total_2+measurements(rep,1).data(channel,2);
            end
            mean_1(channel)=total_1/R;
            mean_2(channel)=total_2/R;
        end
empty.c = mean_1;
empty.g = mean_2;
%% Load measurement data from cap ring array
load(MeaCap);
        for channel=1:mea_nb
            total_1=0;
            total_2=0;
            for rep=2:R
                total_1=total_1+measurements(rep,1).data(channel,1);
                total_2=total_2+measurements(rep,1).data(channel,2);
            end
            mean_1(channel)=total_1/R;
            mean_2(channel)=total_2/R;
        end
mea.c = mean_1;
mea.g = mean_2;
%% Load calibration data from coil array
load(LowCoil);
        for channel=1:mea_nb
            total_1=0;
            total_2=0;
            for rep=2:R
```

```
                total_1=total_1+measurements(rep,1).data(channel,1);
                total_2=total_2+measurements(rep,1).data(channel,2);
            end
            mean_1(channel)=total_1/R;
            mean_2(channel)=total_2/R;
        end
empty.r = mean_1;
empty.x = mean_2;
%% Load measurement data from coil array
load(MeaCoil);
        for channel=1:mea_nb
            total_1=0;
            total_2=0;
            for rep=2:R
                total_1=total_1+measurements(rep,1).data(channel,1);
                total_2=total_2+measurements(rep,1).data(channel,2);
            end
            mean_1(channel)=total_1/R;
            mean_2(channel)=total_2/R;
        end
mea.r = mean_1;
mea.x = mean_2;
%%%%%%%%%%%%%%%%%%%%%%%%%%%%%%%%%%%%%%%%%%%%%%%%%%%%%%%%
%% Noise removal and normalisation
%% Thresholds determined from the level of measurement noise
%%%%%%%%%%%%%%%%%%%%%%%%%%%%%%%%%%%%%%%%%%%%%%%%%%%%%%%%
%% For cap ring array
diff.c = (mea.c - empty.c);%./(empty.r);
diff.g = (mea.g - empty.g);%./(empty.x);
idx.c=find(abs(diff.c)<1e-15);diff.c(idx.c)=0;
idx.g=find(abs(diff.g)<1e-8);diff.g(idx.g)=0;
norm.c = (diff.c)./(0.5*empty.c);
norm.g = (diff.g)./(0.5*empty.g);
%% For coil  array
diff.r = (mea.r - empty.r);%./(empty.r);
diff.x = (mea.x - empty.x);%./(empty.x);
idx.r=find((diff.r)<0.0025);diff.r(idx.r)=0;
idx.x=find(abs(diff.x)<0.0025);diff.x(idx.x)=0;
norm.r = (diff.r)./(0.5*empty.r);
norm.x = (diff.x)./(0.25*empty.x);
%% RESHAPE C, G, R, X MEASUREMENT DATA TO 6x6 ARRAY
for i = 1 : E_no
    for j = 1 : D_no
        % row excitation column detection for Cap
        tmp.c(i,j) = norm.c(6-(j-1) + E_no*(6-i));
        tmp.g(i,j) = norm.g(6-(j-1) + E_no*(6-i));
        % column excitation row detection for coil
        tmp.r(i,j) = norm.r(6-(j-1) + E_no*(6-i));
        tmp.x(i,j) = norm.x(6-(j-1) + E_no*(6-i));
    end
end
norm = tmp;
%% Plot normalised measurement matrix
```

```
% generate a figure at a specific location with a specific size
% unit is the pixel of the screen
left = 500; bottom = 500; width = 800; height = 180;
rect = [left, bottom, width, height];
figure('Position', rect);
subplot(1,3,1);imagesc(norm.c(1:6,1:6));colorbar;title('C');
subplot(1,3,2);imagesc(norm.r(1:6,1:6));colorbar;title('R');
subplot(1,3,3);imagesc(norm.x(1:6,1:6));colorbar;title('X');
%%%%%%%%%%%%%%%%%%%%%%%%%%%%%%%%%%%%%%%%%%%%%%%%%%%%
%% Interpolation by sensitivity coefficients
%%%%%%%%%%%%%%%%%%%%%%%%%%%%%%%%%%%%%%%%%%%%%%%%%%%%
% structure of 3x3 sensitivity coefficients
%     c b c
%     b a b
%     c b c
% 3X3 SENSITIVITY COEFFICIENTS FOR RingCap_Transmission
% cap.a = 255*1; cap.b = 255*0.4140; cap.c = 255*0.0212;
sen.cap=[255*0.0212 255*0.4140 255*0.0212; ...
         255*0.4140 255*1      255*0.4140; ...
         255*0.0212 255*0.4140 255*0.0212];
% 3X3 SENSITIVITY COEFFICIENTS FOR COIL
% coil.a = 255*0.1399; coil.b = 255*0.1623; coil.c = 255*0.0527;
sen.coil=[255*0.0527 255*0.1623 255*0.0527; ...
          255*0.1623 255*0.1399 255*0.1623; ...
          255*0.0527 255*0.1623 255*0.0527];
%% Interpolation using sensitivity coefficients
% use mod(x,y) and fix(x/y) to control array operation
% img.c = zeros(E_no*3, D_no*3);
for i=1:E_no*3
    for j=1:D_no*3
        isen=mod(i-1,3)+1; % index for sensitivity coefficient
        jsen=mod(j-1,3)+1;
        imea=fix((i-1)/3)+1; % index for measurement matrix
        jmea=fix((j-1)/3)+1;
        int.c(i,j)=norm.c(imea,jmea)*sen.cap(isen,jsen);
        int.r(i,j)=norm.r(imea,jmea)*sen.coil(isen,jsen);
        int.x(i,j)=norm.x(imea,jmea)*sen.coil(isen,jsen);
    end
end
%% Pixel averaging for n times
% Y = filter2(h,X) filters the data in X with the two-dimensional FIR
% filter in the matrix h. It computes the result, Y, using two-
% dimensional correlation, and returns the central part of the
% correlation that is the same size as X.
% for n=1:3
    img.c=filter2(fspecial('average'),int.c);
    img.r=filter2(fspecial('average'),int.r);
    img.x=filter2(fspecial('average'),int.x);
%     img.c=filter2(fspecial('disk',1),int.c);
%     img.r=filter2(fspecial('disk',1),int.r);
%     img.x=filter2(fspecial('disk',1),int.x);
% end
%% Threshold image to further remove noise
```

```
i.c=find(abs(img.c)<5);img.c(i.c)=0;
i.r=find(abs(img.r)<4);img.r(i.r)=0;
i.x=find(abs(img.x)<4);img.x(i.x)=0;
%%%%%%%%%%%%%%%%%%%%%%%%%%%%%%%%%%%%%%%%%%%%%%%%%%%%
% Display interpolated images
%%%%%%%%%%%%%%%%%%%%%%%%%%%%%%%%%%%%%%%%%%%%%%%%%%%%
left = 100; bottom = 100; width = 240; height = 180;
rect = [left, bottom, width, height];
figure('Position', rect);imagesc(img.c);set(gca, 'CLim', [-
(abs(max(max(img.c)))+1), abs(max(max(img.c)))+1]);colorbar;axis off;
figure('Position', rect);imagesc(img.r);set(gca, 'CLim', [-
(abs(max(max(img.r)))+1), abs(max(max(img.r)))+1]);colorbar;axis off;
figure('Position', rect);imagesc(img.x);set(gca, 'CLim', [-
(abs(max(max(img.x)))+1), abs(max(max(img.x)))+1]);colorbar;axis off;
%%%%%%%%%%%%%%%%%%%%%%%%%%%%%%%%%%%%%%%%%%%%%%%%%%%%
%% Pixel based fusion using look-up table
%     Case 1    2    3  Else
%     C    +    +    +
%     X    0    -    +
%     R    0    all  +
% Decision epsl sigm mu Artefacts
for i=1:18
    for j=1:18
        if (img.c(i,j)>0) && (img.r(i,j)==0) && (img.x(i,j)==0)
            img.epsl(i,j)=1;
            img.sigm(i,j)=0;
            img.mu(i,j)=0;
        elseif (img.c(i,j)>0) && (img.x(i,j)<0)
            img.epsl(i,j)=0;
            img.sigm(i,j)=1;
            img.mu(i,j)=0;
        elseif (img.r(i,j)>0) && (img.x(i,j)>0)
            img.epsl(i,j)=0;
            img.sigm(i,j)=1;
            img.mu(i,j)=1;
        else
            img.epsl(i,j)=0;
            img.sigm(i,j)=0;
            img.mu(i,j)=0;
        end
    end
end
%%%%%%%%%%%%%%%%%%%%%%%%%%%%%%%%%%%%%%%%%%%%%%%%%%%%%%%%%%%%%%%%%%%%%%%%
% Display permittivity/conductivity/permeability images
%%%%%%%%%%%%%%%%%%%%%%%%%%%%%%%%%%%%%%%%%%%%%%%%%%%%%%%%%%%%%%%%%%%%%%%%
left = 400; bottom = 100; width = 240; height = 180;
rect = [left, bottom, width, height];
figure('Position', rect);imagesc(img.epsl);set(gca, 'CLim', [-1,
1]);colorbar;
figure('Position', rect);imagesc(img.sigm);set(gca, 'CLim', [-1,
1]);colorbar;
figure('Position', rect);imagesc(img.mu);set(gca, 'CLim', [-1,
1]);colorbar;
```